Methods for Optimising Detection of Strong Gravitationally-Lensed Explosive Transients

By

Dan Ryczanowski

A thesis submitted to
the University of Birmingham
for the degree of
DOCTOR OF PHILOSOPHY

Supervisor: Dr. Graham P. Smith

Astrophysics and Space Research Group
School of Physics and Astronomy
College of Engineering and Physical Sciences
University of Birmingham
August 2022

ABSTRACT

Gravitational lensing is a cornerstone prediction of Einstein's General Theory of Relativity, which provided us with the first piece of direct evidence that led to his theory becoming the accepted interpretation of gravity. Now, over one hundred years later, the study of gravitational lensing has evolved into a diverse field that is continually utilised to unveil the wondrous subtleties of our universe. Specifically, the gravitational lensing of explosive transient sources is a field which is set to make major contributions to some of the biggest open debates in astrophysics – including the Hubble Tension, the physics and nature of transient progenitors, the redshift evolution of explosive transient rates, and new tests of Einstein's theory. The next few years are pivotal for the subject, when observatories such as Rubin will transform studies of these events by increasing the number of discovered lensed transients by two orders of magnitude.

In this thesis, I give a description of my original contributions to the field, which are focused around optimising the detection of gravitationally-lensed explosive transient sources such as supernovae, gamma-ray bursts, gravitational waves and kilonovae using a watchlist-based approach. The outcome of my research has led to a new understanding of how a lensed transient watchlist should be constructed, and the development of an algorithm that is capable of locating the galaxy clusters relevant to the lensing of such transients within existing all-sky survey data, which can then be used to populate a lensed transient watchlist. In addition, I describe the searches for lensed transient sources I have been active in alongside my research.

Dedicated to my parents, Sue and Andy

ACKNOWLEDGMENTS

My foremost thanks go to my supervisor, Dr. Graham Smith, for his limitless patience, selflessness, knowledge and guidance throughout my studies. I also thank Dr. Matteo Bianconi for his support in countless ways over the years. My thanks go out to Dr. Matt Nicholl, Dr. Sean McGee, Dr. Ben Gompertz and Dr. Sam Oates for their always-valuable insights. Thank you to Prof. Martin Freer, for always taking the time out to support my progression. I thank Cress and Lucy for providing me with infinite joy, and for being true friends. I thank my fellow PhD students and friends – Alex 'Jill', Alice, Amit, Aysha, Diganta, Eliot, Evan, George, Harry, Matt, Natalie, Tom and Xinyue – for many memorable conversations, spirited games and (probably too many) trips to the pub. I thank all my friends from Swindon – Ben, Benky, Cal, (Captain) Cardi, Danny, Darius, Ed, Ferg, George, Harry, Jimmy, Jacob, Jay, Joby, Leigh, Matty, Nay, Richard, Ryan and Tom – for keeping me grounded and who always manage to provide unforgettable moments.

I thank my parents, for the unwavering support with whatever I choose to pursue. Tom, for the brotherly love. Janet and Paul, for the letters and the cat photos. David and Kate, for keeping me in their prayers. My late Uncle Mike, for the unhinged banter. Emma, for the companionship.

Ain't no right way,

just the wrong way I know

Juice WRLD – *"Empty"*

Contents

Page

1 Introduction **1**

Introduction **1**

1.1 Introduction to gravitational lensing 1

1.1.1 Emergence from General Relativity 1

1.1.2 The deflection of light 3

1.1.3 Multiple images 5

1.1.4 Magnification 9

1.1.5 Time Delay 13

1.2 Gravitational lensing observations 16

1.3 Explosive transients 21

1.3.1 Supernovae 24

1.3.2 Gamma-ray bursts 27

1.3.3 Gravitational waves and kilonovae 29

1.4 Gravitationally-lensed explosive transients 34

1.4.1 Lensed transients as cosmological probes 35

1.4.2 Utilising lensing for studies of EM and GW transients 38

1.4.3 Identifying lensed transients 40

1.4.4 Further applications 43

1.4.5 Previous observations of lensed transients 44

1.5 Outline of the science chapters 50

2 Paper 1 **52**

2.1 Preamble 52

2.2 Introduction 53

2.3 Hostless strongly lensed transients 55

2.4 Strong-lensing clusters in magnitude limited surveys 58

2.4.1 Statistical model 59

2.4.2 Strong lensing cross-section 60

2.4.3 Galaxy number density 63

2.4.4 Predictions of the model 65

2.5 Summary and Implications for Strongly-lensed Transients 65

3 Paper 2 **69**

3.1 Preamble 69

3.2 Introduction 70

3.3 Surveys/Data 73

3.3.1 Overview of data used 73

3.3.2 VISTA Data 74

3.3.3 *WISE* Data 74

3.4 Method 78

3.4.1 Background 78

3.4.2 Creating density maps with kernel convolution 78

3.4.3 Estimating overdensity significance 79

3.5 Testing the method 84

3.5.1 Known cluster/group-scale lens test sample 84

3.5.2 Results of the known lens test 85

3.5.3 False positive rate estimates 91

3.5.4 Testing on Rubin DP0 data . . . 93
3.6 Summary . . . 98

4 Searches for lensed transients using a prototype watchlist **101**
4.1 Introduction . . . 102
4.2 The prototype watchlist . . . 102
4.3 Searches for lensed SNe using ZTF/Lasair and the Liverpool Telescope . . . 106
4.3.1 The Lasair Transient Broker . . . 106
4.3.2 Identification and follow-up of lensed SN candidates . . . 107
4.3.3 Notable candidates from ZTF/Lasair . . . 112
4.4 Search for lensed GWs . . . 117
4.5 Search for lensed GRBs . . . 121

5 Conclusion **127**

Chapter 1

Introduction

1.1 Introduction to gravitational lensing

This section is an introduction to the gravitational lensing formalism relevant for this thesis. It contains no new information, and follows from three main texts [1, 2, 3].

1.1.1 Emergence from General Relativity

The General Theory of Relativity is the current accepted description of how gravity operates in our Universe. Within General Relativity, gravitation is described as a curving of the four-dimensional spacetime in the presence of mass, as opposed to treating it as a force. One consequence of this is that all massless particles follow a specific path through spacetime, known as a null geodesic, which depends upon the spacetime metric that defines the invariant spacetime interval ds^2, given by:

$$ds^2 = g_{\mu\nu} dx^\mu dx^\nu, \tag{1.1}$$

where $g_{\mu\nu}$ is the metric and dx represents the time and space coordinate vectors. In deep space, the Newtonian gravitational potential $|\Phi| = GM/r$ is zero, and the metric reduces to the Minkowski metric for flat spacetime:

$$g_{\mu\nu} = \eta_{\mu\nu} = \begin{pmatrix} -c^2 & 0 & 0 & 0 \\ 0 & 1 & 0 & 0 \\ 0 & 0 & 1 & 0 \\ 0 & 0 & 0 & 1 \end{pmatrix}. \tag{1.2}$$

In this case, the null geodesic is a straight line, recovering the well understood notion that light travels in a straight line. However, when light passes close to an object of significant mass, this is no longer true. In the case of light passing close (within a few tens of kiloparsecs) of a massive galaxy or galaxy cluster ($M \sim 10^{12}$–$10^{15}\mathrm{M}_\odot$), the gravitational potential is weak, but non-zero (i.e. $|\Phi|/c^2 \ll 1$), and so the metric becomes perturbed from that of flat spacetime to become:

$$g_{\mu\nu} = \begin{pmatrix} -c^2\left(1 - \frac{2GM}{rc^2}\right) & 0 & 0 & 0 \\ 0 & 1 + \frac{2GM}{rc^2} & 0 & 0 \\ 0 & 0 & 1 + \frac{2GM}{rc^2} & 0 \\ 0 & 0 & 0 & 1 + \frac{2GM}{rc^2} \end{pmatrix}. \tag{1.3}$$

In this metric, spacetime is curved which naturally affects how light travels. The overall effect is that the speed of light decreases to below c and that the path of light through space is now curved. This commonly occurs when light that travels from a distant extragalactic source intercepts a galaxy or galaxy cluster on its journey towards Earth, during which it travels

through regions of spacetime that are approximately flat, then curved, then approximately flat again. The region of curved spacetime influenced by the galaxy or cluster deflects the path of the light from its initially straight trajectory to a curved one – this is known as *gravitational lensing*, and the object causing the deflection is known as a *gravitational lens* (or just a *lens* for short).

1.1.2 The deflection of light

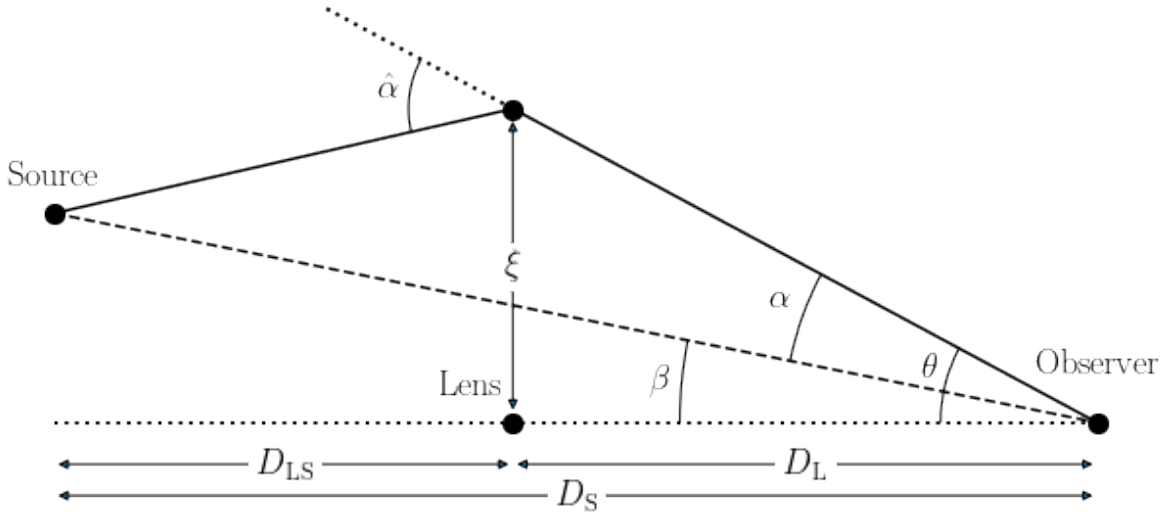

Figure 1.1: Schematic showing light from a source at distance D_{S} being deflected by a gravitational lens at distance D_{L}. The distance between the lens and the source is denoted D_{LS}. Due to the deflection, the observer sees an image of the source at an angle θ rather than at the true source position β. $\hat{\alpha}$ is the deflection angle experienced by the light as it passes the lens with impact parameter ξ. Diagram from [3].

Figure 1.1 shows a schematic setup for a typical gravitational lensing system. This system invokes the *thin lens approximation*, where it is assumed the deflection of the light ray takes place instantaneously at the lens position along the line of sight axis between

the observer and the lens, with impact parameter ξ between the trajectory of the light ray and the lens. This approximation is valid if the size of the region where the gravitational potential is perturbed by the lens along the line of sight is much smaller than the distances D_{L} and D_{LS} between the observer and the lens, and the lens and the source respectively. In extragalactic systems, these distances are typically in the order of Gpc, whereas the dense cores of the largest galaxy clusters are at most a few hundred kpc and therefore justifies applying the thin lens approximation. It should be noted that this and any of the following equations that are functions of D_{L}, D_{S} or D_{LS} only hold in an expanding Universe like our own if these distances are represented as angular diameter distances, rather than physical distances.

Perhaps the most notable feature of gravitational lensing is that the apparent location of a lensed source (the *image*) as seen by an observer is offset from its true position. Tracing backwards from the deflected ray reveals the direction toward which an observer would see the image of the source. This is denoted by the angle θ from the observer-lens line of sight, and is distinct from the true source position denoted by the angle β. The deflection angle, $\hat{\alpha}$ is a useful quantity that describes by how much the light has deflected during the lensing process. In general, this depends on the mass distribution of the lens, but it can be shown that for a point-mass lens:

$$\hat{\alpha} = \frac{4GM}{c^2\xi}, \tag{1.4}$$

where M is the mass of the lens. In other words, the deflection angle scales with the Newtonian potential at the point of deflection. This quantity is of particular significance, as calculating the same quantity whilst assuming Newtonian gravity rather than General Relativity gives a result that is a factor of 2 smaller. Therefore, measurements of $\hat{\alpha}$ were historically used to provide evidence to distinguish between which of Einstein's or Newton's representation of gravity describes reality more closely. Such a measurement was performed by Dyson et al. in 1919 [4], in which a solar eclipse was utilised to be able to measure the

positions of stars close to the limb of the Sun. The background stars had been shifted slightly relative to their expected positions due to gravitational lensing from the Sun, and their recorded offset was more consistent with General Relativity than the Newtonian result. This marked the first piece of direct observational evidence in favour of Einstein's theory. Since then, gravitational lensing has found many applications within astronomy, often utilising the deflection of light to provide information about the masses of objects acting as lenses (e.g. [5]). This technique is one of the few ways to obtain a direct measurement of the mass of an extragalactic object, and therefore has also been used to confirm the existence of dark matter within galaxy clusters in our Universe (e.g. [6, 7]). However, this is just scratching the surface for the many applications of gravitational lensing, and later sections of this introduction will explore these further.

1.1.3 Multiple images

Geometrically, by considering Figure 1.1, and by invoking small angle approximations for the angles involved, it can be shown that:

$$\theta D_{\mathrm{S}} = \beta D_{\mathrm{S}} + \hat{\alpha} D_{\mathrm{LS}}. \tag{1.5}$$

Then by simply rearranging, this equation becomes:

$$\beta = \theta - \frac{D_{\mathrm{LS}}}{D_{\mathrm{S}}}\hat{\alpha} \equiv \theta - \alpha(\theta). \tag{1.6}$$

By defining the scaled deflection angle $\alpha(\theta) = \frac{D_{\mathrm{LS}}}{D_{\mathrm{S}}}\hat{\alpha}$, the right-hand side of Equation 1.6 has become one of the most well-known relations in gravitational lensing, the *lens equation*. Whilst the lens equation can be written succinctly, it is non-linear since α itself depends upon the image angle θ (in the point-mass example of Equation 1.4, $\hat{\alpha}$ depends on ξ which can be seen in Figure 1.1 to be directly related to θ). Due to this non-linearity it is possible to have

multiple values of θ that are solutions to the lens equation – in other words, a single lensing configuration can have multiple valid image positions. This is the reasoning that describes how gravitational lensing can, under the right circumstances, produce multiple images of a single source. The special case where multiple images of a source are produced is known as *strong lensing*, and comprises its own field of research due to its many applications, which are explored further later in this introduction. When lensing occurs but does not produce multiple images, the image can still be magnified (see subsection 1.1.4), and distorted to a different shape. The distortions are often subtle, and the effect can only be realised in a statistical sense by looking at the average effect of the warping of a large number of so called *weakly-lensed* background galaxies. Weak lensing can affect a significant number of background objects depending on the mass and extent of the lens, and hence provides information about the foreground mass distribution (e.g. [5, 8]). Strong lensing requires very precise alignment of sources with lenses, and the effect is only influenced by the mass central to the source. Thus mass measurements from strong lensing cannot be utilised in every case due to its rarity, and also do not provide a complete measurement of the entire cluster mass, only of the mass interior to the projected Einstein ring – both of these issues can be subverted by weak lensing, hence its wider use.

Since the deflection angle $\hat{\alpha}$ depends on both the geometry of the lensing configuration (i.e. impact parameter ξ and the distances between the source, lens and observer), and the mass distribution of the lens, the condition for strong lensing also shares these dependencies. The solution for image positions with a point mass lens is quadratic, hence there are two solutions and two images are always produced. However, this is not always the case with more realistic extended mass distributions, and configurations exist in which greater numbers of images form. The requirement that β is small (i.e. the source is closely aligned with the lens) is always required in order to produce multiple images, although the exact scale of this depends on the mass distribution of the lens. It is therefore convenient to define the

convergence, κ of the lens' mass distribution:

$$\kappa(\theta) = \frac{\Sigma(\theta)}{\Sigma_c}, \tag{1.7}$$

where $\Sigma(\theta)$ is the surface density, which quantifies how the mass in the lens is distributed in our two-dimensional view of the object on the sky, and is defined as the three dimensional density integrated along the line of sight distance z:

$$\Sigma(\theta) = \int \rho(\theta, z)\mathrm{d}z. \tag{1.8}$$

Σ_c is a constant known as the *critical surface density*, defined as:

$$\Sigma_c = \frac{c^2 D_\mathrm{S}}{4\pi G D_\mathrm{LS} D_\mathrm{L}}. \tag{1.9}$$

The critical surface density is used as a convenient way to parameterise the surface density in relation to strong lensing, as typically $\kappa > 1$ represents the values of θ that correspond to strong lensing/multiple images, and $\kappa < 1$ represents single images. However, in order to fully understand exactly when, and how many multiple images will form, one needs to consider the *caustic curves* of a given system – which will be explained further in subsection 1.1.4.

For point mass (or axisymmetric) lenses, a very special case occurs if the source is exactly aligned with the lens along the line of sight. In this case, $\beta = 0$ and the lens equation is solved when

$$\theta = \sqrt{\frac{4GMD_\mathrm{LS}}{D_\mathrm{S} D_\mathrm{L} c^2}} = \theta_E, \tag{1.10}$$

where θ_E is a special quantity known as the Einstein radius. In two dimensions, this would produce images at $\theta = \pm\theta_E$, however in three dimensions there are an infinite number of solutions with $\theta = \theta_E$, as one can choose any orientation of the incident ray rotated around the line of sight (in or out of the plane of Figure 1.1). Therefore the source is lensed into a complete ring (colloquially an Einstein ring), which has angular radius θ_E. The Einstein radius is typically used to quantify the size and strength of a gravitational lens – a larger Einstein radius indicates the sky area across which the strong lensing effect of the object

occurs is larger. In addition, the Einstein radius is the typical maximum angular separation between a source and lens for which strong lensing will occur. For massive galaxies, θ_E is on the order of a few arcseconds (e.g. [9]), whereas massive galaxy clusters can have much larger radii ranging from tens of arcseconds up to of order one arcminute in the most extreme cases (e.g. [10, 11]).

Another commonly-utilised quantity relevant to the production of multiple images is the dimensionless quantity τ, colloquially known as the *Fermat potential*, written in terms of the angular position vectors θ, β and the dimensionless projected gravitational potential $\psi(\theta)$ (see subsection 1.1.4):

$$\tau = \frac{(\theta - \beta)^2}{2} - \psi(\theta). \tag{1.11}$$

The Fermat potential, up to a linear approximation, can be used to calculate the light travel time for a ray that starts at position β, intercepts the lens place at θ, then arrives at the observer. Real lensed rays (i.e. those that obey the lens equation) are those that obey $\nabla\tau = 0$ in equivalence with Fermat's principle in optics, which therefore gives rise to the name for this quantity. This means that the lens equation can be recovered by differentiating the Fermat potential and setting it equal to zero, uncovering the relation:

$$\alpha = \nabla\psi. \tag{1.12}$$

The Fermat potential provides an insight into the formation of multiple images by a gravitational lens by looking at the stationary points of τ . Each stationary point directly corresponds to a real light-path that obeys the lens equation, and therefore also corresponds to an image. Succinctly, the number of stationary points is equal to the number of images produced. In addition to this, extrema of the Fermat potential also provide information

about the surface mass density at that location – maxima indicate $\kappa > 1$ whilst minima indicate $\kappa < 1$. The Fermat potential is also related to the time delay – which will be explored in subsection 1.1.5.

1.1.4 Magnification

When the size of the source is much smaller than the scales on which the properties of the lens change, the mapping between the planes depicting the un-lensed case (the *source plane*) and the lensed case (the *lens plane*) can be written linearly, and hence can be represented by a Jacobian matrix that defines the transformation from one plane to another:

$$J_{ij} = \frac{\partial \beta_i}{\partial \theta_j} = \left(\delta_{ij} - \frac{\partial^2 \psi(\theta)}{\partial \theta_i \partial \theta_j} \right). \tag{1.13}$$

Here, θ and β represent the angular vectors of the source position in the image and source planes, respectively and i, j indices may represent $\{x, y\}$ coordinates in the respective planes. $\psi(\theta)$ is the *projected gravitational potential* – the 3D potential Φ projected onto the two-dimensional lens plane, that is written in a dimensionless form:

$$\psi(\theta) = \frac{D_{\mathrm{LS}}}{D_{\mathrm{S}} D_{\mathrm{L}}} \frac{2}{c^2} \int \Phi(\theta, z) \mathrm{d}z. \tag{1.14}$$

Note that in the above equation, z refers to the distance coordinate along the line of sight, rather than a redshift. The projected potential is related to the scaled deflection angle (Equation 1.12) and can also be calculated directly in terms of the convergence as:

$$\psi(\theta) = \frac{1}{\pi} \int \kappa(\theta') \ln |\theta - \theta'| \mathrm{d}^2 \theta'. \tag{1.15}$$

Given the Jacobian encodes the information that transforms between the source and lens planes, it is not surprising that one can use it to determine the change in area (solid angle) of a source between the source and lens planes. The increase in solid angle is known as the *magnification*, and is equal to the determinant of the Jacobian matrix:

$$\mu = |J_{ij}|^{-1} = \left[(1-\kappa)^2 - \gamma^2\right]^{-1}, \tag{1.16}$$

where γ is known as the *shear*. The shear is duly named as when non-zero, the lensed image will be distorted in a similar manner to the geometrical shear transformation (strictly it changes the size ratio of the axes of the image). It is typically written with two components γ_1, γ_2, where $\gamma^2 = \gamma_1^2 + \gamma_2^2$, and for completeness, these two components are determined as:

$$\gamma_1 = \frac{1}{2c^2}\left(\frac{\partial^2\psi}{\partial\theta_x^2} - \frac{\partial^2\psi}{\partial\theta_y^2}\right), \tag{1.17}$$

$$\gamma_2 = \frac{1}{c^2}\frac{\partial^2\psi}{\partial\theta_x\partial\theta_y}. \tag{1.18}$$

Surface brightness, defined as flux per unit angular area, must be conserved in the lensing process. Therefore, if the apparent angular size of an object increases, so must the received flux. One could therefore also quantify the magnification by considering the increase in the flux of the source between the lensed and un-lensed cases:

$$\mu = \frac{F_{\text{lensed}}}{F_{\text{not lensed}}}. \tag{1.19}$$

This is analogous to lenses in classical optics, where more rays are deflected toward a particular point, causing an increase in the measured flux at that location.

Observationally, the magnification caused by gravitational lensing means any lensed source has its apparent magnitude changed by $\Delta m = -2.5\log(|\mu|)$. It is important to note that whilst magnification is generally referred to in terms of an increase in flux, because

total flux must be conserved, magnification leads to a decrease in flux in other regions – a *demagnification* occurs, where $|\mu| < 1$. In addition, since magnification is a function of the image position θ, it can vary between the images of a strongly-lensed source. This means that some images can experience magnification and become brighter, whilst others might be demagnified, leading to images that are much harder to detect in practice. Magnification can also be a negative quantity, which indicates the image has been flipped relative to the image that would be observed if not lensed, although this does not affect the detectability of the image since the change in flux is dependent only on $|\mu|$. In general, magnification is utilised essentially as a free telescope upgrade, allowing sources to be observed that would not usually be detectable with a given instrument. In cases of strong lensing (production of multiple images) by a galaxy cluster, $|\mu| \gtrsim 10$ is typical, whereas $|\mu| \gtrsim 2$ is typical with galaxy lenses [12]. Magnifications lower than these are also possible, although these generally involve only singly-imaged systems and hence would not be classed as strongly lensed, but they still take advantage of the increase in observed flux. When the alignment of the source and the lens is ideal, higher magnifications can be achieved, even reaching extreme values of $|\mu| > 10^4$. This can be seen from Equation 1.16 by noting that $\mu \to \infty$ as the denominator $\to 0$. Infinite magnification is physically unreasonable due to the finite size of sources limiting how much the flux can increase for a given surface brightness, however, the regions where this condition is mathematically satisfied define very useful regions of the source plane known as *caustics*. High magnifications require objects to be very closely aligned with a caustic, hence determining them allows us to know around which regions the lensing magnification is the most extreme. These cases, in general, can enable observations of some of the highest redshift objects ever observed by taking advantage of this flux boost, and in turn allow us to infer properties of the early Universe and the sources that populated it.

Caustics also determine where multiple images of sources in the background of a lens will form, since any sources within a caustic curve will form +2 images compared to the

number of images formed of the same source outside that caustic. This means that the number of images that form from a gravitational lens must *always* be odd, as outside any caustic one image naturally forms, then +2 more form for each successive caustic. However, in many real examples of gravitational lensing systems, an even number of images are actually observed (e.g. quadruply-imaged quasars [13]). This occurs for a few reasons: firstly because some images can be demagnified and hence are very hard to detect, and secondly because images can be formed on top (or very closely aligned to) the lens itself. In these scenarios, the full (odd) number of images do form but some are just incredibly difficult to detect. In addition, images can blend together, due to telescope optics and the extended nature of many lensed sources, making it difficult to distinguish between the separate images.

Another important feature of caustics is that they have equivalent regions when mapped into the image plane – these are known as *critical curves*. Lensed sources that lie directly on caustics will produce images that span the critical curves, forming arcs and Einstein rings. For a point mass lens, there is also a point caustic directly aligned with the point mass along the line of sight. The corresponding critical curve for this caustic is a circle of radius θ_E around the point mass, so a perfectly aligned source will be lensed into an Einstein ring along this critical curve. The mapping of caustics to critical curves is also dependent on the source redshift, so a single lens has a family of critical curves. This can easily be seen for the point-mass case in Equation 1.10 – the Einstein radius depends explicitly on D_{L}, the separation between the lens and the source. The appearance of giant arcs can also be explained using caustics – in lenses with non-point-like caustics, extended sources that straddle the caustics are partly within and partly outside the region that causes multiple images to form. The images will be stretched along the critical curves in the image plane to create arcs, but as the source is not completely within the caustics, the images will also still partially be overlapping. See section 1.2 for imaged examples of Einstein rings and giant arcs.

Observationally, one of the difficulties in determining magnification is that it is impossible to know exactly the intrinsic brightness of a lensed source. This therefore requires models or observations of similar objects in order to estimate the intrinsic brightness. Knowing the magnification to sufficient precision is important as it is an easy way to resolve the problem of mass-sheet degeneracy in lens modelling. More specifically, if one tries to determine a suitable mass distribution for a lens given a set of observed image positions and properties, there are an infinite number of solutions. This is because if $\kappa(\theta)$ is a solution, then $(1-\lambda)+\lambda\kappa(\theta)$ will also be a solution, where λ is a constant scaling factor. The new solution is equivalent to adding a constant surface-density plane (a mass-sheet) and consequently re-scaling the original distribution. However, the magnification is also affected by this scaling: $\mu \to \mu/\lambda^2$, so if the magnification is know a priori, then the degeneracy can be broken. If the lensed source is a standard candle, like a Type-Ia supernova (see subsection 1.3.1), then the precision at which the magnification can be determined is significantly improved as there is less ambiguity in its intrinsic luminosity.

1.1.5 Time Delay

Another striking feature of strong gravitational lensing is the time delay between the arrival of different images of the same object. Although each image emerges from the same source, and the light corresponding to each image was emitted at the exact same time, the light does not arrive at our detectors simultaneously due to a lensing-induced time delay. The total time delay is defined as the difference in arrival time between two photons emitted simultaneously, but that travel on different paths influenced by gravitational lensing. There are two contributions to the total time delay: geometrical time delay and Shapiro time delay. Geometrical time delay is a difference in travel time due to the paths taken by the photons having physically different lengths due to differences in curvature, whereas Shapiro

time delay is caused by the "slowing" of the photon due to time dilation in the gravitational field of the lens [14]. Both of these contributions are caused by the local effect of lensing experienced by the photon on its trajectory, which can easily be asymmetrical based on the position of the source relative to the lens and the mass distribution of the lens.

By utilising the metric in Equation 1.3, it can be shown that the total time delay experienced by a photon, compared to an undeflected photon emitted from the same point is:

$$\Delta t = \frac{(1+z_{\mathrm{L}})}{c}\frac{D_{\mathrm{L}}D_{\mathrm{S}}}{D_{\mathrm{LS}}}\left[\frac{(\theta-\beta)^2}{2}-\psi\right]. \tag{1.20}$$

Here, symbols have their usual meanings, and z_{L} is the redshift of the lens. The factor $(1+z_{\mathrm{L}})$ takes into account the expansion of the Universe as the photon travels and ensures the equation is valid over cosmological distances. The two terms in square brackets are the Fermat potential (Equation 1.11), which when combined with the constants, represent the geometric and Shapiro time delay, respectively. The geometric time delay simply quantifies the change in path length by the new trajectory of the photon compared to the original, whereas the Shapiro time delay quantifies the effect of gravitational time dilation caused by the lens with projected potential ψ. It is important to note that Δt is the difference in arrival time for a single image between the lensed and non-lensed case, which is different to the observable quantity of the time difference between the arrival of two images of a lensed source. This is instead calculated by the difference in values of Δt each calculated for the specific images.

Observationally, time delay can be measured by comparing lightcurves (recording the flux against time) of two or more images of a strongly-lensed object and identifying the same features in each curve. Then, it is simply a case of measuring the time difference Δt between identical features in each image's lightcurve. For a source with homogeneous emission like

a galaxy, it is not possible to probe the time delay since there are typically no discerning features to measure the time delay against. In other words, if one has a lightcurve for each of two images of a strongly-lensed galaxy, it would not be possible to pinpoint a suitable feature within a lightcurve to act as a reference point. As a result, time delay is mostly discussed with reference to transient or variable sources like active galactic nuclei (AGN), quasars and supernovae which have much more prominent features or lightcurves. This is especially true for the case of supernovae, whose lightcurves have a single distinct rise and fall, so it is straightforward to calibrate on the peak brightness.

Arguably the most important application of time delay from gravitational lensing is the ability to measure the Hubble parameter, H_0. The easiest way to see how this is possible is to consider the distance ratio factor in Equation 1.20. Since each angular diameter distance term is proportional to H_0^{-1}, Δt is also proportional to H_0^{-1}. Thus, a precise measurement of the time delay corresponds to a direct evaluation of the Hubble parameter, as long as the other quantities are known. Specifically, the uncertainty in the Hubble constant measurement is proportional to the *fractional* time delay – i.e. the uncertainty in the time delay over the total length of the time delay. Therefore, the most precise measurement would involve a long time delay, measured with minimal error.

Typically the quantity other than the time delay that is most difficult to precisely determine is the projected lens potential, ψ, as this requires detailed knowledge of all the mass components (dark and luminous matter) that contribute to the lens. Individual galaxy lenses tend to be easier to model given they are dominated by a single density function, but cluster lenses will have multiple components, including the underlying dark matter halo as well as perturbations from the member galaxies. However, with sufficient data the projected potential can be constrained and the Hubble parameter determined.

Determining H_0 via time delays is extremely important since it is a direct and one-

step measurement that is independent of any other method. This is made especially notable because of the so-called "Hubble tension", a high-significance ($> 4\sigma$, depending on which datasets are compared) discrepancy between values of H_0 determined by observations of phenomena from the early and late Universe [15, 16]. This is perhaps the greatest discrepancy of modern astrophysics and implies either the existence of new physics beyond the current understanding of cosmology, or that there are unaccounted statistics in the method(s). However, there is little evidence thus far that suggests either is closer to the truth. Gravitational time delay is not sensitive to the same assumptions that these methods require, and therefore has the capability to provide valuable insight into solving this discrepancy.

Time delay also has applications for unearthing new physics about transient sources such as supernovae or kilonovae. If a lens is modelled well enough, then it is possible to accurately determine, in advance of its appearance, if and where another image of a lensed transient will appear. This is unique, as there are usually no indicators that, for example, a supernova is about to explode in a particular galaxy, and therefore provides the opportunity to study the early stages and evolution of a supernova's lightcurve that would normally be missed with conventional searches with standard response times.

1.2 Gravitational lensing observations

Despite the theory behind strong gravitational lensing being formulated in the early-to-mid 1900s, it was not until 1979 that the first observation of a multiply-imaged source was observed. During observations in March of that year, aiming to identify radio-emitting sources in optical bands, Walsh et al. [17] discovered a system of two quasars – luminous galactic nuclei – separated by only 5.7 arcseconds that appeared to have identical redshifts and spectra. The system, QSO 0957+561 (shown in Figure 1.2), was shown to be consistent with being

two images of a single gravitationally-lensed object, with one image being magnified by a factor of ~ 4 with respect to the other. Further observations alluded to the lensing interpretation, including further identical spectra at other wavelengths, and the identification of a putative lens – a galaxy at the centre of a small cluster located between and at lower redshift than the two quasars [18]. All this evidence surmounted into this being an undeniable case of the multiple imaging of an extragalactic object due to gravitational lensing.

In the years since the first detection, a variety of lensed sources have been detected, including quasar point sources with greater image multiplicities, lensed galaxies forming multiple images, Einstein rings and arcs, and lensed supernovae (lensed transients will be discussed in more detail in subsection 1.4.2). Figure 1.3 shows a lensed object with an "Einstein cross" formation, where the background source is lensed into four identical images in a cross configuration. This occurs when a background object is within two caustics of a lens – meaning five images are produced, but with one that is usually unobservable due to being demagnified and being so close to the lens itself that its emission blends with the lens. Such configurations have been used to calculate H_0 by observing the time delay between the images from the concept originating in [19]. In particular, multiply imaged quasars have been used to measure H_0 to a precision of 2.4 percent ($73.3^{+1.7}_{-1.8}$ km/s/Mpc, [20]). Such measurements can however still be complicated by time-dependent gravitational lensing on very small scales – known as microlensing – and this contributes to the uncertainty on the final result. Stars or other objects within the lensing galaxy moving in and out of the line of sight via rotation or their peculiar velocities causes the lensing signal to be inhomogeneous, complicating measurements that can make it hard to distinguish the variability of the quasar above all the noise. However, as long as a large baseline is used for measurements (typically at least a few years, depending on the quality of photometry and cadence of data) the variability due to microlensing can be accounted for statistically.

Measurements of the Hubble parameter using lensing are valuable since they are com-

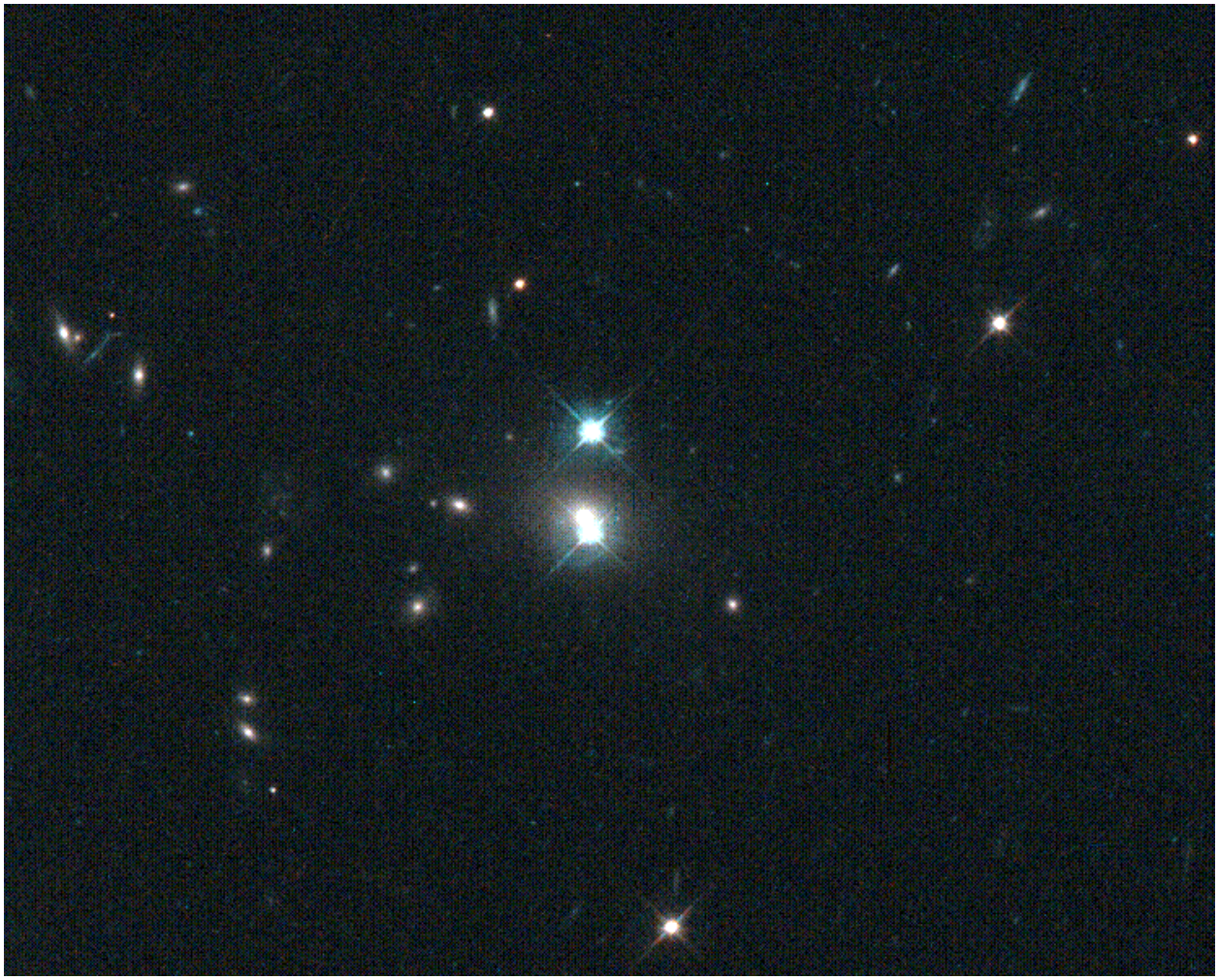

Figure 1.2: An image of the twin quasar system QSO 0957+561, where the two images of the $z = 1.41$ quasar are the bright objects in the centre of the frame. The lens galaxy ($z = 0.36$) is the brightest central galaxy of a galaxy cluster, and can be seen just above the lower quasar image with a slightly redder colour. The two quasar images are separated by ~ 6 arcsec, which is slightly larger than would be expected for an isolated galaxy lens, likely due to the lensing also being influenced by the mass of the dark matter within the cluster component of the lens. Image credit: G. Rhee, ESA/NASA Hubble.

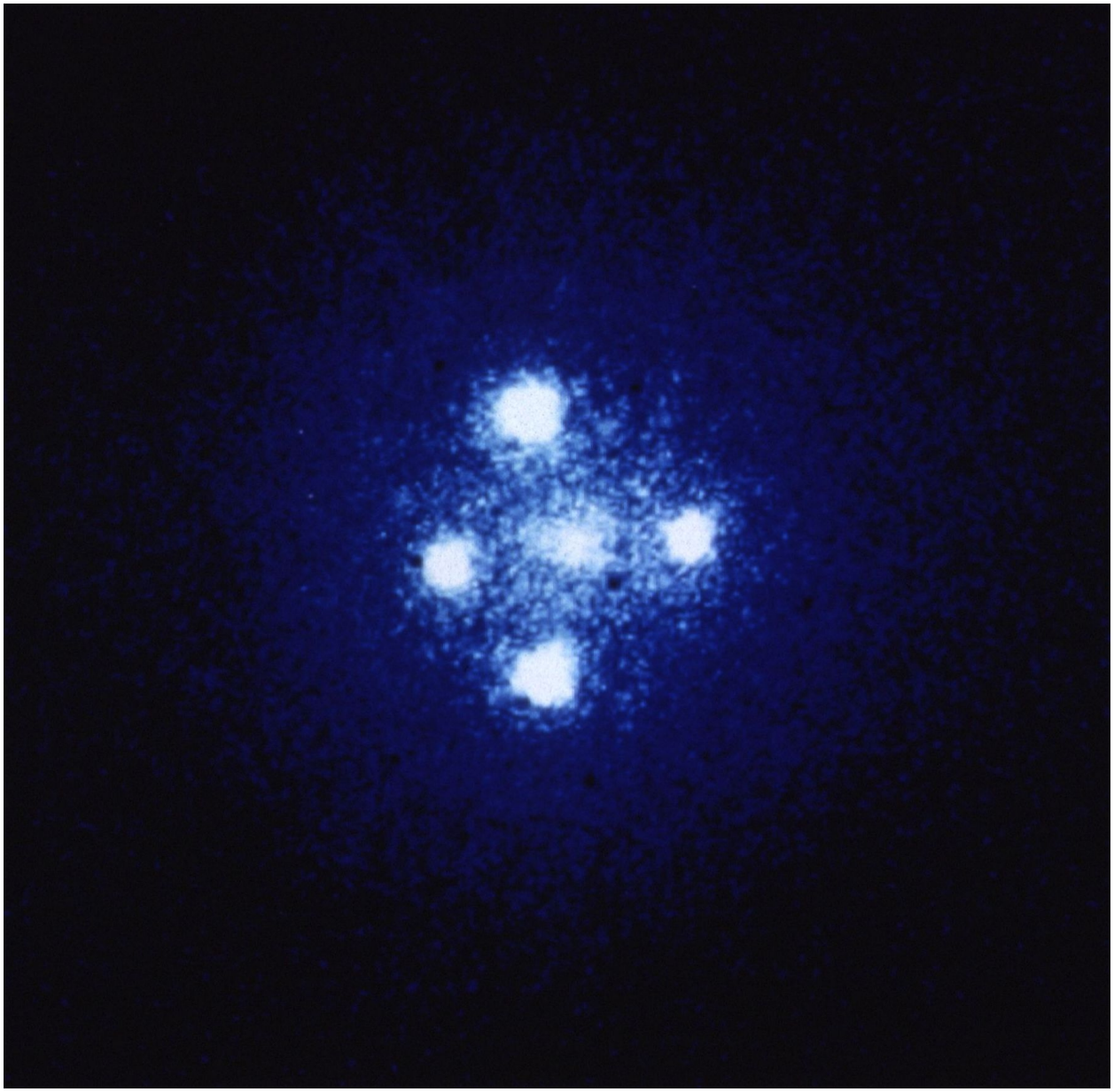

Figure 1.3: The gravitationally-lensed quasar QSO 2237+0305 split into four images in a cross-configuration by a central galaxy lens. This particular object was discovered in 1985 initially considered peculiar due to only a single, magnified image being resolved via observations [21]. Later follow-up discovered that the single image actually consists of four separate components (the angular separation between the top and bottom images is only 1.6". Such configurations additionally expect a fifth, faint and demagnified image very close to the position of the lens, which is not usually resolved. Image credit: NASA/ESA Hubble.

pletely independent of other 'local universe' measurements i.e. measurements made using objects at fairly 'low' redshifts ($0 \lesssim z \lesssim 10$); compared to 'early universe' measurements that utilise phenomena like the cosmic microwave background originating from $z \sim 1100$. Local universe measurements are typically those made relying on the cosmic distance ladder – distance measurements made based upon observables that are known to directly depend on the distance to the object. Many of these measurements are only useful over particular distance ranges, and are used to calibrate other methods giving rise to the notion of a distance 'ladder' – the success of some methods relies on other methods on previous 'rungs' of the ladder. Two examples of such measurements can be performed using cepheid variable stars and Type Ia supernovae – objects utilised for Hubble parameter measurements by the SH0ES team [15]. Cepheid variables have a known relationship between the period of their brightness oscillations and their luminosities, hence observing these periodicities can allow distances to be calibrated [22]. Similarly, Type Ia supernovae (discussed further in subsection 1.3.1) are known as *standard candles* – objects whose luminosities can be calibrated to a standard value in order to directly measure their distance from their observed brightness [23]. Local universe measurements of H_0 from lensing are completely independent from any other local universe method, which means they do not rely on the cosmic distance ladder or any innate systematics that may arise from measurements at any step of the ladder. Having independent methods to verify each other is especially important for attempts to resolve the Hubble tension. Thus, performing as many separate measurements of cosmological parameters as possible based upon differing astrophysical phenomena is one way to introduce new information and work toward a solution to the problem. Gravitational lensing has (and will continue to) play a vital role in this.

Figure 1.4 shows an image of a near-complete Einstein ring, where a background galaxy is lensed by another in the foreground. The extended nature of galaxies allows for this to occur when the source lies exactly on the caustic of a gravitational lens. Complete

rings occur for lenses with perfectly symmetrical mass distributions and when the source is aligned directly behind the lens. Such perfect circumstances are almost impossible in reality, however cases like this do indeed occur. Measuring the diameter of the Einstein ring gives a direct measurement of the mass of the lens interior to the ring – in this case the ring enabled the measurement of the mass of the lens to be $5.2 \times 10^{12} M_{\odot}$ [9], which was claimed as the highest mass lens galaxy at the time. Similarly, giant arcs are segments of Einstein rings that typically are formed of overlapping multiple images of galaxies that have been distorted along the critical curves. Extremely rich clusters such as Abell 370, as shown in Figure 1.5, are very efficient gravitational lenses and hence produce many luminous arcs of lensed background galaxies. These, along with other multiply-imaged galaxies, can allow the underlying mass distribution for the cluster to be determined via the lens equation [10, 11]. This is an important measurement to make for rich galaxy clusters, where the mass distribution is much more extended and complex than for singular galaxies, and hence can vary significantly between different objects. By accurately modelling the mass distribution of the cluster, one can know the locations of the critical curves to search for galaxies that will have been magnified by large amounts. Such methods are applied in order to locate very high redshift objects that would have been impossible to resolve without the boost in flux from gravitational lensing (e.g. [24, 25, 26, 27, 28, 29, 30]).

1.3 Explosive transients

An astronomical transient is defined as any source that significantly changes its flux output over some timescale. Such objects include a wide variety of phenomena including (but not limited to) supernovae, quasars, variable stars, gamma-ray bursts and exoplanets transiting their host star. They are not restricted to electromagnetic radiation either, so gravitational waves are also considered to be a transient source. An *explosive* transient can be defined

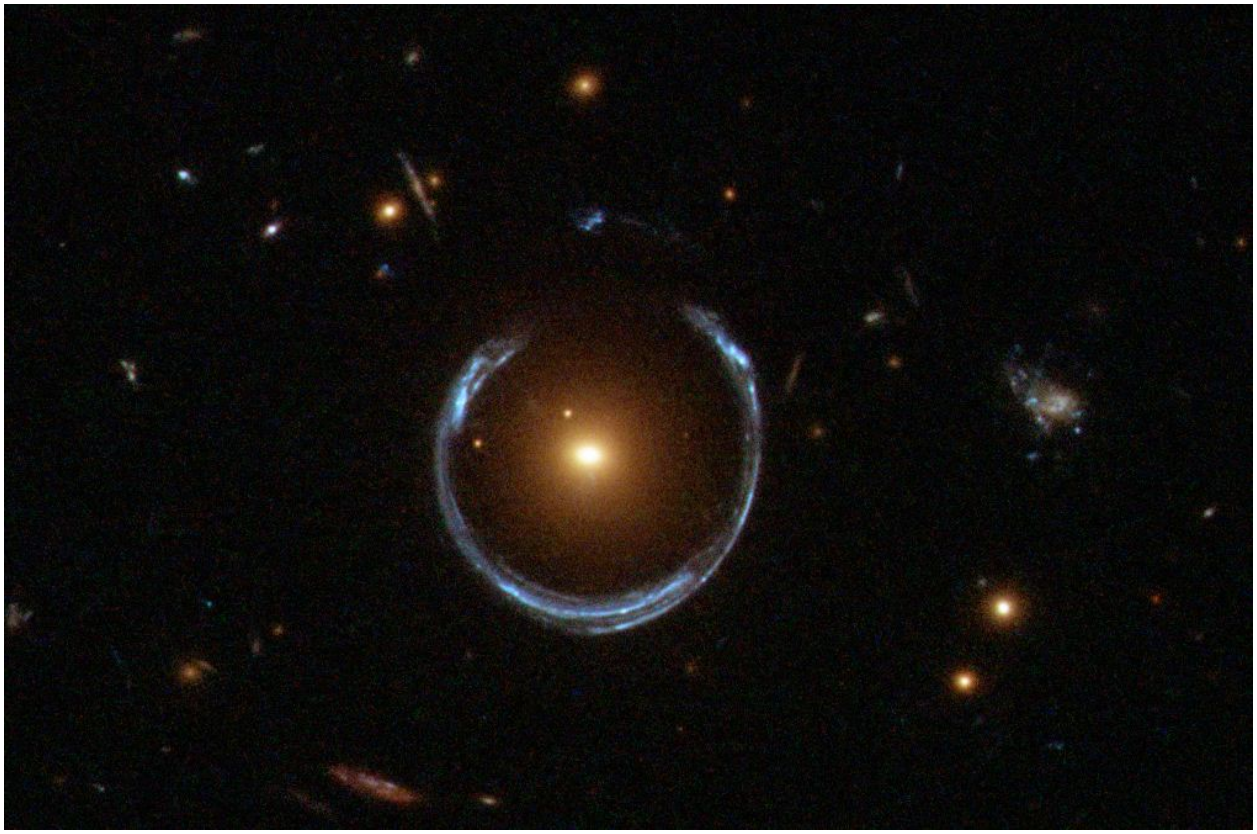

Figure 1.4: A *Hubble Space Telescope* image of the 'Cosmic Horseshoe' [9] – a near-complete Einstein ring formed of a high-redshift ($z = 2.379$) background spiral galaxy being lensed into five overlapping images by the massive foreground galaxy LRG 3-757 ($z = 0.444$). This example is particularly spectacular due to the combination of the high intrinsic luminosity of the background galaxy and the high mass of the lens, which results in a large magnification of the brightness of the source. Detailed modelling of the system allowed for the mass of the lens interior to the ring to be determined at $5.2 \times 10^{12} \mathrm{M}_{\odot}$, one of the most massive lens galaxies to be discovered to date. Image credit: ESA/NASA Hubble.

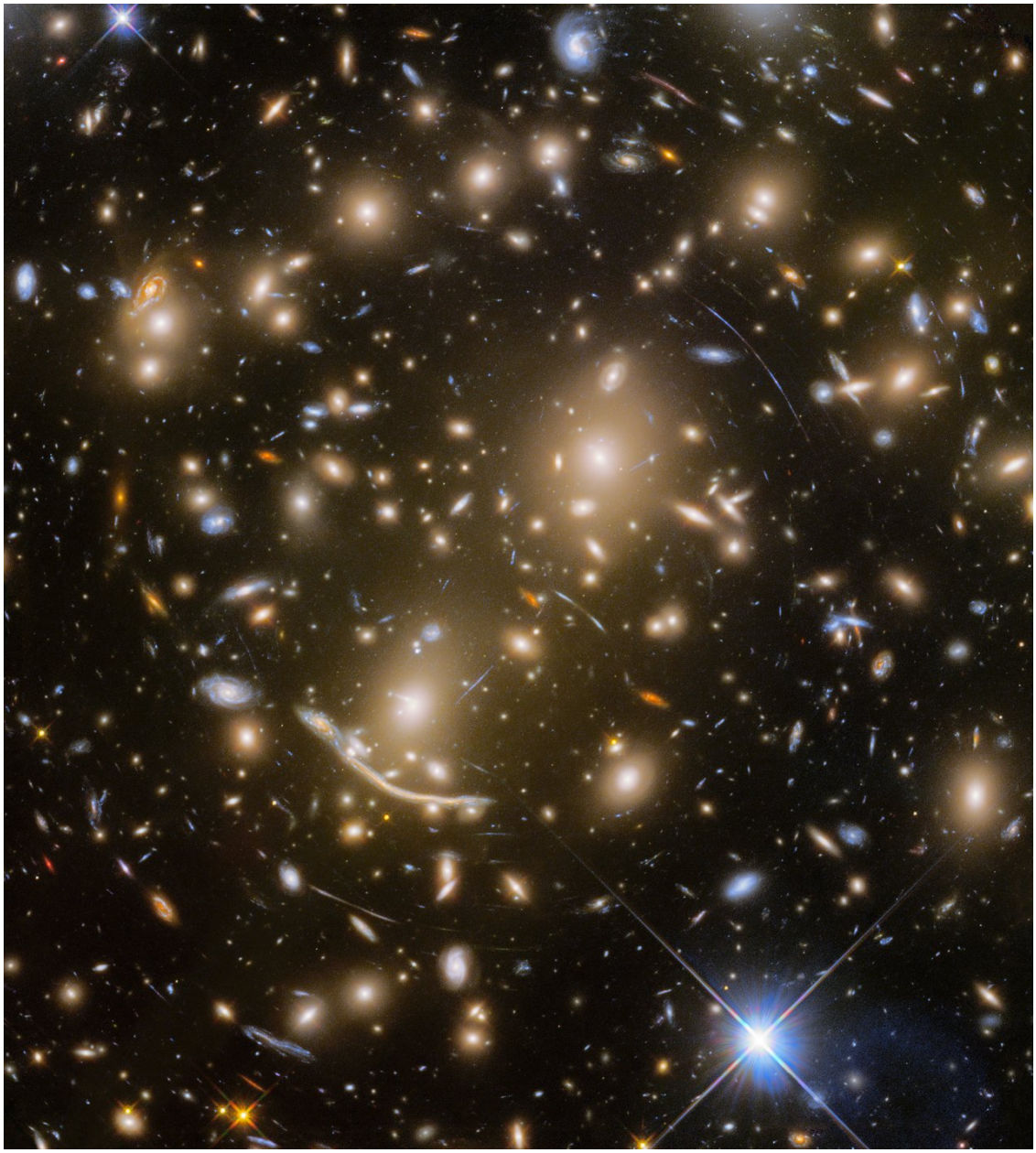

Figure 1.5: The strong gravitational lens and massive galaxy cluster Abell 370, imaged by the *Hubble Space Telescope*. The cluster consists of many red elliptical galaxies which can be seen glowing bright and golden in this image. The background lensed galaxies are seen as bluer, thin arcs. Tangential arcs can be seen tracing parts of circles around the centre of the cluster, whereas radial arcs appear elongated and pointing toward the cluster centre. The cluster's large mass ($\sim 10^{15} M_{\odot}$ [31]), of which $\sim 90\%$ is contributed by its dark matter halo, lends itself to being a very efficient gravitational lens. The broad arc just to the bottom-left of the cluster centre was the first of its kind to be discovered [24, 32]. Image credit: ESA/NASA Hubble.

as a relatively short (rough timescale of weeks to months) and non-repeating source, and includes supernovae, gravitational waves (and their electromagnetic counterparts, kilonovae), gamma-ray bursts and fast radio bursts [33]. Since explosive transients are the main focus of any work involving transients within this thesis, I will hereafter often refer to them just as 'transients'. I also will not discuss fast radio bursts any further in this thesis, as I have not been involved in any research which directly relates to them.

1.3.1 Supernovae

Supernovae (SNe) are by far the most common class of explosive transient that are detected. They are cataclysmic explosions formed at the end of a massive star's life-cycle once all the material in the star that can support nuclear fusion has been exhausted and the star collapses, expelling some of its material at high velocities up to a few percent of the speed of light. The prolonged glow of a SN comes from the radioactive decay of heated material expelled during the explosion, and gives rise to the characteristic light curves that are underpinned by the supernova's *type* – broadly referring to the composition of the elements that are present within each of their spectra. For example, the largest subdivision of supernova types splits the population between Type-I and Type-II, depending on the lack of or presence (respectively) of hydrogen within their spectra. The most commonly observed SN are Type-Ia, which are believed to arise from the accretion of material from a companion star onto a white dwarf. This accretion can lead the white dwarf to exceed the Chandrasekhar mass limit (approximately $1.44 M_{\odot}$) and initiate its collapse. In this scenario, since the limit for the collapse to initiate is approached gradually, the conditions achieved before each Type-Ia explosion are all very similar. In addition, the peak luminosity of a Type-Ia has a strong correlation with the rate at which the observed brightness of the supernova falls off post-peak, meaning they are all standardisable and can hence be used to calculate distances based

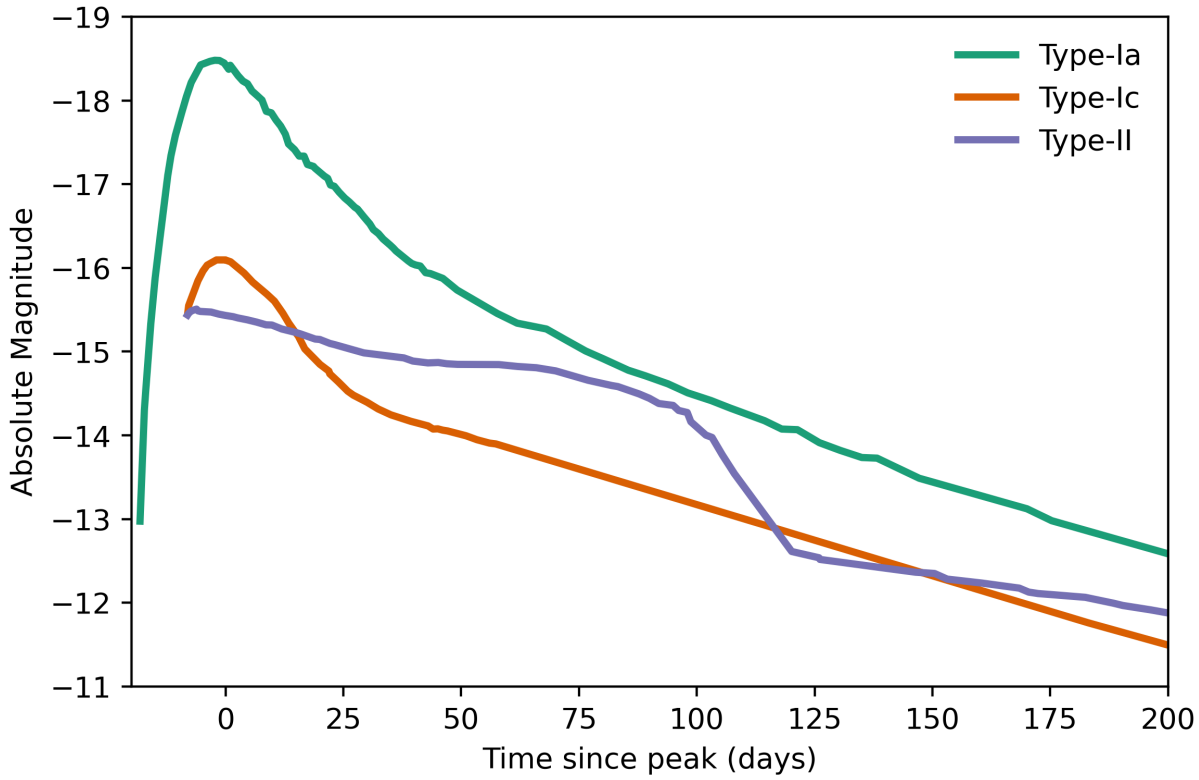

Figure 1.6: Typical lightcurves for the three most commonly-occurring SN types [34]. The Type-Ia is SN2011fe, Ic is SN2007gr and II is SN2004et (a type II-P). Lightcurves are often very similar between Ib and Ic, as is the case with the Type-IIs, hence the omission of the various subtypes.

Table 1.1: Rates and progenitors for different supernova types. Note that Type-II SNe are split into a few subclasses based upon the properties of their progenitor star. Data in this table are taken from [36].

SN Type	Rate (%)	Progenitor Type
Ia	$24.1^{+3.7}_{-3.5}$	White Dwarf
Ib/c	$18.7^{+3.5}_{-3.3}$	Wolf-Rayet Star
II-P	$40.0^{+2.9}_{-3.3}$	Red Supergiant
II-L	$5.5^{+2.3}_{-1.8}$	Low-H Supergiant
II-n	$4.9^{+1.9}_{-1.8}$	Supergiant in dense circumstellar medium
II-b	$6.8^{+2.2}_{-2.1}$	Supergiant stripped by companion star

on the inverse square law [23]. Other SNe result from the core collapse of very massive stars ($M \gtrsim 8\ \mathrm{M}_\odot$ [35]), and are split into subclasses based upon their elemental composition that is generally governed by the properties of the progenitor star. Figure 1.6 shows some examples of real supernova lightcurves that are very typical examples of their individual classes. Type-Ia are the brightest class of SNe (besides the much rarer class of 'superluminous supernovae' [34]), which lends to their ease of detectability, and show a simple rise-and-fall curve that peaks 1-2 weeks after the initial explosion before beginning to drop off. Type-II SNe typically retain their brightness for longer, and show a distinct 'plateau' in their lightcurve. Such features can be used to classify SNe in the absence of high-SNR spectroscopy.

Table 1.1 shows the rates for various types of SNe, along with their progenitors. Type-Ib/c refers to the other hydrogen-poor supernovae that are further categorised based on whether they (respectively) contain helium or not, and are commonly grouped together due to their similarities. Type-II SNe are split based upon their spectral features, which is ultimately driven by the progenitor. The most common of these is the Type II-P, which form from red supergiants, although other types exist such as the II-L which form from

hydrogen-deficient supergiants and II-n that occur when SN ejecta interacts with gas in the environment surrounding the star [37]. In addition, a SN II-b forms from a supergiant that has lost most of its hydrogen layer, likely due to interaction with a binary companion [38]. This list is not complete, however, as there are other rarer classes of Type-II SNe that are rarer ($\lesssim$ 1% of SNe) and hence are less-studied. The most famous example of this are 1987A-like (sometimes known as II-pec) SNe, which takes its name from an event that occurred in the Large Magellanic Cloud – a dwarf galaxy neighbour of the Milky Way. This is particularly notable for not only being the closest observed supernova in over 400 years, but also for its peculiar blue supergiant progenitor [39] that was confirmed by finding a particular star missing after follow-up observations. Such an event was thought to be peculiar as stellar evolution models did not expect these stars to be capable of producing SNe [40], however this event unsurprisingly altered the understanding of core collapse SNe formation to include such progenitors.

1.3.2 Gamma-ray bursts

A gamma-ray burst (GRB) is a non-repeating burst of high-energy/short-wavelength γ photons which are thought to emerge either from either the collapse of a massive star or the merging of two compact neutron stars, producing a signal which can vary in length depending on the progenitor. They typically last from orders of hundredths of a second up to thousands of seconds, forming a bimodal distribution that consists of two families of 'long' and 'short' bursts [41], defined by their 'duration' T_{90} – the time during which the central 90% of the total burst energy is emitted. Long and short GRBs are characterised by $T_{90} > 2$s and < 2s, respectively, although these boundaries are fairly empirical and do not represent a distinct cut-off for the length of bursts based upon physical processes occurring due to either merging neutron stars or collapsing massive stars, and there is certainly some overlap

between durations of the longest short-GRBs and the shortest long-GRBs [42].

GRBs are extremely high-energy events, emitting $\gtrsim 10^{51}$ergs over the duration of the transient (for reference, it would take the Sun over 8 billion years in its current state to emit this much energy). The discovery of GRBs was serendipitous, following from satellites launched by the US to detect terrestrial nuclear detonations that recorded spikes of gamma ray emission that could be roughly localised based on the delay in arrival time at different satellites [43]. Their stochastic distribution ruled out a local origin for the bursts and led to the conclusion that they must be astrophysical sources from beyond the solar system. With the launch of the *Compton Gamma Ray Observatory* in 1991, astronomers were able to identify the two families of GRB and finally verify that they are extragalactic sources, given that there was no bias toward detecting them within the galactic plane [44].

Short gamma-ray bursts are expected to follow from the merger of two neutron stars and occur when material from a disk remnant of the merger falls into the newly-formed NS or BH [42]. The γ-ray emission is expected seconds after the merger, leading to a clear temporal association with the GW signal. The GRB itself is extremely luminous and emits the γ photons in a collimated relativistic jet with opening angle $\lesssim$10 deg. Due to this, an observation that is off-axis with respect to the jet will not observe it, although the opening angle of the jet can widen over time and come into view if only slightly misaligned with the axis [45]. Following the base jet emission, the high-energy jet ejecta interacts with the interstellar medium surrounding the remnant to produce an 'afterglow' of emission that can span across the entire EM spectrum from radio to x-rays. This afterglow is collimated similar to the initial jet is, so is not always observable. In contrast, an isotropic source of photons is also produced stemming from radioactive elements that are produced and ejected during the merger – this is known as a kilonova (these are explored further in subsection 1.3.3) and due to the isotropic nature can, at least in theory, be detected independently of the GRB.

The relativistic jets of long gamma-ray bursts are similar to those of short bursts, except are produced following the collapse of massive stars. Given that these bursts are associated with the end of a massive star's life-cycle, (core collapse) supernovae are often discovered in tandem (e.g. [46]). In a similar vein, they are often discovered in spiral galaxies with active star formation – a prerequisite for massive stars. Long GRBs similarly produce an afterglow, however in this case it is caused by interactions of the jet with the circumstellar medium as opposed to a disk of NS material, and optical kilonova counterparts are not expected due to the lack of synthesised r-process elements. More generally, observations have shown that long GRBs tend to be produce softer (lower-energy) γ-rays than short bursts [47], and that long bursts experience a longer *spectral lag*, i.e. the time difference between receipt of hard and soft photons [48]. Hard and soft emission from short GRBs is generally coincident (within order of ms), indicating further differences between the two types of source.

1.3.3 Gravitational waves and kilonovae

A gravitational wave (GW) is an oscillatory distortion of space-time that travels at the speed of light, formed by accelerating mass, similar to how electromagnetic (EM) waves are created by accelerating charge. GWs act to deform space in dimensions perpendicular to the direction of propagation of the wave, affecting everything they permeate (see Figure 1.7). Mathematically this is represented by a perturbation on the spacetime metric. The first observational evidence for the existence of GWs was found by Hulse and Taylor in 1975, where they were able to show that the orbital period of the binary pulsar PSR B1913+16 was decaying at a rate which matched general relativity's predictions of energy loss by emission of GW radiation [49]. However, it is the ability of GWs to deform space that allowed for the first direct detection to be made on 9 September 2015 by the Laser Interferometer Gravitational-

Wave Observatory (LIGO, [50]). As the name suggests, the two LIGO detectors, located in Hanford and Livingston, USA, are ground-based laser interferometers, each with two arms 4km in length. The lasers propagating along these arms measure precise changes in the arm's length to detect the effects of GW radiation emerging from the coalescence of compact astrophysical objects, such as neutron stars (NS) and black holes (BH) [51]. These sources have masses of ~ 1.4 to $2M_\odot$ (for NS sources) or $\gtrsim 5M_\odot$ (for BHs), and if they merge at distances of up to a few hundred Mpc from Earth, will produce GWs detectable by current interferometers. The amplitude of GWs is known as the strain, and defines the factor change in length caused by the wave. The typical strain of detected GWs is $\sim 10^{-21}$, hence the arm length of the interferometers is altered by an amount one-thousandth of the width of a proton – this highlights the incredible precision that has been achieved by interferometric detectors.

Since September 2015, GWs have regularly been detected throughout multiple observing runs using a growing network of detectors, that now forms the LIGO-Virgo-KAGRA (LVK) collaboration. This began with the two LIGO instruments, now includes two more detectors – Virgo in Italy and KAGRA in Japan – and will soon expand further to include more instruments including one planned to be built in India (LIGO-India). As of writing, the collaboration is between their third and fourth observational runs 'O3' and 'O4', respectively, with O4 due to start in March 2023. 90 high-significance GW events have been published from the first three observing runs, which mostly consists of binary black hole (BBH) mergers, but also star-black hole mergers (NSBH) and binary neutron star (BNS) mergers [53].

Studying GWs has many applications for future developments in astrophysics and cosmology. Firstly, they permit observations of BNS and BBH systems (GWs provided the first direct evidence for the existence of BBH systems), and allow for detailed study of their populations, structure and evolution [53]. Directly observing GWs allows for the estimation

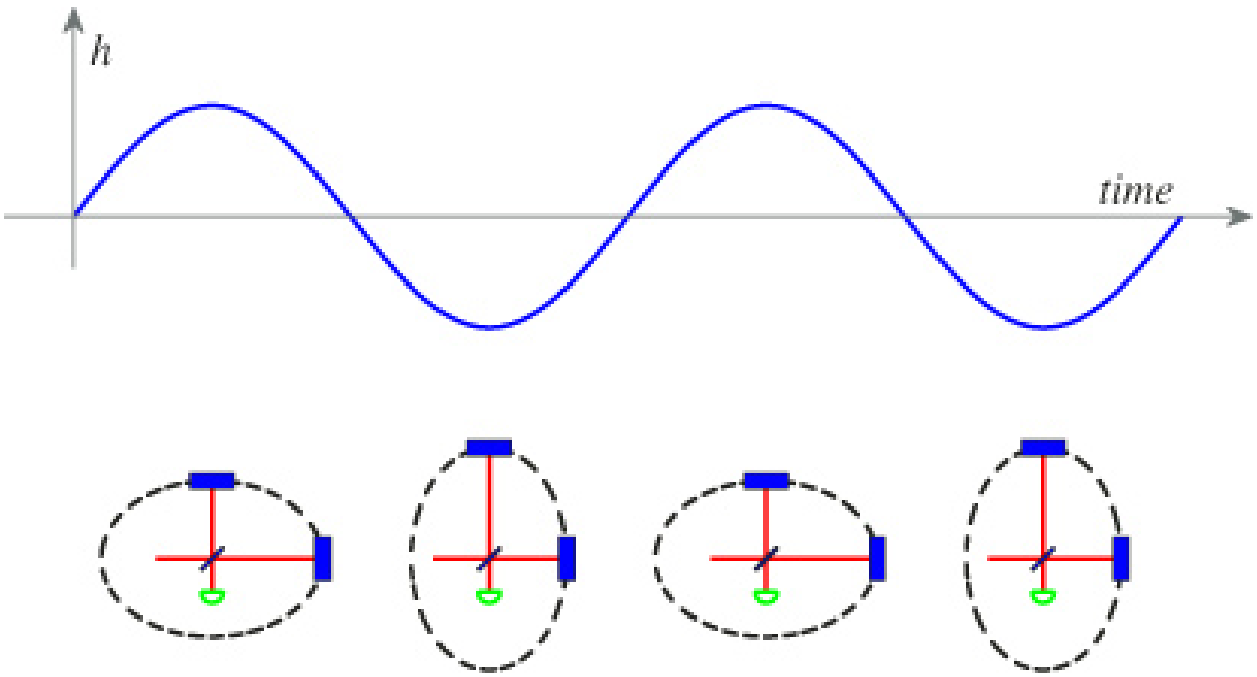

Figure 1.7: From [52]. A schematic view of the effect of a GW passing through a detector with equal length arms. The arms experience changes in length equal to the strain amplitude, h, of the GW. The dashed line represents the effect on a circle of test masses, which is warped into an ellipse. In this scenario, the GW is travelling into the page and is "plus polarised", meaning that the increase in length along one axis perpendicular to the direction of travel is equal to the decrease in length of the other perpendicular axis. GWs can also be "cross polarised", which acts at 45 degrees to the plus polarisation. Real GW signals consist of some linear combination of the two polarisations.

of source masses and spins as well as the distance to the merger. In addition, GWs are able to propagate freely through all kinds of matter and are essentially unimpeded as they spread through the universe. This means that they do not suffer from absorption or scattering from gas, dust or the atmosphere, and can also be used to probe conditions in the very early universe – even beyond the surface of last scattering [51]. In addition, GW measurements can be utilised to measure the Hubble constant [54], as well as to directly test the predictions of GR [55].

Binary compact object mergers are also responsible for producing electromagnetic radiation in an explosion known as a kilonova (KN), which follows a BNS or NSBH event. During these collisions, rare and heavy 'r-process' elements are formed in which neutrons fuse with existing nuclei to form heavier elements (known as neutron capture). Elements heavier than iron cannot be formed via fusion reactions, so neutron capture (or similar) reactions are required. Thus, the r-process is responsible for creating approximately half of the elements heavier than iron in the periodic table – and BNS/NSBH mergers are the only astrophysical environments within which the r-process is currently known to occur. Therefore, this is possibly the only way in which these elements form in any sort of abundance in our universe. The unstable of these elements begin to undergo radioactive decay as they are released, producing the photons responsible for the glow of the KN that we can then observe. In contrast, BBH collisions are not thought to eject a significant amount of material and hence are not thought to have associated electromagnetic counterparts – although a potential candidate has been identified [56].

BNS and NSBH mergers are also thought to be the progenitors of short gamma-ray bursts (see subsection 1.3.2), however the number of detections of optical KNe is dwarfed by the number of detected short GRBs – the *Fermi* satellite detected $\sim$ 400 short GRBs during its first ten years of operation [57]. Comparatively, only a handful of KNe candidates and discoveries have been discovered to date (e.g. [58, 59, 60, 61, 62, 63]). Of these,

[59] is the most notable example; an optical kilonova counterpart was detected following the LIGO/Virgo detection of GW170817[1], which is the only of its kind to be detected following a GW alert and the only multimessenger event to date that involves detection of GWs. Detections of an optical counterpart following GW alerts are not common, as they are complicated by the size of the GW localisation maps, which for previous observing runs have typically spanned hundreds to thousands of square degrees [64, 53, 65]. Given that optical kilonova lightcurves peak within approximately a day of the merger, current observatories struggle to observe the entire localisation to sufficient depth. In the case of GW170817, the sky localisation was much smaller (~ 30 deg^2) due to the merger being very local (40 Mpc from Earth, $z = 0.0098$) and the fact that three detectors – both LIGO instruments and Virgo – were involved. This all lent itself to a favourable chance for detection of the kilonova. In general, the localisation can be minimised by detection with a greater number of instruments [66], one motivation for the construction of KAGRA and LIGO-India. However, with an optical counterpart identified the GW can be localised to its host galaxy which in turn permits the true source redshift to be determined. Knowing the redshift reduces the degeneracies present in GW analysis, for example between the mass and redshift, and in turn results in more precise estimates of the source parameters. This is an example of one of many symbiotic relationships that exist with the science done between GW and EM observers.

Approximately 1.7s following the detection of GW170817, a short GRB was detected by the *Fermi* and *Integral* satellites, but the source was outside of the view of the Swift x-ray observatory which is usually used to better localise the source. Despite this, the afterglow of the GRB was still detected in radio and optical (once the KN had faded sufficiently) wavebands. The KN itself (official designation AT 2017gfo) was discovered simultaneously by multiple observing programmes using various strategies and was thoroughly observed in

[1]Secure GW detections are named with the GW prefix, followed by the date of detection in format YYMMDD, in this case referring to the 17th of August 2017.

multiple bands ([67] and references therein). This allowed fitting of kilonova models and ruled out the possibility of the transient being a SN, which are typically brighter and decay much more slowly than was shown by the observations of AT 2017gfo. Prior to this, only KNe candidates had been detected in the aftermath of GRBs, with no secure detections. Since 2017, there have now been additional KN detections and further candidates although none were accompanied by detected GW signals [58, 60, 61, 62, 63].

1.4 Gravitationally-lensed explosive transients

Combing lensing with detections of explosive transients induces many new applications involving the nature of transients themselves, cosmology and fundamental physics. Many of the consequences of lensing apply generally to all transients, such as the effect of magnification boosting flux received from those sources which makes it easier to detect faint and/or high-redshift objects. Of course, some applications are already possible with lensing that doesn't involve explosive transients, such as utilising lensed quasars[2] to measure the Hubble constant – however employing other sources promises some distinct advantages that can improve on current methods for greater return. However, these approaches naturally come with their own challenges to solve and difficulties to overcome. The aim of this section is to give an overview of these applications and their merits, and how to tackle some of the complications with the methods. Much of the information in this section follows from a recent review on the topic [33].

[2]Whilst quasars are a class of transient, they are not considered *explosive* transients.

1.4.1 Lensed transients as cosmological probes

Lensing affects all transients just as it affects any point-source – multiple images can be formed with a time delay between the arrival of these images, and each image can be strongly (de)magnified. In particular, SN lightcurves are well-studied in the literature and benefit from having a relatively short and simple rise-and-fall form (as in Figure 1.6), compared to the long and stochastic nature of the more commonly-studied quasar lightcurves. This lends itself to being able to easily determine precise time delays (and hence values of H_0) using lensed SNe, as observations only need to be taken over the lifetime of each image of the SN (the peak lasts ∼weeks), as opposed to the many years required with quasars in order to overcome the random fluctuations and obtain a precise time delay measurement [20]. More specifically, Type-Ia SNe have additional benefits that lend themselves to being ideal candidate lensed sources. Because of their standard candle nature, their absolute magnitudes can be well-constrained and this automatically provides an estimate of the lens magnification which is valuable for its ability to break the mass-sheet degeneracy that would otherwise add additional uncertainty when determining the lens' mass distribution [68], another ingredient required for H_0. Knowing the lens' mass distribution well is essential for being able to derive the Hubble constant precisely, therefore the free magnification estimate provided by the lensed SNe Ia is indispensable.

Even if the SN is not Ia, once it fades the host galaxy is no longer inhibited by light from the transient, unlike with quasar hosts. This is advantageous for making observations of the lensed host galaxy, which are beneficial for a number of reasons [69]. Firstly, measuring the shapes of lensed galaxies will provide information on the lens' mass distribution. Secondly, it permits spectroscopy to be more easily carried out on the host providing access to measurements of the host's velocity dispersion, as well as the redshift (also the velocity dispersion and redshift of the lens, in the cases where the lens is also a single galaxy rather

than a cluster, such as [70, 71]). It should be noted that this advantage is shared by all lensed explosive transients, however, and is not specific just to SNe.

Because of the shorter observation time associated with supernovae, this implies a susceptibility to microlensing, an effect which is normally averaged out from quasar observations over the long temporal baseline. However, the microlensing effect on Type-Ia SNe can be effectively negated using 'colour' lightcurves [72], i.e. lightcurves consisting of a difference of magnitudes in two separate bands. This works because the flux magnification due to microlensing from the SNIa in different bands is wavelength-independent during the first ~ 3 weeks after explosion, meaning a colour lightcurve cancels out any microlensing present. At times following this, the supernova shell expands and cools, which changes its elemental composition[3] and in turn changes the absorption and emission processes that are occurring. Due to these changes, the emission is no longer spatially uniform for different wavelengths of light, meaning different bands are now susceptible to varying levels of microlensing and this technique can no longer be applied. In general, this lack of 'monochromatic' emission later in the lifetime of a SN is not an issue as one typically only wants to use the peak to calibrate time delays. Using this method to eliminate microlensing effects, time delays can be measured to a precision of less than 1% [72]. However, this technique will not be tractable in all cases, since the signal in the colour lightcurve depends on the difference in flux in the different observation bands. This requires that the peaks in the lightcurves in individual bands be either offset from each other in time, or have significantly different amplitude in order to retain a prominent signal that can be used for comparison between different images of the SN. Simulated lightcurves in [72] indicate that the colour signal does not exceed 1 mag within 20 days of explosion, with the largest signal in $R - I$ colour. Therefore for this method to be worthwhile, the photometry needs to be high S/N in order to locate any peaks accurately, and thus outweigh the inherent uncertainty introduced by microlensing that this

[3]Specifically Fe-III $\rightarrow$ Fe-II transitions

aims to remove. Such a situation would be valid for a low-redshift and/or highly-magnified lensed SNIa.

SNe are also not the only transient that can be utilised for time delays. Lightcurves for GRBs and GWs (that we currently detect) are very short in comparison to the optical transients we observe. In addition, they typically consist of a single large spike in signal, which would make the time delay estimate easy to make. The typical lengths of these signals are $\lesssim 1$ second, which immediately provides a very precise time delay measurement compared to those recorded using many years of quasar observations [73, 74].

The time delay is only one of the parameters that needs to be well-constrained to measure H_0 – the others being the lens mass distribution, the external effect of lensing (the *external shear*) from extraneous mass along the line of sight, and the true redshift of the source[4]. Modern lens modelling techniques (e.g. those used in [75]) allow the mass distribution of a quasar lens to be determined to precisions of a few percent. However, in the absence of the bright quasar source which introduces further systematic errors as it needs to first be extracted from the image, this can be reduced to sub-percent precision [74]. The external shear of a lensing system can be determined by considering the lensing effect from reconstructing the mass distribution along the line of sight using observational constraints and tracing light rays through simulations. The external shear is then the additional shear required for the simulations to replicate the observed lensing effect. Some authors claim this effect is fairly negligible in most time-delay systems, and affects the measurement at the sub-percent level [76], whilst others believe the external shear introduces significant systematics into the determination of H_0 [77]. In either case, this will become relevant as the other sources of uncertainty are continually decreased through the techniques described here. Finally, the true redshift of the source can usually be determined by spectroscopy for

[4]The lens redshift also needs to be determined, although this is usually less problematic, as lens galaxies tend to be massive, bright galaxies and/or members of prominent groups or clusters.

high-SNR transients, or by similar observations of the host galaxy. However, in the case of GWs, due to the large sky localisations the host galaxy is incredibly difficult to determine unless an associated optical counterpart is discovered. Therefore, lensed GWs emerging from BBH systems or those without detected counterparts are less than ideal for time delay measurements, and are almost impossible to detect robustly in the first place.

1.4.2 Utilising lensing for studies of EM and GW transients

As mentioned previously, the effect of magnification causes an increase in the apparent magnitude of a background source by an amount $\Delta m = -2.5 \log(|\mu|)$. This effect can allow faint objects that are below the threshold of a magnitude-limited survey to be securely detected, and hence bypass implicit limits on the detection of high-redshift sources. This effect is not just limited to EM sources – GWs experience lensing through an increase in flux of factor μ, equivalent to EM radiation, which results in an increase of the strain amplitude by factor $\sqrt{\mu}$, increasing their detection capabilities compared to those that are not lensed. This can give insight into populations of EM and GW progenitors from earlier cosmic time, although numbers are likely to be small given the rarity of high-magnification lensing.

The lensing effect on GWs is important to consider in general, as incorrectly inferring the magnification will cause other parameters estimated from the signal to be incorrectly inferred as well. The strain amplitude of a GW is inversely proportional to the luminosity distance $D_{\rm S}^{\rm L}$ of the binary merger [64], just like for EM waves, forming the relation $A \propto \sqrt{\mu}/D_{\rm S}^{\rm L}$. As the response of a detector is based solely on GW amplitude, there is a degeneracy between the distance and magnification. Because of this, a lensed event can easily be misinterpreted as a non-lensed event occurring closer by. This is also problematic for determining the masses of the progenitors, as the redshift is required in order to measure them. This is because the compact object's masses affect the rate at which the frequency of the GW signal

changes, and this is utilised to measure the masses of the system. However, because the GW signal is affected by cosmological redshift, the observed frequency needs to be corrected in order to infer the true frequency, and thus the progenitor masses [78]. The total mass of the binary (the sum of the progenitor's masses) transforms as $\widetilde{M} = (1+z)M$, where M is the true total mass and $\widetilde{M}$ is the redshifted total mass. Therefore, by wrongly assuming $\mu = 1$ when the source is lensed, the luminosity distance is underestimated by a factor μ and this results in an overestimation of the mass.

A strongly-lensed transient will be multiply imaged, with the images arriving at different times. If one image is detected before the appearance of any others, by precisely determining the time delay one can plan exactly when observations should take place in order to directly observe transient events as they occur. Therefore one can obtain very early measurements of the transient's lightcurve [79] that would otherwise evade observation. In particular, in the case of supernovae this would permit observation of the shock breakout phase that occurs at the very beginning of the SN explosion, which are required in order to fill gaps in our understanding of stellar evolution and transient progenitors [80].

Finally, the lensing rate of lensed transients can be used to constrain the redshift distribution of said transient. The origin of such a method is due to the increasing rate of gravitational lensing for sources at higher redshifts (e.g. [81]). Therefore, based on the observed number of strongly-lensed sources from a statistically-large sample, one can infer their average redshift. Such a method was first utilised to constrain the redshift distribution of GRBs [82], when their true origin as cosmological sources was not yet well established, despite over a thousand detections. Since then, a similar method has been suggested for constraining the progenitors of fast radio bursts, since different possible progenitors are expected to follow different redshift distributions [83].

1.4.3 Identifying lensed transients

SNe are a common transient as any galaxy can host them (although typically only Type-Ia are found within elliptical galaxies that have ceased star formation, and the other core collapse SNe are found within the high star-forming spiral galaxies). However, locating them is essentially down to chance as it is not known in advance when or where one will occur. Therefore, the most effective strategy to locate as many as possible is to scan the entire sky as often as possible and use an automated system to look for sharp increases in flux at every point (with respect to some reference sky image). This is essentially the concept of a survey being conducted by the Zwicky Transient Facility (ZTF [84]), which to date has discovered around 6000 supernovae, among many other transients. In the next few years, the Rubin observatory will commence operation and will begin the Legacy Survey of Space and Time (LSST), which will scan the entire sky above the southern hemisphere once every three nights to unprecedented depth [85]. This will operate in a much similar vein to ZTF and over the course of this ten-year survey, it is expected to discover upwards of 10^7 supernovae. Discovering a lensed SN is much less common – only one in $\sim 10^{3-4}$ SNe will be strongly lensed [86, 87] – although such numbers are easily achievable with the scale of LSST.

Confirming that a SN has been strongly lensed requires the multiple images to be resolved and spectroscopy utilised. Performing such a feat for every SN discovered in surveys such as LSST or even ZTF is unfeasible given that ground-based telescopes often have difficulty resolving objects separated by arcsecond scales (the typical separation of lensed images) due to atmospheric seeing, let alone the time and resources required for spectroscopic observations. As such, other information should be utilised in order to significantly narrow down candidate lensed transients. One way to do this would be to look for transients with coincident positions, under the assumption that these sources have been multiply imaged. Whilst there are cases where this method would certainly result in success, it has its limita-

tions. To begin with, this requires that the transient detections are sufficiently spaced out (either in time or space) such that each is resolved as its own individual transient. If the time delay is less than the cadence of the survey searching for them, or the image separation is less than the point-spread function of the instrument, then it is likely the multiple images would be blended and hence classed as if they were a single transient detection. In addition, each image would need to be bright enough to detect – cases where only a single lensed image is detected would automatically be wrongly classed as an un-lensed source. Lastly, this method inherently ignores cases of lensed transients that are singly-imaged but still magnified – [12] estimates that a significant fraction of lines-of-sight relevant to transients lensed by clusters with $\mu = 10$ will produce single images, and likewise 10% of those magnified by $\mu = 100$. Therefore a non-negligible number of sources can still be significantly magnified without producing multiple images, and this method would be inherently insensitive to these cases.

As for GWs, it is much more difficult to determine whether an event has indeed been lensed or not. This is dominantly due to the difficulty to localise them to a particular host galaxy because of the large sky localisation maps. If detected, a multiply-imaged GW would appear as two unique triggers each with its own localisation map. Overlaps within these maps could be used to constrain the search region for possible host galaxies, although current scales of localisation ($\gtrsim 100$ sq. degrees) are many orders of magnitude from being able to constrain sky regions to individual galaxies. Observation of a multiply-imaged kilonova counterpart alongside one or more gravitational wave images would be a smoking gun [88], although the vast majority of GW signals originate from BBH mergers that do not produce EM counterparts [65]. Alternatively, evidence for the lensing of GWs can be inferred from the GW population in a number of ways. For example, [89] compared the observed population to the expectations of progenitor models and whether their distribution required a lensing interpretation in order to be consistent. Searching for a 'Morse phase', where a particular phase shift is applied between each image of the GW that corresponds to the same source,

can provide further evidence for the lensing of GWs directly within the signals themselves [90, 91]. In addition, one can look for statistical similarities in the estimated parameters of pairs of GW detections [92, 93, 94], under the assumption that these detections would convey similar estimated parameters. Evidence for the lensing of GWs from BNS mergers can be inferred from tidal effects on the GW signal [95], or by searching for signals that imply sources with masses lensed into the supposed 'mass-gap' that exists between observed neutron star and low-mass black holes [12]. Despite many efforts however, no evidence currently exists that robustly suggests any of the GW events detected so far have been influenced by gravitational lensing.

An alternative method for locating lensed transients would be to continually monitor known lensed galaxies, and await for a transient to occur within one. This can be done easily by utilising wide-field surveys such as ZTF and LSST that naturally cover many of these targets during routine observations, however this requires the lensed galaxies to be known about in advance. In addition, since many transients are detectable even when their hosts are not (SNe are optically brighter than a typical galaxy, GWs, GRBs and FRBs are detected with instruments insensitive to galaxy emission) then it is plausible the hosts will not have been discovered in advance or in tandem with the transient. In chapter 2 I discuss this in the context of detecting lensed SNe in optical bands, where their detectability with a given magnitude-limited survey is compared with the detectability of lensed host galaxies behind clusters in the same survey. This study was completed in order to quantitatively analyse the optimum approach for finding transients lensed by galaxy clusters, by considering whether the host galaxies of transients lensed by clusters would be observable in the same discovery images.

The method that promises to be the most effective for discovering the largest number of lensed transients is discussed throughout the later chapters of this thesis. This involves utilising a 'watchlist' of a large number of potential (in most cases unconfirmed) lenses

consisting of LRGs, galaxy groups and galaxy clusters and searching for transients that appear nearby these objects in wide field surveys. This method can be applied to any regularly-detected extragalactic transient and can identify candidates using only routine observations of these surveys. This method is at the forefront of my research presented in this thesis, and will be explored further in the coming chapters.

1.4.4 Further applications

Here I introduce some additional applications of lensed transients that are less directly related to astronomy and more toward fundamental physics. Firstly, lensed GRBs and GWs from BNS mergers can be used to test the relative propagation speeds between photons of different energy and photons and GWs, respectively. The former is relevant as some formulations of quantum gravity predict an energy-dependent change in a photon's speed (see e.g. [96]). GRBs can be utilised for such studies since they are known to produce γ-ray photons with varying energy, including distinct hard and soft components separated by a characteristic time lag [48]. An issue is that this time lag is generally not well constrained, partly owing to the fact that the physics behind GRBs is not fully understood. Strongly lensed GRBs can circumvent this issue, as this intrinsic time lag would be present within each of the multiple images of the burst. This means the time delay between the arrival of similar-energy photons in each image should be completely describable by the lensing-induced time delay. Any deviation from this would indicate evidence for an alternative source of delay – potentially pointing to new physics. This exact same idea can also be applied to multiply-imaged KNe following multiply-imaged GW detections to constrain the speed of propagation of GWs [97].

1.4.5 Previous observations of lensed transients

There are currently very few observations of lensed transients where multiple images have been successfully resolved. Future observatories utilising refined observing strategies within the next decade will significantly enhance these numbers by orders of magnitude, and enable a rich variety of new discoveries by taking advantage of the benefits of lensing. Preceding this, past fortuitous discoveries of multiply-imaged SNe have been made, paving the way forward and drawing attention to the possibilities associated with lensed transients. This section will describe the key lensed transient discoveries that have been made so far, and the impact they have made on the field.

The first transient that is generally agreed to have been gravitationally lensed was the Type-Ia supernova PS1-10afx discovered by the Pan-STARRS1 Medium Deep Survey [98] in 2010. It was initially identified as a very atypical SN – it was too bright for the associated decay in its lightcurve and standard models could not simultaneously predict its temperature, ejecta velocity, colour evolution and spectrum. As a result, it was labelled as a new variety of superluminous supernova [99]. The lensing hypothesis was suggested as an alternative explanation, where the SN is classified instead as a regular Type-Ia that has been gravitationally magnified by a significant amount [100], although this was initially disputed due to the lack of a suitable lens in the SN imagery, a lack of detection of multiple images, and that the evidence for the SN being Type-Ia was ambiguous. However, this prompted further observations of the location of the SN, which revealed additional spectral features combined with those of the host galaxy that indicated the existence of a second, intervening galaxy at lower redshift [101]. This evidence was sufficient to explain the observations – the SN was a usual Type-Ia that had been magnified by $\mu \simeq 30$ (determining this magnification factor is simpler given the standard candle nature of SN-Ia). Subsequent modelling of the lensing interaction utilising this value of magnification predicted the SN to have four images

separated by less than an arcsecond, which explains why multiple images were unable to be resolved by the ground-based instruments involved.

Unfortunately, because the lensing evidence for PS1-10afx was compiled approximately 3.5 years after first detection, the true nature of this transient could not be directly imaged at sufficient resolution. However, it would only be another year until it would be announced that a supernova with resolved multiple images had been discovered. During a scheduled *Hubble Space Telescope* observing programme studying high-z galaxies behind galaxy clusters, a quadruple system of transient point source was serendipitously detected ([102], see Figure 1.8). It was later identified to be a SN and named 'Refsdal' after the seminal paper [19] suggesting the use of multiply-imaged SNe as cosmological probes. Unlike PS1-10afx, SN Refsdal was quickly ruled out from being Type-Ia due to the evolution of its brightness differing from that of typical Ia, and was soon established to be a 1987A-like Type-II SN [103], meaning the magnification could not be easily determined through observations and was hence subject to some uncertainty ($\mu \sim 10 - 20$, depending on the image [102, 104, 105, 106, 107, 108]).

The nature of SN Refsdal is spectacular – its host galaxy had three resolved multiple-images even before detection of the SN [109], meaning one expects at least one image of the SN per host galaxy image. However, one of these images is individually distorted by alignment with a particular cluster member galaxy, again splitting the image of the SN within that image of the host fourfold to the observed Einstein cross configuration (see Figure 1.8). As a result, the image as shown in Figure 1.8 is missing the two SN images from the other host images due to the gravitational time delay. Subsequent modelling showed that one of these had already been and gone ~ 20 years prior, however the final image was predicted to have yet arrived. Predictions for its arrival varied, even up to a few years in the future [102, 104, 105, 106, 107, 108], and the detection of this last image was made on 11 December 2015; thirteen months after the first detection [110]. Because of this relatively long time delay,

the fractional error on the measurement is small and allows a fairly precise measurement of $H_0 = 64^{+9}_{-11}$km s^{-1} Mpc^{-1} with just the one measurement, with the dominant source of error coming from the modelling of the complex galaxy cluster structure [111]. In addition, the appearance of this image was the first opportunity for cluster lens models to be blind-tested – models constructed in advance of the final image were able to be stringently tested on their ability to constrain the location of the image, with no opportunity for prior knowledge to bias results [110].

The second multiply-imaged and resolved SN iPTF16geu was detected on September 5 2016 [70]. It was detected by the Palomar Transient Facility, which acts similarly to an early rendition of the ZTF survey, using nightly repeated observations of particular areas of sky to look for transients via difference imaging [112]. This was identified during routine searches for general transients, and had a spectrum taken as part of this routine programme. The spectrum revealed an intervening galaxy system, and that it is consistent with being a Type-Ia, despite being significantly brighter than is typical (as for PS1-10afx). This all pointed toward evidence for this SN to be gravitationally lensed, which was confirmed via higher resolution imaging from *Hubble* and the Keck Observatory, revealing four images embedded within a partial Einstein ring (Figure 1.9). As a Type-Ia, the magnification could be determined (a substantial $\mu \sim 50$) allowing for precise measurements of the mass distribution, although unfortunately due to the low mass of the lens (a $\sim 10^{10}$M$_\odot$ galaxy), the time delay was too small for precise Hubble constant measurements. In fact, the time delay was not measured as all four images had already arrived by the time the high-resolution imaging was taken. From lens modelling in [70], the average time delay between arrival of successive images was estimated to be between $\sim$ 2 and 16 hours, and no longer than 35 hours (99.9% confidence level) meaning very rapid follow-up would have been required to observe the appearance of the images. Given that iPTF16geu is the only lensed Type-Ia SN discovered by the Palomar Observatory, it is also possible to determine a rate of lensed SNe,

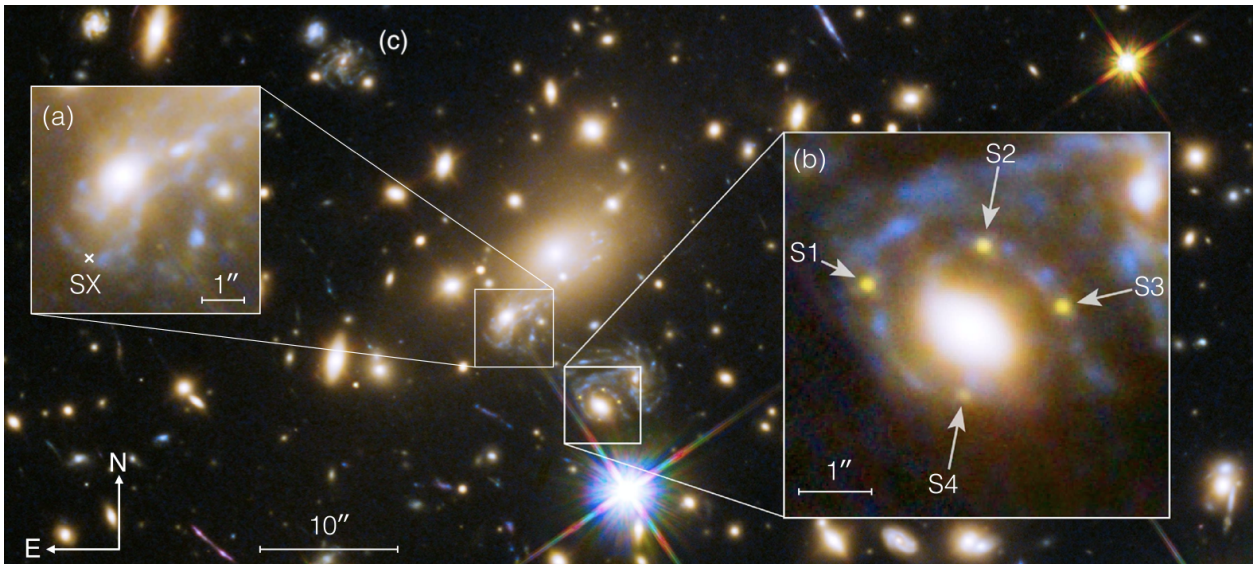

Figure 1.8: *Hubble Space Telescope* image of the multiply-imaged Supernova Refsdal lensed by galaxy cluster MACSJ 1149.6+2223 [102]. Insert (b) clearly shows the four images of the SN, S1-4, that were originally resolved within one image of the host galaxy. Note that these images in particular are formed due to alignment with a cluster galaxy in addition to the underlying cluster dark matter halo that splits the host galaxy into three images. Insert (a) shows a second image of the host galaxy, with SX marked, the location at which a fifth image of the SN appeared approximately one year later [110]. The galaxy labelled (c) is the third image of the host galaxy, where it was predicted a sixth image would have appeared approximately 20 years prior, but was never observed. In particular, the scales of the images should be noted. The host galaxy images are separated by ~ 10 arcseconds, whereas images S1-4 are separated by ~ 1 arcsecond. This shows the difference in scale of image separations created by cluster and galaxy lenses, respectively.

under the assumption the single detection is a good representation of the true rate. This was done in [70], and is reassuring that this rate is broadly consistent with lensed transient rate predictions from ray tracing simulations [81].

The final lensed transient with resolved multiple images, AT2016jka (named "SN Requiem"), discovered to date was only found in 2019 when three SN images were found during the re-analysis of *Hubble* images from 18-19 July 2016 [113]. Due to this, the SN had already faded from view by the time its lensing nature was discovered. This means only essentially one data point exists for this source from the single observation. However, due to the induced gravitational time delay within the multiple images, the three detected images of the SN actually represent the object at three different epochs along its lightcurve. Therefore, if the lens is accurately modelled, three points can populate a lightcurve. This immediately highlights a challenge posed by this system, since the SN was lensed by a galaxy cluster (MACS J0138.0-2155) so the modelling of the mass distribution is inherently complicated compared to a single galaxy lens. Nevertheless, sufficient data exists for properties of the cluster galaxies and the multiply-imaged host galaxy to reasonably recover the positions of the host + SN, and the morphologies of three out of four of the host images following a blind analysis also completed in [113]. Following the modelling of the lens, the lightcurve and colour information more closely resembles a Type-Ia SN, furthermore, the host is an evolved and quiescent galaxy which typically lends itself against hosting core collapse SNe. Based on this evidence, the SN is assumed to be Ia, although further evidence is required in order to confirm this classification, such as spectroscopic observations of a later image – which are predicted by the lens model. In fact, the current lens model predicts the next image to arrive in the year 2037 ± 2 – a ~ 20 year time delay. This would be approximately three times longer than the longest time delay observed to date [114] and would enable an incredibly precise measure of the time delay component of H_0, although at the cost of a long wait and would still be subject to uncertainties in the mass distribution.

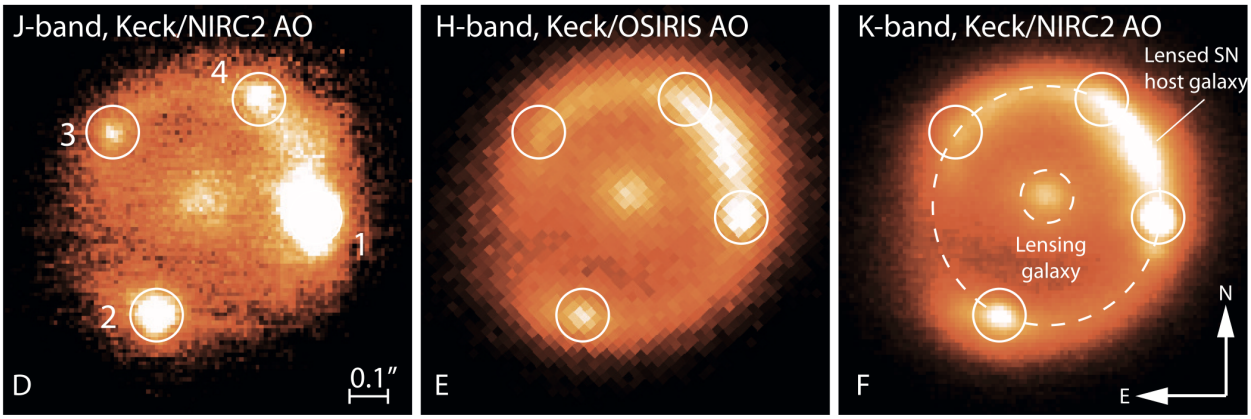

Figure 1.9: Keck Observatory images of iPTF16geu from [70] – the first Type Ia SN with resolved and spectroscopically-confirmed multiple images. In the leftmost panel taken in J the four images are clearly resolved, encircling the central lens galaxy, a $1.7 \times 10^{10} \mathrm{M}_{\odot}$ source at $z = 0.216$. Part of an Einstein ring can be seen more clearly in the centre and rightmost panels, taken in H and K respectively. The relatively low mass of the lens owes to the sub-arcsecond separations. Since the SN was Ia, the magnification was able to be estimated at $\mu \sim 50$ which equates to a boost of over 4 magnitudes compared to if it had not been lensed.

Besides the three multiply imaged SNe, there have been no other transients of any flavour with resolved multiple images. Additional observations of lensed, but not multiply imaged, SNe have been made, where sources are magnified without increasing image multiplicity [115, 116, 117, 118, 119]. In addition to this, there have been searches for other lensed transients, including GRBs [120, 121] and GWs (and optical counterparts) [122, 123, 90, 94, 12], including using methods that are described in more detail in chapter 3 and chapter 4. Despite these efforts, no confirmed detection has been made to date, although searches will continue and expand in scope with new surveys conducted by modern observatories.

1.5 Outline of the science chapters

The next three chapters of this thesis will explore the research I have conducted within the field of strong gravitationally-lensed transients. Specifically, my research focuses on optimising the watchlist-based approach for locating strongly lensed transients that was introduced in subsection 1.4.3. In short, this method requires two key ingredients to function. The first is a list of potential lenses (galaxies, groups or clusters), and the second is a survey that will regularly observe the fields nearby these lenses, searching for transients. Any detected transients that have locations coincident with a lens within the watchlist are therefore potential candidates for being lensed, and should therefore be inspected further to investigate the lensing hypothesis.

In chapter 2, I quantitatively estimate the viability of the watchlist method, and deduce the optimum way to populate a watchlist with galaxy clusters – should it contain all galaxy clusters, or just those that are already known to be lenses? In chapter 3, following on from the results of the previous chapter, I describe a method by which the watchlist of potential lenses can be easily assembled using data from existing wide-field surveys. This

method ensures the watchlist can cover the entire extragalactic sky, and is populated deep enough to cover the entire redshift range of lenses relevant to the lensing of transients. Finally, chapter 4 explores searches that I have been involved in utilising this method, looking for lensed SNe, GRBs and GWs/KNe using a prototype watchlist of galaxy clusters assembled from pre-existing cluster catalogues.

Chapter 2

Paper 1

2.1 Preamble

This chapter is a reformatted and partially edited version of my first-author paper [124]: Ryczanowski D., Smith G. P., Bianconi M., Massey R., Robertson A., Jauzac M., *On building a cluster watch-list for identifying strongly lensed supernovae, gravitational waves and kilonovae* 2020, published in MNRAS, Volume 495, Issue 2, pp.1666-1671.

The study was initially conceived by Dr. Graham P. Smith, however I naturally influenced its direction throughout the project. I was responsible for completing all of the analysis and producing all of the figures, with the pedagogical support of both Dr. Graham P. Smith and Dr. Matteo Bianconi. The other co-authors provided comments on drafts of the figures and text of the paper.

2.2 Introduction

The discovery of Supernova Refsdal marked the dawn of observational studies of strongly-lensed transients [102]. A new generation of wide-field optical surveys (e.g. ZTF [84], GOTO [125], LSST[1] [85]) are now poised to discover large samples of strongly-lensed supernovae (SNe) in the 2020s [87, 126, 127]. The prospects for discovering strongly-lensed gravitational waves (GWs) and their electromagnetic counterparts has also been discussed recently, following the early detections of GWs [122, 88, 123, 128, 129]. There is no clear cut evidence that any of the GW events detected thus far are strongly lensed [89, 130], due in part to the challenge of detecting a strongly-lensed electromagnetic counterpart and thus localization of a candidate lensed GW to a lens.

Search strategies for lensed SNe typically involve cross-matching a list of newly discovered transients with a watch-list of luminous red galaxies [e.g. 87]. Concentrating on individual galaxy lenses is partly driven by the scientific motivation of measuring the Hubble parameter with lensed SNe, which benefits from lower systematic uncertainties arising from simpler lens mass distributions [131, 76]. However, strongly lensed SNe and GWs/Kilonovae (KNe) are expected to be dominated by high magnification events, i.e. those with lens magnification of $|\mu| > 10$, until at least late 2022 when LSST survey operations begin [122, 87]. Calculations using hydrodynamical simulations were carried out by [81] which suggest the mass distribution of high-magnification optical depths for lensed point sources is flat over the range 10^{12}–$10^{14}\mathrm{M}_{\odot}$, highlighting the prevalence of cluster scale lenses which have typical mass $M_{200} \sim 10^{14}\mathrm{M}_{\odot}$. In addition, the cases of high-magnification lensing of point sources detected thus far are indeed dominated by galaxy clusters [e.g. 132, 133, 102, 134]. This motivates constructing cluster-based watch-lists for use along with wide-field surveys

[1] We refer to the Vera Rubin Observatory as LSST throughout this paper, as the change of name occurred during the time of writing.

to detect strongly lensed transients. The search strategy utilising such a watch-list relies on the detections of transient events from wide-field surveys such as ZTF and LSST. Detections found near to a cluster included in a watch-list can then be flagged as candidate strongly lensed transients for follow-up observations, which will confirm if they are indeed lensed. Transient searches are a core component of such surveys, hence the focus of this chapter on how to prepare for finding transients lensed by clusters in their alert streams.

The detectability of lensed SNe/KNe within the LSST era has been studied by several authors recently. Based on simulations, [87] predict that many hundreds of strongly lensed supernovae will be detected by LSST per year. Whilst these simulations were carried out with galaxy lenses, the results of [81] indicate that clusters should lens a comparable amount. KN counterparts to lensed GWs are predicted to be detectable with dedicated target of opportunity observations with LSST in red optical bands, specifically the z-band, within a few nights of GW detection. A typical source will be located at $z \sim 1-2$ and magnified by $|\mu| \sim 100$ [123, 135]. Transient point sources close to the tangential critical curves of strong-lensing galaxy clusters have also been shown to be recoverable close to the nominal 5σ detection limit of LSST-like data [88]. The prospects for detecting lensed SNe and KNe in crowded cluster cores, based on wide-field survey observations and a watch-list of strong-lensing clusters therefore appear promising.

A key question is: how should clusters be selected in order to construct such a watch-list? Strong-lensing clusters can be chosen by searching for visible bright giant arcs and/or multiple images of distant background galaxies [e.g. 136, 137] – we refer to this as source-plane selection. Alternatively, they can be chosen based on the inferred projected mass density of cluster cores [e.g. 138, 139] – a lens-plane selection method. In this chapter, we investigate whether relying solely on "traditional" source-plane selection is sufficient for creating a watch-list for the discovery of lensed transients. We concentrate on answering two main questions. Firstly, what fraction of the progenitors of GW events/SNe can be

found within galaxies whose apparent magnitudes are fainter than the limits of optical wide-field surveys? This is analogous to estimating the fraction of such transients that appear to lack a host galaxy (hereafter, "hostless" lensed transients). A hostless lensed transient (whether GW or electromagnetic radiation) may be the first detectable source lensed by a particular lens, in which case source-plane selection alone could not have identified this lens prior to the transient event. Thus a search using a source-plane selected watch-list would miss all such events. Secondly, we ask what fraction of clusters that are capable of strongly-lensing a transient are identifiable as strong lenses by searching for lensed images in wide-field magnitude-limited surveys, i.e. what fraction are identifiable by source-plane selection? We investigate these questions in section 2.3 and section 2.4 respectively, before summarising our main results and discussing their implications for strongly-lensed transient detection in section 3.6. All magnitudes quoted are in the AB system, and we assume a flat cosmology consistent with the recent Planck data: $H_0 = 67.8$ kms^{-1}Mpc^{-1}, $\Omega_M = 0.308$ [140].

2.3 Hostless strongly lensed transients

We first consider the first question posed in the introduction, in which transients occur in galaxies that are strongly-lensed and yet not magnified enough to be detected in wide-field photometric surveys. In this situation, a watch-list of source-plane selected lenses will not include the clusters responsible for lensing these galaxies, and the lensed transients would appear to be hostless. To quantify how common this scenario is, we consider the fraction of the progenitors of GW events and SNe that reside in strongly lensed galaxies that are too faint to detect in wide-field strong lens searches – i.e. the fraction of progenitors that will evolve into apparently hostless lensed transients, $f_{\rm hostless}$. Specifically, we calculate:

$$f_{\rm hostless} = \frac{\int_0^{L_{\rm lim}} L\,\phi(L)\,dL}{\int_0^{\infty} L\,\phi(L)\,dL}, \tag{2.1}$$

where $\phi(L)$ is the galaxy luminosity function, which is weighted in Equation 2.1 by the luminosity L, and $L_{\rm lim}$ is a nominal limit below which lensed galaxies are not detectable.

This formulation is based on the assumption that GWs and SNe form from stellar remnants, and that the stellar population is traced by the stellar light in galaxies. We base $\phi(L)$ on our Schechter function [141] fits to galaxy number counts from the COSMOS i-band selected photometric redshift catalogue [142]. The fits are performed for galaxies within particular redshift bins, which are described in subsection 2.4.3.

It is important to note that the integrals in Equation 2.1 converge for all of our derived values of the Schechter function faint-end slope parameter, as convergence occurs when $\alpha > -2$. We adopt $z = 1$ and $z = 2$ as two representative redshifts as they are typical of the redshifts at which strongly lensed transients have and will be detected. A single representative value of the faint-end slope ($\alpha = -1.2$) is applied to both redshifts, rather than their individual fit values. Our results are insensitive to this choice, and is within the uncertainties from the COSMOS analysis.

Figure 2.1 shows $f_{\rm hostless}$ as a function of the limiting i-band magnitude of observational surveys. We relate this limiting magnitude to $L_{\rm lim}$ in Equation 2.1, by assuming that all images of galaxies that are strongly-lensed by clusters are magnified by $|\mu| = 10$. The plot shows that a significant fraction of transient progenitors, $f_{\rm hostless} \sim 0.15 - 0.5$, are housed within $z \sim 1 - 2$ galaxies that are fainter than the detection limits of current wide-field surveys, such as the Dark Energy Survey [DES, 143]. This indicates that with present surveys, a significant fraction of lensed transients will be located in lensed galaxies that are not identifiable in magnitude-limited surveys, and thus if the lensed transients are detected they will appear to be hostless. The situation is less severe for sensitivities comparable with that

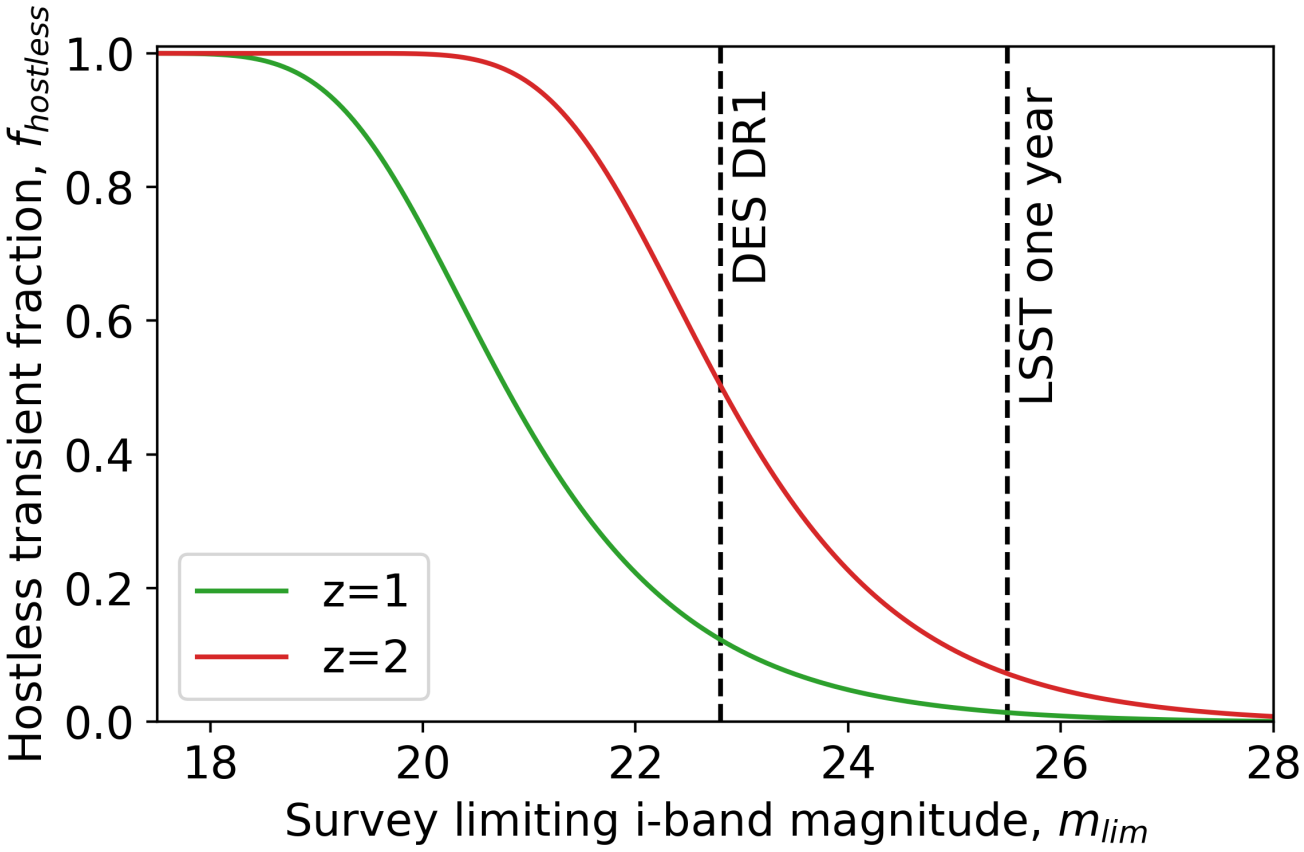

Figure 2.1: Lower limits on the fraction of strongly-lensed SNe and GWs/KNe that will appear to be hostless. Such transients occur in strongly-lensed galaxies that are too faint to be detected in magnitude-limited searches for strong-lensing clusters based on the detection of multiple images and arcs. These hostless lensed transients would not initially be identified as lensed, based on strong-lensing cluster watch-lists constructed solely from source-plane searches. The curves are plotted as a function of the depth to which strongly-lensed galaxies are identified in wide-field survey data. Prior to the release of data from the first year of LSST ($i_{\rm lim} \sim 25.5$ [85]), $\sim 15-50\%$ of the strongly-lensed transients are expected to be hostless, i.e. in lensed $z = 1-2$ galaxies beyond the sensitivity limit of precursor surveys such as DES DR1 ($i_{\rm lim} \sim 23.5$ [143]).

of LSST after one year of observing, with $f_{\rm hostless} \lesssim 0.1$. However, this is little comfort for efforts to detect strongly lensed transients within the first year or two of LSST observations, because cluster watch-lists for these early years of LSST will be constructed from pre-LSST data. It is also important to stress that our estimates of $f_{\rm hostless}$ are lower limits, because they assume that all strongly-lensed galaxies brighter than $i_{\rm lim}$ are detectable – i.e. source-plane lens detection methods are perfect.

In summary, our estimates of $f_{\rm hostless}$ motivate consideration of lens-plane search methods for finding strong lensing clusters, as they suggest current watch-lists built from purely source-plane search methods may not contain all of the clusters responsible for lensing a non-negligible number of hostless transients.

2.4 Strong-lensing clusters in magnitude limited surveys

To answer the second question posed in the introduction, we develop a model to estimate the fraction of strong lensing clusters that will be unidentifiable as lenses in magnitude-limited searches for multiply-imaged galaxies or bright arcs. In other words, we estimate the fraction of clusters that would require lens-plane methods to identify, assuming we cannot increase the sensitivity of source-plane searches.

The model utilises Poisson statistics to determine the probability of finding no detectable strongly lensed galaxies behind a cluster lens, based on galaxy number densities from the COSMOS survey. The absence of any detectable galaxies within a lens' so-called strong lensing cross-section implies that no observable bright arcs or multiple images will be seen, and so would not be identifiable as a strong lens in a magnitude-limited source-plane

search. Our estimates of the fraction of unidentifiable strong-lensing clusters are lower limits for the same reason as discussed in section 2.3, i.e. that any inefficiency of methods used to search for multiply-imaged galaxies will act to boost the fraction of strong lensing clusters that are missed.

2.4.1 Statistical model

We estimate f_0, the fraction of unidentifiable strong lensing clusters of mass M_{200}, from the probability that the number of strongly-lensed galaxies behind a cluster that are brighter than the photometric depth of the survey, $m_{\rm limit}$, is zero. The first step of this calculation is to consider Poisson statistics, where the probability of k galaxies appearing in a region of size σ with average galaxy number density N is given by:

$$p(k|N,\sigma) = p(k|M_{200}, m_{\rm limit}) = \frac{(N\sigma)^k \exp(-N\sigma)}{k!}. \tag{2.2}$$

Here we have replaced the independent variables on the left hand side as the strong lensing cross section σ of the cluster is a function of M_{200}, whilst $m_{\rm limit}$ affects the number density of observable galaxies that could be lensed by the cluster (see subsection 2.4.2 and subsection 2.4.3). For the cluster to be unidentified as a lens, no observable galaxies must be inside the strong lensing region behind the cluster – so by setting k=0 the equation reduces to:

$$p(0|M_{200}, m_{\rm limit}) = \exp(-N\sigma). \tag{2.3}$$

Since both σ and N are functions of redshift, we must take this into account when calculating the probability. Our estimates of observable galaxy number density are calculated in discrete redshift bins (see subsection 2.4.3), and so we need to determine the probability that no galaxies reside within the strong lensing region at the redshift associated with each bin. Therefore, the total fraction f_0 is given by the probability of having zero galaxies within the strong lensing region at all redshifts considered, i.e. it is the product of the individual

probabilities calculated for each redshift bin:

$$f_0(M_{200}, m_{\rm limit}) = \prod_i p_i(0|M_{200}, m_{\rm limit}) = \exp\left(-\sum_i N_i\,\sigma_i\right). \tag{2.4}$$

Here we use the index i to run over the series of redshift bins, and have simplified using Equation 2.3. These equations assume that galaxies are randomly distributed on the sky, and therefore ignore galaxy clustering. Clustering concentrates some of the galaxy population into particular regions of space near to each other, meaning a randomly-positioned aperture of fixed size will find zero galaxies within it more frequently than using the above Poisson-based calculations. Using Equation 2.4 will therefore result in a conservative lower limit on f_0.

2.4.2 Strong lensing cross-section

Our model for the strong lensing cross-section, σ, of a lens relies on an analytic description of the typical mass distribution in galaxy clusters on the scale of the Einstein radius – i.e. a few tens of arcseconds. The singular isothermal sphere (SIS) model is commonly used to quantify the density profile in studies that predict the lensing properties of massive galaxies [e.g. 144]. This model has a projected density profile of:

$$\Sigma(R) = \frac{\sigma_v^2}{2GR}, \tag{2.5}$$

where G is the gravitational constant, R is the projected radial distance from the centre of the lens and σ_v is the velocity dispersion. However, the projected density profile of clusters in the strong-lensing regime is typically shallower than the R^{-1} isothermal profile. For example, the slope of the projected density profile of strong-lensing clusters in the Local Cluster Substructure Survey (LoCuSS) sample span exponents in the range -0.11 to -0.87 at the respective Einstein radii of the clusters for sources at $z_S = 2$, with a median of -0.57 ([145]; see also Figure 3 of [146]).

A common alternative to the SIS model is the Navarro, Frenk and White (NFW, [147]) model. Whilst this model describes the observed density profile of clusters well on large scales [e.g. 148], it is too shallow within the Einstein radius of clusters. For example, the NFW models described in [148] that fit the weak-lensing constraints on the clusters in the [145] strong-lensing sample have exponents in the range -0.22 to -0.41 at the respective Einstein radii of the clusters for a source at $z_S = 2$. Therefore neither the SIS nor the NFW model alone provides a completely faithful description of the azimuthally averaged properties of strong-lensing clusters clusters at their Einstein radii – the SIS model is too steep and the NFW model is too shallow. We adopt the SIS model because its slightly steeper slope will boost the strong-lensing cross section relative to reality and thus ensure that our end values of f_0 (Equation 2.4) are conservative. After describing our definition of cross section below, we will return to this point at the end of this Section.

For simplicity, we consider a galaxy to be strongly lensed if it experiences a gravitational magnification of $|\mu| \geq 10$. We also assume that all strongly lensed galaxies suffer the same magnification $|\mu| = 10$ – the smallest value we associate with strong lensing – and ignore the effect of larger magnifications. This is justified, as the quantity of strong lensing regions with the capability to produce a magnification greater than some value $|\mu|$ falls off as μ^{-2} [149], and so the population of strong lensing lines of sight is dominated by those of lower magnification. Defining strong lensing in this way allows us to quantify the strong lensing cross-section by finding the region within which the magnification exceeds a particular value of $|\mu|$. Following the equations describing the SIS model in e.g. [1], this condition is found to be satisfied by at least one image when the source is within the region:

$$\beta < \frac{\theta_{\mathrm{E}}}{|\mu| - 1}, \tag{2.6}$$

where β is the angular separation from the centre of the lens in the source plane and θ_{E} is the Einstein radius of the lens. Using Equation 2.6, the strong lensing cross-section can be found by taking advantage of the symmetry of the SIS model and using our $|\mu| = 10$

definition of strong lensing:

$$\sigma = \pi\beta^2 = \frac{\pi\theta_{\rm E}^2}{81}, \tag{2.7}$$

which depends only on the Einstein radius. Within the SIS model, the Einstein radius can be expressed in terms of the lens mass as:

$$\theta_E = \frac{2\pi}{c^2}\left(\frac{D_{\rm LS}}{D_{\rm S}}\right)(10\,G\,H_{\rm L}\,M_{200})^{\frac{2}{3}}, \tag{2.8}$$

where $H_{\rm L}$ is the Hubble parameter at the lens redshift, and $D_{\rm LS}$ and $D_{\rm S}$ are the angular diameter distances between the lens and the source, and the observer and the source respectively. M_{200} is defined as the mass within a radius r_{200}, within which the mean density of the cluster is 200 times the critical density of the universe. We adopt a single lens plane at a redshift of $z_{\rm L} = 0.25$, which fits with the binning procedure used in subsection 2.4.3, and is close to the median value from the sample of known strong lensing clusters discussed by [122]. Following these specifications, the strong lensing cross-section within each redshift bin can be determined as a function of halo mass.

The range of density profile slopes for known strong-lensing clusters noted above implies considerable scatter in their cross-sections. This could be due to a variety of phenomena such as substructures within cluster cores that are associated with cluster-cluster and cluster-group mergers [e.g. 150, 151, 152, 153], cluster halo triaxiality [e.g. 154, 155, 156, 157], or line-of-sight structure [158, 159, 160]. We investigate this scatter further in the context of our definition of the lensing cross-section, in part as a cross-check on our assertion that adopting the SIS model is conservative. We consider the fourteen X-ray selected clusters in common between the [145] strong-lensing analysis and [148] weak-lensing analysis. We used the models of Richard et al. to compute the total source-plane solid angle that is magnified by $|\mu| \geq 10$, and compared these values with the equivalent SIS cross-sections that are calculated using Equation 6 and M_{200} for each cluster from Okabe and Smith. The distribution of the ratio of SIS to LoCuSS cross-section is approximately log-normal and is

centred at $\ln(\sigma_{\rm SIS}/\sigma_{\rm LoCuSS}) = 0.23$, implying that the SIS model typically over-estimates the lens cross-sections by 26% – i.e. in qualitative agreement with our expectations. The standard deviation of the distribution implies a factor of ~ 3.7 scatter around the central value of 0.23, which reflects the structural diversity of strong-lensing cluster cores. Therefore, when discussing cluster mass in later Sections, it should be taken to mean "clusters that have cross-sections comparable with the typical cluster of that mass". The scatter therefore raises important questions about how to approach the lens-plane selection of strong lensing clusters, and does not alter the broad conclusions of this chapter. We will investigate methods to lens-plane select strong lensing clusters in future work.

A final consideration to be made is of the finite size of galaxies in the source plane. The typical solid angles of optically-selected galaxies from [161] was compared to the SIS cross-section, and it was found that typical $z = 2$ galaxies subtend a solid angle comparable to the SIS cross-section of an $M_{200} = 5 \times 10^{13}{\rm M}_{\odot}$ cluster. Therefore less massive clusters do not strongly lens a region large enough to enclose an entire typical galaxy. Because of the galaxy number densities (subsection 2.4.3), this caveat does not turn out to affect the conclusions of this study. This is because the fraction of clusters that lens one or more galaxies does not become significant until at least $M_{200} \sim 10^{14}{\rm M}_{\odot}$ (depending on observation depth, see subsection 2.4.4), at which point the cross-section is much larger.

2.4.3 Galaxy number density

Galaxy number densities, N_i, were estimated using number counts from the COSMOS catalogue of [142]. Galaxies are binned so that the observable number density can be quantified as a function of redshift. The catalogue was split up into eleven redshift bins in the range $0.25 < z < 5.75$, each with a constant width of 0.5. This scheme was chosen because it spans the majority of the catalogue (which includes objects up to redshift $z = 6$) and al-

lowed for the lens to reside at a redshift $z_{\rm L} = 0.25$, a value consistent with the current known population of strong lensing clusters [122]. Ultimately, the final three bins centred at $z = 4.5$, 5.0 and 5.5 were excluded from the analysis as they contained very few galaxies with well-constrained redshifts.

The photometric depth of the catalogue from Ilbert et al., $i = 25$, is well matched to the first data release (DR1) of DES, which reaches approximately this magnitude after taking into account a lens magnification of $|\mu| = 10$. However, data from the final release of DES, and other surveys including upcoming data from LSST will reach depths up to $i \sim 28$ after including this magnification, and hence will probe intrinsically fainter galaxies beyond those of the COSMOS catalogue. Therefore, we fit a Schechter function [141] to the number counts in each redshift bin, allowing the COSMOS number counts to be extrapolated when considering deeper surveys.

The dominant source of uncertainty in this extrapolation is the so-called "catastrophic failure" rate of the photometric redshifts. The catastrophic failure rate quantifies how often photometric redshift measurements differ significantly from reliable spectroscopic redshift measurements, as defined in [142]. If the rate is high, then many galaxies will be placed in the wrong redshift bins, skewing the number densities and hence affecting the curve fitting and extrapolation. The failure rates provided in the catalogue paper [142] vary with apparent magnitude, but are of order 15 to 20% for the faintest sources (which Ilbert et al. categorise as $i > 23$). We quantify the overall effect of catastrophic failures on the end result by considering a worst-case scenario based on the quoted failure rates, and in this scenario determine how many galaxies would appear in the wrong redshift bins. Then, correct for this and re-do the calculation based on the new "corrected" number counts. The true probability curve will then lie somewhere between the original and corrected result, providing a range of uncertainty on the final result. Doing so provides an error on the final result of $< 2\%$.

2.4.4 Predictions of the model

Figure 2.2 shows our estimated lower limit on the fraction of strong-lensing clusters that will be unidentifiable by wide-field surveys as a function of the lens halo mass and survey magnitude depth, as calculated by the model described in section 2.4. The fractions are calculated for various survey depths that span ongoing and upcoming surveys. The uncertainties in each curve, represented by their width, are due to limitations of the photometric redshifts in the COSMOS data set, as outlined in subsection 2.4.3. This plot shows that for the most massive strong lensing galaxy clusters, with masses of $\sim 10^{15}\mathrm{M}_{\odot}$, about 75% would not be identifiable as strong lenses by a survey similar to DES DR1, i.e. $i_{\mathrm{lim}} \sim 23.5$ [143]. In deeper surveys, such as the first year of LSST observations ($i \sim 25.5$), only around 40% of $10^{15}\mathrm{M}_{\odot}$ will not be identifiable as strong lenses. Lenses of lower mass are even less likely to be identified. The model predicts that even with deeper surveys, no more than 5% of the more common $10^{14}\mathrm{M}_{\odot}$ strong lensing capable clusters will be identifiable by searching for multiply imaged galaxies or bright arcs. We therefore conclude that the level of incompleteness of source-plane searches will be particularly severe for strong lensing clusters with typical masses close to the knee of the halo mass function, independent of whether deep future LSST survey data are available.

2.5 Summary and Implications for Strongly-lensed Transients

Observational results [132, 133, 102, 134, 162, 163] and theoretical predictions [164, 81] all point to galaxy clusters making a significant contribution to the high-magnification strong lensing optical depth of point sources. This implies that some of the strongly-lensed transients discoverable by ongoing and future optical surveys (e.g. ZTF, GOTO, LSST) will

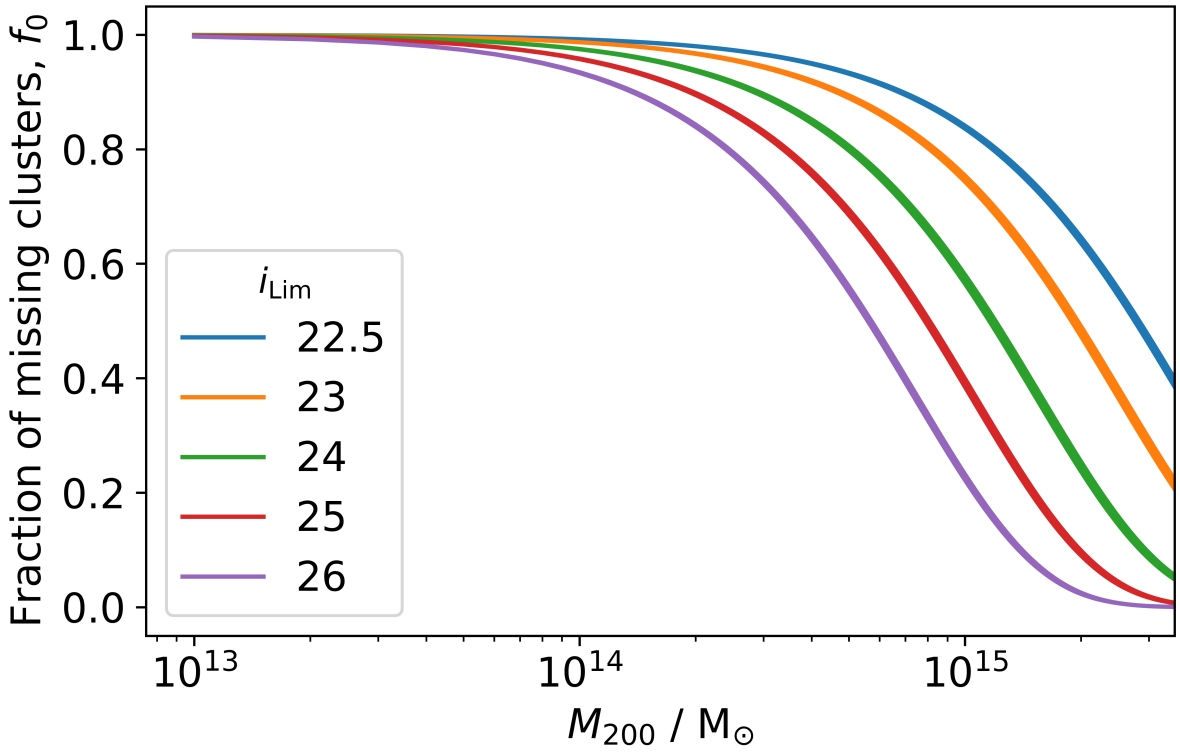

Figure 2.2: The fraction of strong lensing clusters that are unidentifiable as strong lenses in magnitude-limited surveys, as a function of halo mass, M_{200}, and survey depth, i_{lim}. The coloured lines represent various magnitude depths similar to those of recent and upcoming surveys. The thickness of each line corresponds to the uncertainty due to photometric redshift failures. DES-like surveys will miss $\sim 75\%$ of $10^{15}\mathrm{M}_\odot$ strong-lensing clusters, rising to $\sim 100\%$ at $\sim 10^{14}\mathrm{M}_\odot$. Deeper surveys such as LSST will miss ~ 40 and $\sim 95\%$ at these masses.

be strongly-lensed by galaxy clusters. So far, searches for transients strongly-lensed (i.e. multiply-imaged) by clusters have employed pointed observations of known strong-lensing clusters – i.e. clusters that are known to be strong lenses because multiply-imaged galaxies have been detected in their central regions [e.g. 115, 102, 119, 123], or in other words, clusters selected in the source plane. In this study we have investigated whether it is beneficial to build a watch-list of strong-lensing clusters for wide-field optical surveys such as LSST, based on only known strong lenses (selected in the source plane) or on a more extensive (likely more complete but less pure) list of strong-lensing capable clusters which includes those selected in the lens plane.

First, in section 2.3 and Figure 2.1, we derived a lower limit on the fraction of lensed transients whose host galaxies are fainter than the magnitude limit of wide-field photometric surveys, even after taking lens magnification into account. Such lensed transient point sources would appear to be hostless and would be lensed by clusters that are not identifiable as strong lenses by a source-plane search. We predict that the fraction of hostless lensed transients is $f_{\rm hostless} \sim 0.15 - 0.5$ for cluster watch-lists that are based on source-plane selection in data of depth similar to DES DR1. This falls to $f_{\rm hostless} \lesssim 0.1$ for source-plane-based watch-lists derived from LSST year one data. Our estimates of $f_{\rm hostless}$ therefore imply that galaxy clusters that are not identifiable as strong lenses in magnitude limited surveys should be included in watch-lists so that the non-negligible number of lensed hostless transients can be identified, especially if the watch-list is based on relatively shallow data before the LSST survey begins.

Second, in section 2.4 and Figure 2.2, we predict the fraction of strong lensing capable clusters that are unidentifiable due to an absence of detectable multiply-imaged galaxies. We predict that the fraction of unidentifiable cluster lenses of mass $M_{200} \sim 10^{15}{\rm M}_{\odot}$ is $f_0 \sim 0.75$ at depths comparable to DES DR1, and $f_0 \sim 0.4$ at depths comparable to the first year of LSST observations. For more abundant $10^{14}{\rm M}_{\odot}$ clusters, we predict that

even at LSST one-year depth, the fraction of unidentifiable strong lensing clusters is $f_0 \gtrsim 0.95$. We emphasize that these predictions are conservative lower limits as we assume no galaxy clustering and a perfectly efficient source-plane cluster strong-lens search algorithm. Taken together, our results on $f_{\rm hostless}$ and f_0 both motivate building cluster watch-lists for strong-lensing transient discovery based on lens-plane selection. In chapter 3 we will explore methods for lens-plane selection.

Chapter 3

Paper 2

3.1 Preamble

This chapter is a reformatted and partially edited version of my first-author paper [165]: Ryczanowski D., Smith G. P., Bianconi M., McGee S., Robertson A., Massey R., Jauzac M., *Enabling discovery of gravitationally lensed explosive transients: a new method to build an all-sky watch-list of groups and clusters of galaxies*, 2022, submitted to MNRAS, arXiv:2204.12984. This chapter is adapted from the second version (v2 on arXiv) of this publication, with updated plots and inclusion of some of the corrections suggested by the MNRAS reviewer.

The study was initially conceived as a natural continuation from the results of chapter 2 [124] by myself and Dr. Graham P. Smith. I was responsible for completing all of the analysis and producing all of the figures, with the pedagogical support of both Dr. Graham P. Smith and Dr. Matteo Bianconi. The other co-authors provided comments on drafts of the figures and text of the paper.

3.2 Introduction

Within the next decade, lensed transient detections are expected to increase vastly in number thanks to deep wide-field surveys such as Rubin's LSST [85, 127, 87, 166], and expand to other flavours of transient, including gravitational waves and their kilonova counterparts [88, 12], as well as gamma ray bursts [120]. One observing strategy for finding lensed transients follows a watchlist-based approach, whereby wide-field survey telescopes routinely scan the sky for transient events and compare their locations with a list of lens coordinates. Those sufficiently nearby a lens are then flagged for further investigation and follow-up observations. This technique works to filter out candidate lensed transients from the increasingly large number of events detected nightly by wide-field surveys like those conducted currently by the Zwicky Transient Facility [ZTF, 84], and that will soon commence with Rubin's LSST. In addition, this method allows lensed transients to be identified even if they have multiple images arriving on timescales shorter than the discovery survey's cadence, or if multiply imaged transients have only one detectable image due to variances in magnification. This is advantageous as lensed transients with these properties would evade detection by a search that instead looks for multiple images by way of detecting spatially coincident transient events within a wide-field survey that are separated by some time delay.

One important requirement of a lens watchlist is that it contains objects across the entire sky. This is because many transients are now being discovered by facilities that are able to monitor the entire sky, including gravitational wave interferometers and gamma ray burst satellites. This is in addition to the optical surveys that have been, and will continue to monitor a significant fraction of the sky like ZTF and Rubin's LSST. Therefore, current catalogues of lenses that only reside in the footprints of particular surveys are insufficient for maximising lensed transient discoveries. In other words, a significant fraction of the mass function covering the range $10^{12} \lesssim M_{200} \lesssim 10^{15}\,\mathrm{M}_{\odot}$ [81] is missing from the tools

used to find lensed transients due to the lack of an all-sky lens catalogue. This is especially important in the southern hemisphere, which Rubin will begin to survey in the next few years to unprecedented depths. Ensuring such a list of lenses is available as soon as Rubin's operations begin is ideal so that searches for lensed transients can be optimised immediately – maximising early science prospects and the baseline over which these discoveries can be made.

It is also important to emphasise that the dark matter halos that are efficient lenses for the population of transients in question do not have to have been previously identified as lenses (for example, by identification of arcs or multiple images) to be considered a valid entry in a watchlist. This is because, in general, the detectability of lensed transients is independent of whether or not the lensed galaxies that host them can be detected in magnitude-limited surveys – even optical transients such as SNe can easily be brighter than their host galaxy, so host detection does not always come in tandem. Therefore, the selection of objects for a complete strongly-lensed transient watchlist should not just consist of known lenses, but in fact any object capable of lensing. In other words, lenses should be selected in the lens-plane (i.e. based on their lensing ability), rather than in the source-plane (i.e. based on a chance alignment with source-plane objects detected in magnitude-limited searches for arcs). As shown in [124], for the case of group and cluster scale objects, $\sim 95\%$ of $10^{14}\mathrm{M}_{\odot}$ clusters and $\sim 40\%$ of $10^{15}\mathrm{M}_{\odot}$ clusters would not be identified as lenses based on source-plane selection at the sensitivity of Rubin, despite being capable lenses of transients. Therefore, even with next-generation surveys, source-plane lens selection methods will miss a significant fraction of the objects capable of lensing transients. Alternative lens-plane selection methods have been explored previously for both massive galaxies and clusters [e.g. 138, 139], however a suitable all-sky catalogue of these objects for the detection of lensed transients in wide-field surveys does not yet exist.

Before discussing lens-plane selection methods further, it is first important to con-

sider what objects should populate the watchlist. Ray tracing through hydrodynamical simulations of large scale structure in the Universe indicates that the optical depth to high magnification ($|\mu| \geq 10$) spans a broad range of halo masses, with $\sim 50\%$ of it contributed by objects of group and cluster mass scales ($M_{200} \gtrsim 10^{13} M_{\odot}$, [81]). This is a key region of parameter space for lensed transients because clusters are responsible for the most extreme cases of magnification and image time delays (like those seen with lensed SNe Refsdal and Requiem), which are interesting from the perspectives of studying distant objects and making measurements of cosmological parameters with high precision. It is also relatively under-explored in relation to very wide-field time domain surveys, with search strategies for lensed supernovae concentrating on watchlists comprising individual galaxy lenses [e.g. 126].

Previous studies aiming to detect galaxy clusters have historically used a variety of methods. Direct detection is possible through detection of X-rays emitted by the hot intra-cluster gas [e.g. 167], or distortion of the cosmic microwave background by the same medium – known as the thermal Sunyaev-Zeldovich effect [168, 169]. Clusters can also be discovered through observations of galaxies by the detection of a cluster red sequence [e.g. 170], or by utilising galaxy positions and photometric redshifts to test for clustering in 3-dimensional space [e.g. 171]. More recently, cluster detection in future wide-field surveys was thoroughly tested using a variety of methods in preparation for the wide survey component that is to be conducted by *Euclid* [172]. These methods each presented their own merits and challenges, and overall sported great success. Inspired by these methods, we set out to develop our own that complements our requirements for an all-sky lens-plane selected cluster/group catalogue. The method of [173] was of particular interest due to its small number of fundamental requirements and capability to be used alongside existing all-sky survey data, aiming to utilise all-sky J-band data from the UKIRT Hemisphere Survey [UHS, 174] in the north and the VISTA Hemisphere Survey [VHS, 175] in the south, as well as $W1$-band data from the *WISE* (Wide-field Infrared Survey Explorer) mission [176].

Therefore, in this paper we describe and test a method with the capability to produce an all-sky watchlist of galaxy group and cluster-scale objects ($M \gtrsim 10^{13} M_{\odot}$) out to $z \sim 1$, with the intention of using the list to aid in the discovery of gravitationally lensed transients. Our method is based upon the principles of [173] and can detect clusters to sufficient depth using only existing all-sky near-infrared data. Our testing concentrates on the southern sky which is due to be surveyed by Rubin in the coming years. Prioritising this region allows a curated watchlist to be available to find lensed transients as soon as Rubin begins operations.

The structure of this paper is as follows: Section 3.3 gives an overview of the surveys and data used in this study. Section 3.4 describes the cluster-finding method, and Section 3.5 explains how the method was tested, using both real data and state-of-the-art simulated data, before summarising in Section 3.6. Where relevant, and unless otherwise stated, we have assumed a flat cosmology with $H_0 = 67.74$ km/s/Mpc, $\Omega_{\Lambda} = 0.693$ [140] and give magnitudes in the Vega system.

3.3 Surveys/Data

3.3.1 Overview of data used

The main data used in this study are from wide-field surveys conducted by the VISTA and *WISE* instruments. These surveys are used due to their complete coverage in the southern hemisphere – the region due to be surveyed by the Rubin Observatory once in operation – and also for their access to the wavebands sensitive to galaxies in cluster environments. Specifically, we make use of J-band photometry in the southern hermisphere from VISTA and all-sky *W1*-band photometry from *WISE* in order to create density maps of galaxies. It should be noted that suitable J-band data are also available for the northern hemisphere from

the UKIRT Hemisphere Survey (UHS), but we prioritise testing in the southern hemisphere due to slightly better magnitude depths and to cover the field of Rubin's LSST. Sources are first matched between the *WISE* and VISTA catalogues, giving multi-band coverage of each galaxy – this ensures all detections are robust, and allows estimates of further properties from $J - W1$ colours such as the redshift. The following sections describe the data sets in more detail.

3.3.2 VISTA Data

The Visible and Infrared Telescope for Astronomy (VISTA) is a 4.1m survey telescope located at Paranal Observatory, Chile. It has conducted a variety of wide-field surveys in the sky above the southern hemisphere and equator, and between these the entire southern sky has collectively been surveyed. In this work, we directly use data from the largest of these surveys: the VISTA Hemisphere Survey (VHS, $\sim$20000 deg^2, [175]) and the VISTA Kilo-Degree Infrared Galaxy Survey (VIKING, $\sim$1500 deg^2, [177]). These surveys provide complete coverage in two near-infrared bands, J and Ks, with additional coverage in other bands in specific regions. In creating our maps, we utilise the J-band (1.25μm) data which has a 5σ detection limit of $J(5\sigma) \leq 20.1$ across the surveys. All VISTA data used is publicly available through the online VISTA science archive.

3.3.3 *WISE* Data

The NASA *Wide-Field Survey Telescope Explorer* (*WISE*) is a space-based 0.4m infrared telescope that surveys the entire sky in four infrared bands, named $W1$ to $W4$ with wavelengths of 3.4, 4.6, 12 and 22 μm respectively. We use sources detected specifically in the $W1$-band – the most sensitive of the *WISE* passbands – from the CatWISE2020 catalogue

[178], a compilation of almost 2 billion sources collected by the instrument from its first operation in January 2010 up to December 2018.

The addition of the *WISE* data is useful for assuring robust galaxy detections by requiring each *WISE* source to match to a nearby J-band detection from VISTA, and creates the opportunity to use $J-W1$ colours to infer photometric redshift estimates and additional metrics to test if cluster detections are real objects (see subsection 3.5.3). Figure 3.1 shows the predicted evolution of an $L^\star$ galaxy's[1] $J-W1$ colour using the EzGal modelling tool [179] [2]. This shows that with the magnitude limits of each survey, detecting cluster galaxies down to at least $L^\star$ is attainable out to $z \sim 1$. When modelling the galaxy evolution, we assume a Bruzual & Charlot model [180], with a single delta burst of star formation at $z = 3$ that follows a Chabrier initial mass function [181] and contains stars of solar metallicity. We also normalise the luminosity of an $L^\star$ galaxy to the [182] cluster sample, which has $K_S^\star = 15.5$ at $z = 0.25$. $W1$ was chosen for this purpose over K-band, as $W1$ has full coverage in both hemispheres, and K-band in current surveys is not sensitive enough to reach $z = 1$.

One important consideration when utilising *WISE* data is the large PSF ($W1$-band FWHM ~ 6 arcsec) compared to the VISTA data (J-band FWHM ~ 1 arcsec). This means that in dense cluster cores, there is a possibility that multiple galaxies detected by VISTA are blended into a single *WISE* detection. To take account of this, when matching sources between the two catalogues, the number of VISTA sources within one PSF half-width of a *WISE* detection is counted and used to weight the contribution of that detection to the galaxy map. The existence of blended sources in dense cluster cores also make it difficult to determine accurate colours for these central galaxies and their neighbours. For example, within our sample of known strong lensing clusters described in subsection 3.5.1, approx-

[1] L* is a characteristic luminosity scale present in the [141] luminosity function, typically representing the value below which the number density grows exponentially.

[2] http://www.baryons.org/ezgal/

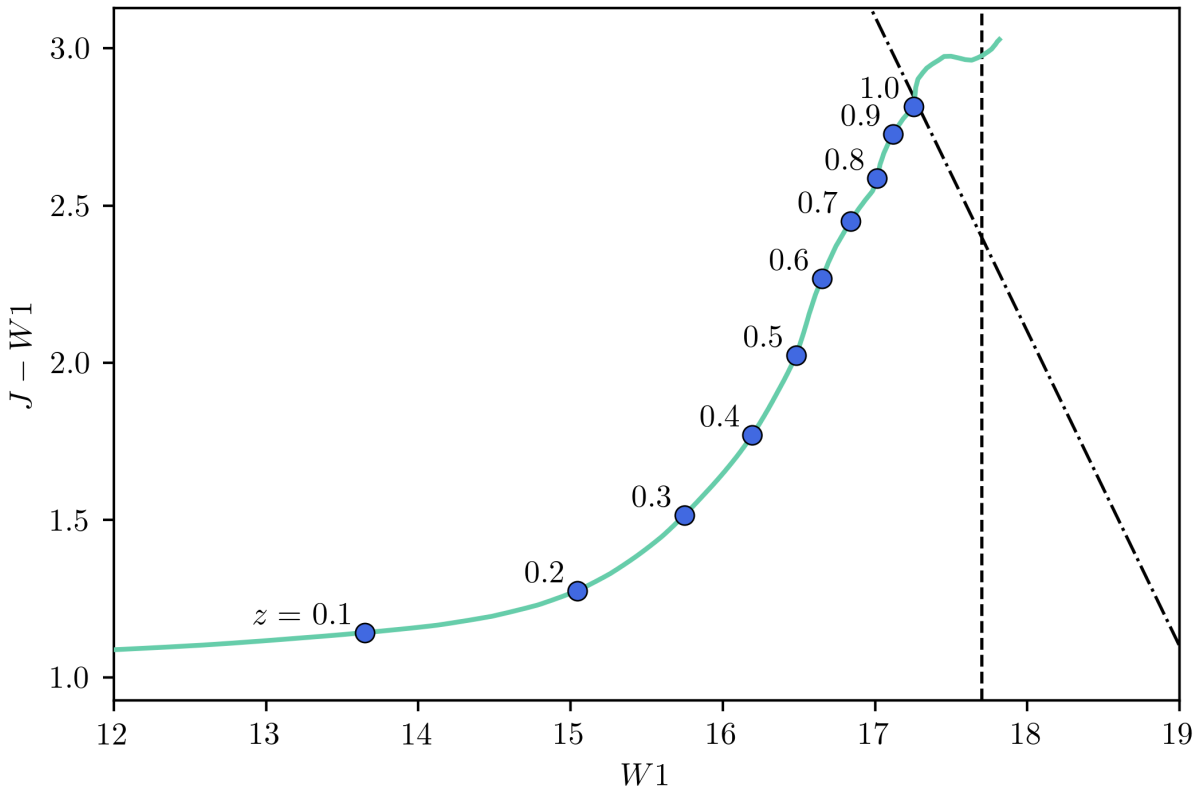

Figure 3.1: Predicted $J - W1$ colour evolution of an $L^\star$ cluster galaxy as a function of apparent $W1$ magnitude (solid line). Circular points highlight the values at specific redshifts during this evolution. The vertical black dashed line represents the 5σ $W1$-band magnitude limit of CatWISE ($W1 = 17.7$), and the dot-dashed diagonal line represents the 5σ J-band magnitude limit of VHS ($J = 20.1$), the largest of the VISTA surveys. Magnitudes obtained using the EzGal tool assuming a Bruzual & Charlot evolution, with an SSP star formation history, Chabrier initial mass function and solar metallicity. Given that $z = 1$ $L^\star$ cluster galaxies reside within these detection limits, detection of clusters out to this redshift is tractable.

imately 10% of *WISE* galaxies within 1 arcminute of their respective cluster centre have multiple matches in the J-band. However, as we do not make any explicit cuts based on the colours this does not directly affect the density maps, but does have a visible effect on colour-magnitude diagrams we produce during testing in subsection 3.5.3.

Our selection criteria for galaxies are relatively straightforward, and consist of a flat cut of the 5σ detection limit in the relevant bands in both surveys ($J = 20.1$ for VHS, the largest of the VISTA surveys and $W1 = 17.7$ for *WISE*) and a cut on the VISTA catalogue's *pGalaxy* attribute which estimates the probability that a source is a galaxy. We require $pGalaxy > 0.9$ to eliminate any interloper stars, although the majority of the sample has $pGalaxy > 0.99$, indicating these are secure detections of extended sources.

3.4 Method

3.4.1 Background

Galaxy cluster members are typically early-type galaxies that emit strongly in the near-infrared, due to the spectrum of metal-poor population II stars ($T \sim 3000$K) that dominate early type galaxies' peaks at a rest-frame wavelength of $\lambda \sim 1\mu$m. Utilising the $W1$-band of *WISE* and the J-band of VISTA, we produce density maps of galaxies detected in both catalogues. This is done following a similar methodology to [173], whereby a raw map of galaxy positions is convolved with a difference-of-Gaussians smoothing kernel. This convolved map then provides an estimate of the local density of galaxies within that region of sky, and peaks within the map can hence be used to unveil candidate galaxy groups and clusters within the wide-field data. Given that no specific colour or redshift information is taken into account when selecting galaxies, it is entirely possible that multiple chance alignments of smaller groups can produce signals in the maps comparable to those from richer clusters. Whilst it might initially appear that these false positives are problematic, such cases are still considered to be high-density lines of sight and are therefore still valuable from a strong lensing perspective, and hence belong in a lensed transient watchlist. Therefore, we can motivate using this method to assemble a list of the densest regions of the sky as traced by collections of galaxies detected in infrared data.

3.4.2 Creating density maps with kernel convolution

To create a raw density map, galaxies matched between the two catalogues that pass the selection criteria are placed into a 0.5×0.5 degree pixel grid with 7.5 arcsec/pix scale. Each pixel contains a value representing how many galaxies exist within that region of space, and

we take into account the large PSF of *WISE* by weighting the contribution of a single *WISE* detection by the number of J-band detections from VISTA within the *WISE* PSF radius. This ensures we are not underestimating the number density due to blended sources in dense cluster cores where there can be up to of order 10 blended galaxies.

Once the raw map has been constructed, it is convolved with a kernel designed to smooth out contributions from components that do not match those of typical cluster core scales. The kernel is described by a difference of two normalised Gaussian functions with different widths given by:

$$K(\theta) = \frac{1}{2\pi\sigma_{\rm in}^2\sigma_{\rm out}^2}\left[\sigma_{\rm out}^2 \exp\left(\frac{-\theta^2}{2\sigma_{\rm in}^2}\right) - \sigma_{\rm in}^2 \exp\left(\frac{-\theta^2}{2\sigma_{\rm out}^2}\right)\right], \tag{3.1}$$

where θ is the angular separation and $\sigma_{\rm in}$, $\sigma_{\rm out}$ are the widths of the inner and outer Gaussians, respectively. By definition, $\sigma_{\rm in} < \sigma_{\rm out}$. Each Gaussian is normalised to have unit volume, such that the kernel integrates to zero. Similarly to [173], we select $\sigma_{\rm in} = 45$ arcsec, corresponding to the scale of the dense cores of galaxy clusters, and choose the ratio of $\sigma_{\rm in}$ to $\sigma_{\rm out}$ to be 1:6. Multiple values were experimented with for the filter widths, anticipating an effect based on the changing scales of clusters at different redshifts – however the final results were insensitive to any change of these parameters. Figure 3.2 shows an example of a difference-of-Gaussians function as given by Equation 3.1.

Applying the convolution produces a map whose pixels correspond to the local galaxy number density; Figure 3.3 shows an example map centred on known galaxy cluster and strong lens Abell 1689.

3.4.3 Estimating overdensity significance

Within each density map, a peak-finding algorithm is utilised to identify positions of the densest regions of the map. To reduce the impact of edge effects caused by the convolution

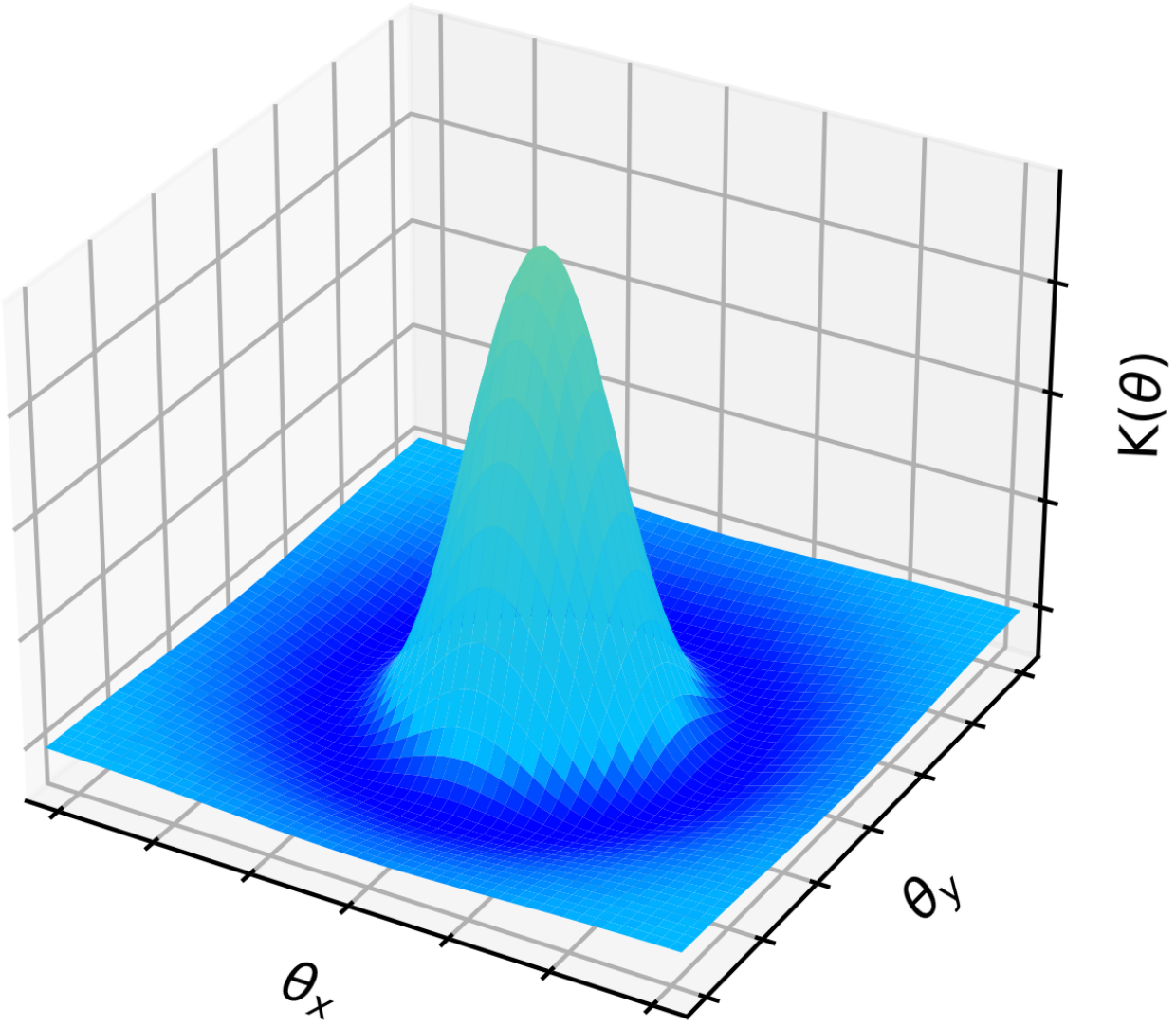

Figure 3.2: Example surface plot of a normalised difference-of-Gaussians kernel, showing the positive central peak and the negative region surrounding it. This is used as a smoothing function to identify cluster-like structures within pixellated galaxy maps. The angular extent of the interior width is tuned to that of cluster cores, and acts to smooth out contributions from scales larger and smaller than this.

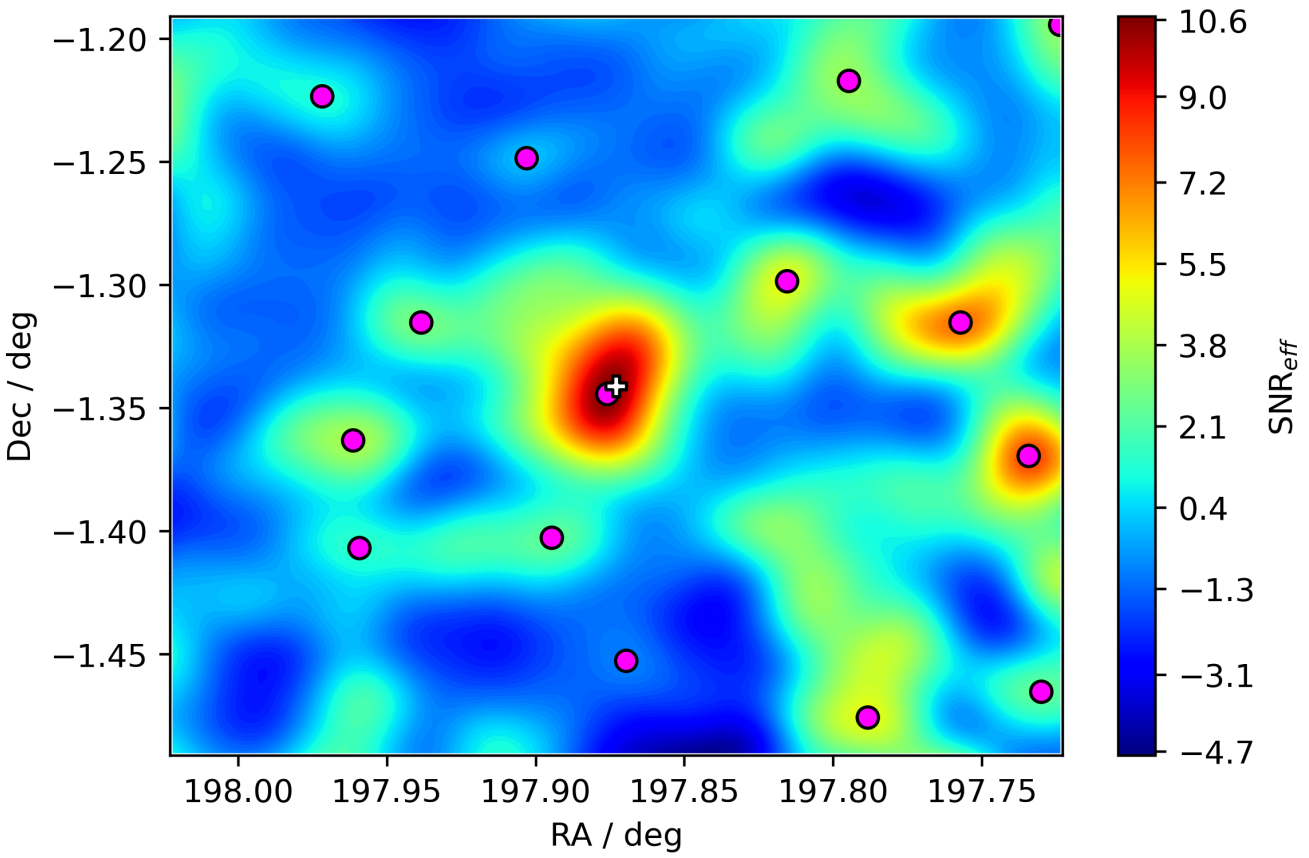

Figure 3.3: A 0.3×0.3 degree map produced by convolving a difference-of-Gaussians kernel with a pixel grid of galaxy positions surrounding the coordinates of known cluster and strong lens Abell 1689. Purple dots highlight peaks in the galaxy number density distribution, and the white plus marks the coordinates of the cluster centre, which in this case is located very close to the largest peak. The colour bar scale shows the $\mathrm{SNR}_{\mathrm{eff}}$ of each pixel, a quantity introduced in subsection 3.4.3 which indicates the significance of a detection, and is normalised between the maximum and minimum values within the map. Data to produce this map are taken from an overlapping 0.5×0.5 degree region, extending an additional 0.1 degrees from each edge of the map. This is to ensure there is sufficient data beyond the map region to prevent any edge effects caused by the convolution. The cluster in the centre is recovered with high significance, and a few other regions are highlighted as having a high density along the line of sight and hence represent candidate groups/clusters.

on outer regions of a map, we ignore any peaks that are within 24 pixels of the map border. This effectively reduces the size of each map to 0.3×0.3 deg, but ensures that no bias is introduced to outer regions. The reduced size of map is a fairly arbitrary choice and is specific for tests on known objects. This would be optimised for computational efficiency in a blind search, by maximising the usable map area given the inherent edge effects, but we leave investigation of this for future work.

We quantify the significance of each overdensity in a map by adopting a quantity similar in form to a signal-to-noise ratio (SNR), which we call the "effective SNR", $\mathrm{SNR}_{\mathrm{eff}}$, and calculating this for each pixel in the convolved map. We then take the largest $\mathrm{SNR}_{\mathrm{eff}}$ pixel value of each local maximum to represent the significance of a detection at that position. To calculate this quantity, we firstly assume that the background of non-clustered galaxies is randomly and uniformly distributed. Under this assumption, we can produce a large set of maps of randomly-distributed galaxies, where each map contains the same total number of galaxies as the real map now randomly positioned across the same size patch of sky. These random maps are then convolved by the same difference-of-Gaussians kernel, and can be used as a metric to estimate the background noise. By calculating the mean and standard deviation of pixels within these random maps, we define $\mathrm{SNR}_{\mathrm{eff}}$ for each pixel within real maps as:

$$\mathrm{SNR}_{\mathrm{eff}} = \frac{s - \mu}{\sigma} = \frac{s}{\sigma}, \tag{3.2}$$

where s is a pixel value, and μ and σ are the pixel mean and standard deviations respectively, determined from the sample of random maps. By construction, any pixel map convolved with a kernel of the form given by Equation 3.1 will have $\mu = 0$, due to the kernel's property of integrating to zero, hence the additional simplification in the equation and thus leaving only σ to be determined. In a random map containing N_{gal} galaxies, the pixel values follow a Poisson distribution and so $\sigma \propto \sqrt{N_{\mathrm{gal}}}$. Given that the smoothing kernel acts only to spread the pixel values from a raw map over a larger region, one can expect the standard deviation

of pixel values within the entire convolved map to follow the same distribution. Therefore, we can precisely measure the standard deviation σ' for a single arbitrary number of galaxies $N'_{\rm gal}$ and calculate $\mathrm{SNR_{eff}}$ in proportion for the relevant $N_{\rm gal}$:

$$\mathrm{SNR_{eff}} = \frac{s}{\sigma'}\sqrt{\frac{N'_{\rm gal}}{N_{\rm gal}}}. \tag{3.3}$$

Consequently, random maps only need to be created once, with new random maps being required only if a fundamental property of the method, such as the kernel size, is changed. By creating 10^4 random maps each containing $N'_{\rm gal} = 2000$ galaxies, we determine $\sigma' = (8.7 \pm 0.4) \times 10^{-3}$ galaxies/pixel. These values are then used to determine $\mathrm{SNR_{eff}}$ within the pixels of the real maps, which is in turn used to assess the confidence that a given local maximum within a map corresponds to a real group or cluster-scale object, and comparatively rank any peak determined by this method by way of proxy for the mass or richness of the cluster core. We discuss in section 3.5 the values of $\mathrm{SNR_{eff}}$ that categorise the robustness of detections. It should be stressed that $\mathrm{SNR_{eff}}$ is not a true signal-to-noise ratio, but rather an estimator based on correlated nearby pixels that aims to evaluate the overdensity of a region of galaxies under simple assumptions.

Given that the non-clustered background galaxy distribution will not be truly random but rather correlated on small scales to, on average, be denser than random, $\mathrm{SNR_{eff}}$ will be a slight underestimate due to underestimating the magnitude of the noise. However, we believe this effect to be small due to the amplitude of the galaxy two-point correlation function at scales similar to those of our maps. Figure 15 in [183] shows a determination of this quantity – their faint population of galaxies is approximately representative of the typical L* cluster galaxies we expect to be detectable with *WISE*, based on colours inferred from the same EzGal models introduced in subsection 3.3.3. Based on their results, galaxies at scales similar to our maps ($\sim$0.1 deg) are $\sim$5% denser than a purely random distribution. Therefore, we expect the difference made due to our simplifying assumptions to be small. In

addition, the ordering of objects based on $\mathrm{SNR}_{\mathrm{eff}}$ is arguably more useful than $\mathrm{SNR}_{\mathrm{eff}}$ alone, and this would largely remain unchanged as a result of this assumption.

3.5 Testing the method

3.5.1 Known cluster/group-scale lens test sample

We use two samples of lenses to test our method's ability to recover known groups and clusters – 130 spectroscopically confirmed cluster-scale lenses assembled by [122], and 98 galaxy and group-scale lenses assembled by [184]. The cluster-scale lenses have been utilised in previous searches for lensed gravitational waves and supernovae with a prototype watchlist [185, 186, 187]. These 130 objects are some of the best studied strong lenses in the literature, many of which have been observed by the *Hubble Space Telescope*. This sample ensures our test sample extends to the most extreme clusters in terms of mass, which have Einstein radii as large as 1 arcminute, and hence provide some of the largest strong lensing cross-sections for individual objects. The distribution of these clusters peaks at $z \sim 0.35$, but the upper tail stretches to $z \sim 1$, which suitably matches the distributions of objects we aim to detect, as outlined in section 3.2.

Objects from the [184] sample are lenses and lens candidates that were found within the Canada–France–Hawaii Telescope Lensing Survey (CFHTLenS) data. CFHTLenS is a deep optical ($u^*/g'/r'/i'/z'$-band) survey spanning 154 deg^2 observed by the Canada-France-Hawaii Telescope (CFHT) as part of the Canada–France–Hawaii Telescope Legacy Survey (CFHTLS). The survey's primary objectives involve studies of weak lensing effects, however the high-quality data along with accurate photometric redshifts makes it useful for some strong-lensing science as well. These group and galaxy scale objects typically have smaller

Einstein radii than those in the cluster sample, ranging from $3'' \leq \theta_E \leq 18''$, which is valuable for testing the limits of what the method can reliably detect. The redshift range of $0.2 < z < 0.9$ is also well-matched to our aims and the cluster sample.

We were able to retrieve VISTA data for 63 out of the 98 objects within the Carrasco et al. sample. The majority of the objects that do not have VISTA data reside in the third CFHTLenS region around $\delta = 55\,\mathrm{deg}$ – far outside of the coverage of the surveys. We were also only able to obtain data for 62 out of the 130 sample of known lenses, giving a total of 125 objects in our final test sample. Ultimately, the only information we utilise in our method beyond selection is the coordinates of objects from the samples and use them to obtain VISTA and *WISE* data from the surrounding regions. This allows us to test our method fully, extract the $\mathrm{SNR_{eff}}$ distribution for regions containing known objects and hence estimate the recovery rate of the method.

3.5.2 Results of the known lens test

For each of our sample objects, we produce a convolved density map using the difference-of-Gaussians kernel and the procedure as described in subsection 3.4.2. Within each map, we locate peaks within $5\sigma_{\mathrm{in}}$ (225 arcsec) of the object's coordinates given in the sample and calculate $\mathrm{SNR_{eff}}$ for each of these peaks using the same method discussed in subsection 3.4.3. If the $\mathrm{SNR_{eff}}$ around the peak closest to the object is above some designated threshold (which we initially define to be 5), then the object is considered to be recovered with high significance.

Figure 3.4 shows a plot of the calculated $\mathrm{SNR_{eff}}$ against estimated Einstein radius, θ_E, for our 125 sample objects. It should be noted that the θ_E values for objects in the Carrasco et al. [184] sample are taken directly from their catalogue and are only estimates

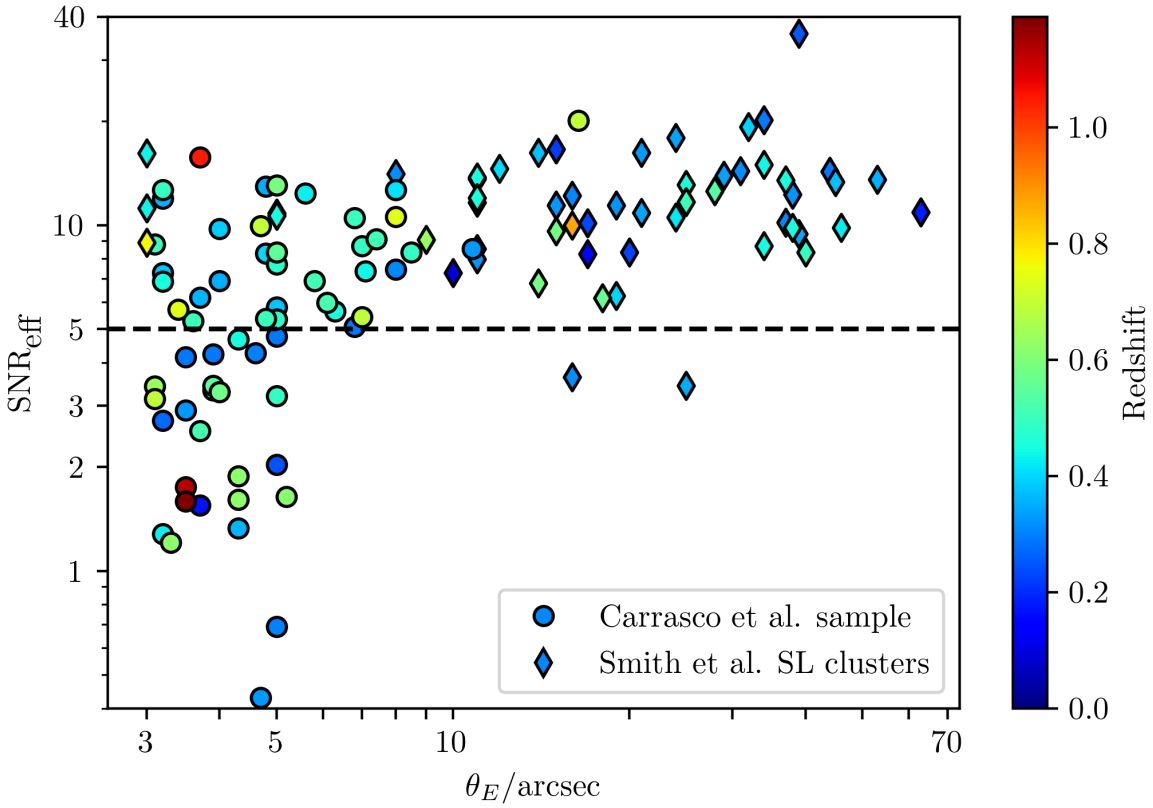

Figure 3.4: Distribution of $\mathrm{SNR_{eff}}$ against Einstein radius for the 125 test objects, made up of those from the Carrasco et al. sample (circles) and the Smith et al. SL sample (diamonds). Horizontal dashed line at $\mathrm{SNR_{eff}}$=5 marks the threshold above which an object is classed as recovered with high significance. The colour of the points represents the redshift of the object, signified by the colour bar. Recovery appears to be related to Einstein radius, as the majority of non-recovered objects have small θ_E ($\theta_E \lesssim 5''$). Recovery also does not appear to depend strongly on redshift, as shown by the absence of any obvious trends with redshift.

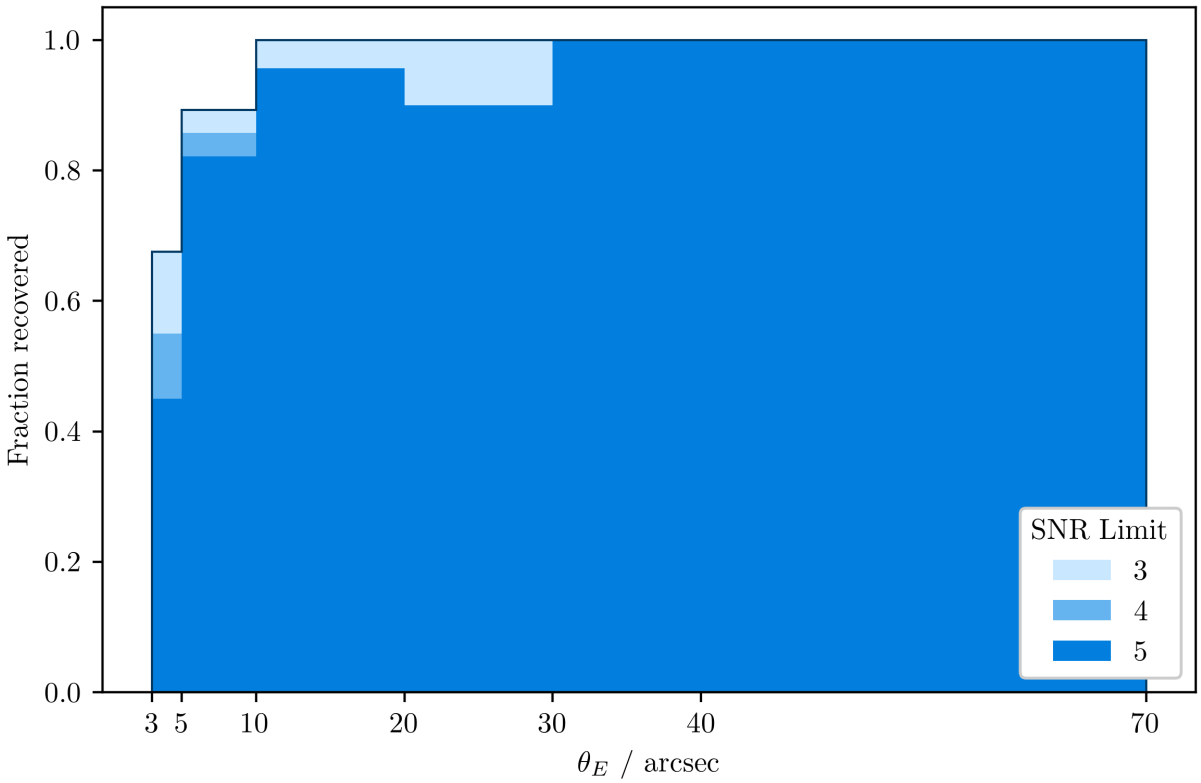

Figure 3.5: Histogram showing the recovery fraction of objects in bins of Einstein radius. Different colour bars represent different $\mathrm{SNR}_{\mathrm{eff}}$ thresholds to define recovery. Even with the stringent requirement of $\mathrm{SNR}_{\mathrm{eff}} > 5$, the recovery fraction of our sample is $> 80\%$ for $\theta_E > 5''$, and 100% of $\theta_E > 30''$ objects are recovered, with an average of 91% recovered for $\mathrm{SNR}_{\mathrm{eff}} = 5$. The reason for the drop off below $5''$ is partially due to the sample containing isolated galaxy lenses as well as smaller galaxy groups, and this method is naturally less sensitive to objects with fewer members. Using a lower $\mathrm{SNR}_{\mathrm{eff}}$ threshold of 3 allows for complete recovery of all $\theta_E > 10''$ objects, but this will come at the expense of a greater number of false positive detections.

found, as they describe in their paper, by finding the average distance between the bright arc (or candidate arc in the unconfirmed cases) and the object's centre. We use θ_E as a proxy for the lensing cross-section (and equivalently, mass) of each object as is commonplace in many lens models. Objects with small θ_E tend to produce smaller $\mathrm{SNR_{eff}}$, making up the majority of non-recovered objects with $\mathrm{SNR_{eff}} < 5$. In addition, above $\theta_E \sim 5''$, there is a slight correlation between Einstein radius and $\mathrm{SNR_{eff}}$, with the data in Figure 3.4 showing a Spearman correlation coefficient of $r_S = 0.504$, indicating clusters with larger Einstein radii generally produce slightly higher $\mathrm{SNR_{eff}}$. As there is inherent scatter in the Einstein radii for clusters of a given mass or richness in both the Smith et al. and Carrasco et al. samples, we would not expect a perfect correlation between the two variables. These results are further highlighted by Figure 3.5, which shows the fraction of objects recovered in bins of θ_E. The recovery fraction drops significantly for $\theta_E < 5''$, due to the inclusion of single galaxy and small group lenses within the Carrasco et al. sample, but is much higher ($> 80\%$ recovery) above this. Given that $\mathrm{SNR_{eff}}$=5 is fairly arbitrary, since $\mathrm{SNR_{eff}}$ is only an estimator for an object's overdensity, we can vary the cut to see the effect on recovery. A cut at $\mathrm{SNR_{eff}}$=3 increases the recovery rate at low Einstein radii fairly significantly, and allows the remainder of the larger radius objects to be recovered, giving 100% recovery for $\theta_E > 10''$. However decreasing the $\mathrm{SNR_{eff}}$ threshold will increase the proportion of false positives in a blind search, as we explore in the next section, so this must be done with caution.

The drop in recovery fraction for the $\theta_E < 5''$ objects is unsurprising, as some of these objects are single galaxy lenses or small galaxy groups, which will naturally be either impossible or very difficult to detect by any method sensitive to number density. It is also interesting to note that Figure 3.4 suggests the redshift of the object does not appear to have a major impact on whether the object is recovered or not. There are objects with a wide range of redshifts both above and below $\mathrm{SNR_{eff}} = 5$ – although the impact on $\mathrm{SNR_{eff}}$ due to redshift at the upper end of the range ($z \gtrsim 0.8$) is not well tested due to the scarcity

of these objects.

Figure 3.6 shows the $\mathrm{SNR}_{\mathrm{eff}}$ against the weighted number of galaxies detected in the matched VISTA-*WISE* catalogues within 1 arcminute of the map peak closest to the coordinates of each lens in our sample. As explained in subsection 3.4.2, the weighting is done based on the number of blended J-band detected galaxies within the PSF of each *WISE* detection. This affirms that the method is more sensitive to objects with a larger member number density, given that there appears to be a scattered but approximately linear relationship between the number of selected galaxies within 1 arcmin of the peak and the corresponding $\mathrm{SNR}_{\mathrm{eff}}$ (with Spearman correlation coefficient $r_S = 0.870$). We suspect the larger r_S for this relation compared to $\mathrm{SNR}_{\mathrm{eff}}$ against Einstein radius in Figure 3.4 is because the cluster richness will directly influence the pixel values within the map that drive the $\mathrm{SNR}_{\mathrm{eff}}$ calculation, and additionally because there is inherent scatter between Einstein radius values for a given cluster mass or richness. The calculations of N_{gal} here ignore the fact that each 1 arcminute region will be contaminated by galaxies that are not part of the group or cluster, however by assuming contaminant galaxies are randomly distributed (or close to it), this should only contribute to the scatter which can be overshadowed by the cluster overdensity.

Within Figure 3.4 and Figure 3.6, there are two clear anomalous data points that stand out from the rest. Firstly is the high redshift ($z \sim 1$) and high $\mathrm{SNR}_{\mathrm{eff}}$ ($\simeq 15$) point. This particular object is a high-redshift group that is closely aligned with a larger and closer cluster ($z \sim 0.3$) along the line of sight. Therefore, the detection appears with an inflated N_{gal} and hence $\mathrm{SNR}_{\mathrm{eff}}$ compared to objects at a similar redshift. The other is Abell 1835 – the object at $\mathrm{SNR}_{\mathrm{eff}} \simeq 35$, which is significantly higher than any other object in our sample, especially considering there are other clusters with similar N_{gal}. This object in particular has a large number of highly-weighted galaxies near to the cluster core, hence our method assigns this cluster a high $\mathrm{SNR}_{\mathrm{eff}}$ even among the large N_{gal} objects.

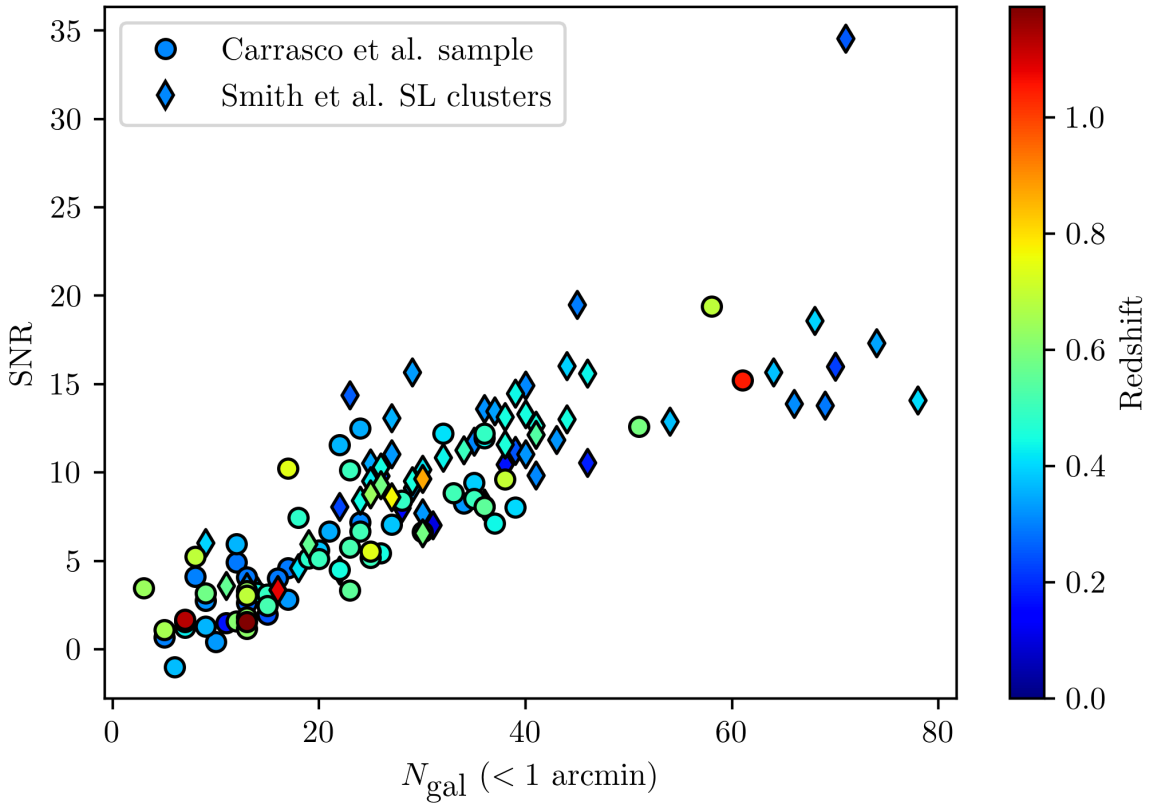

Figure 3.6: $\mathrm{SNR}_{\mathrm{eff}}$ of objects in the test sample against the number of galaxies detected within 1 arcmin of the corresponding map peak. The colour of each point indicates the redshift of the object. The $\mathrm{SNR}_{\mathrm{eff}}$ appears to correlate with the number of galaxies, although there is some clear scatter present. Therefore, $\mathrm{SNR}_{\mathrm{eff}}$ is a reasonable estimator for the richness of an object.

3.5.3 False positive rate estimates

Our method is based on counting galaxies without considering their colours. This is well matched to the available all-sky data given that the colour of galaxies in crowded cluster and group cores is challenging to measure accurately given the mis-match in angular resolution between ground-based J-band ($\lambda = 1.25\mu$m) and space-based $W1$ ($\lambda = 3.4\mu$m) photometry. In contrast, modern galaxy-based cluster- and group-finding algorithms typically incorporate colour information [e.g. 170, 173]. Objects detected by our method may therefore include projections of more than one group or cluster along the line of sight, and chance alignments of galaxies at very different redshifts that are indistinguishable from real groups or clusters when colour information is not taken into account. Given that our focus is on identifying group and cluster-scale dark matter halos capable of strong lensing, we regard the former (multiple groups and clusters) as a secure detection, and the latter (chance projection of field galaxies) as false positives.

We estimate the false positive rate from the population of detections in the sky regions surrounding the known lenses from the Carrasco et al. sample. Specifically, we check whether there are obvious peaks in the CFHTLenS photometric redshift catalogue associated with detections other than the known lens in our 0.3×0.3 degree $J/W1$-based maps centred on these lenses. In practice, this involved inspecting figures following the same format as Figure 3.7, which contains a series of images and plots produced using data from CFHTLenS, as well as J and $W1$ photometry, in order to confirm if the peaks correspond to real objects.

The left hand column of Figure 3.7 shows two images of the region in optical (top, from CFHTLenS) and in $W1$ (bottom, *WISE*). Cyan triangles mark the most likely cluster members: galaxies with colours consistent with the EzGal model, green circles mark those that are not. Orange symbols are galaxies within $10''$ of the provided centre coordinates for this object, and are candidates for the brightest central galaxies of the cluster. The

top-centre panel shows a zoomed in version of the density map ($3.75' \times 3.75'$), centred on the largest peak. The white plus signifies the coordinates of the object centre and the purple circle is the location of the peak. The top-right panel shows histograms of the redshifts of galaxies within the CFHTLenS catalogue (black), and a subset of those that also appear in the *WISE* data (green). The object's recorded redshift is marked with a red dashed line, and the photometric redshifts of the most central galaxies are marked with orange dashed lines. The bottom-centre panel shows a J-$W1$ colour-magnitude diagram, with the red dashed line indicating the colour predicted by the EzGal model for an L* cluster galaxy at the object's recorded redshift. The red transparent band marks a fiducial ± 0.2 error on this value. The bottom-right panel shows colour against the CFHTLenS photometric redshift for galaxies in the colour-magnitude diagram, with identical red lines to the bottom-centre and top-right plots showing the expected colour for the object and the recorded photometric redshift.

The primary resource for identifying whether the object is indeed a true detection is using the top-right plot and counting the number of peaks in the redshift distribution. In this case, using object SA6 which appears in Figure 3.7 as an example known lens, we would count two peaks, one at $z \sim 0.3$ and one at $z \sim 0.6$. We also stress that qualitatively the serendipitous detections near to SA6 are typical of those found in the outskirts of the maps. Note the broad distribution of $(J - W1)$ colour at the latter redshift, which arises due to our method in which we cope with the multiple possible matches for galaxies at the centre of dense cluster cores, occurring due to the PSF of *WISE* being distinctly larger than that of VISTA. In the absence of relying on galaxy colours, we naively match galaxies based on the closest entry in the other catalogue, up to a maximum separation of 1.4 arcseconds. Multiple matches are therefore common in high density cluster cores where multiple J-band detections are separated by less than the *WISE* PSF. This leads to inconsistent colour measurements either because a $W1$-band flux measurement contains contributions from multiple individual J-band sources (leading to an overestimate of $J - W1$), or because galaxies in different

wavebands are simply matched incorrectly.

In total we examine 269 serendipitous detections with $\mathrm{SNR_{eff}} \geq 3$, of which 70 have $\mathrm{SNR_{eff}} \geq 5$. At $\mathrm{SNR_{eff}} \geq 5$, 66 detections are associated with one or more redshift peaks and therefore are classified as secure detections in that there is clear evidence of one or more collapsed group/cluster-scale halos along the line of sight. This translates to a false positive rate of $\sim 6\%$ at $\mathrm{SNR_{eff}} \geq 5$. At $3 \leq \mathrm{SNR_{eff}} < 5$ we find that 158/199 serendipitous detections are associated with one or more redshift peaks, which implies a false detection rate of $\sim 20\%$. We also find no evidence of a strong trend in false positive rate at $3 \leq \mathrm{SNR_{eff}} < 5$, and expect an increase in false positive rate below $\mathrm{SNR_{eff}} = 3$ due to a large increase in the number of detections. To summarise, including $\mathrm{SNR_{eff}} > 3$ detections only increases the false positive rate of detections to 17% whilst producing almost four times as many real detections than if we include only the $\mathrm{SNR_{eff}} > 5$ detections. In addition, when comparing to our tests on objects from our test sample (subsection 3.5.2), extending the detection threshold down to $\mathrm{SNR_{eff}} \geq 3$ increases the recovery of lenses with small Einstein radii, $3 < \theta_{\mathrm{E}} \leq 5\,\mathrm{arcsec}$ from $\simeq$ 40 per cent to $\simeq$ 70 per cent (Figure 3.5). This is encouraging for building a watchlist based on J and $W1$-band photometry in advance of LSST, especially bearing in mind that photometric redshifts from LSST photometry and spectroscopic redshifts from surveys taking advantage of the 4MOST instrument will be efficient tools to subsequently suppress the false positives. Therefore, we believe $\mathrm{SNR_{eff}} > 3$ to be a sufficient threshold for selecting detections of real objects to include in a lensed transient watchlist.

3.5.4 Testing on Rubin DP0 data

The Rubin Observatory Data Preview 0 (DP0) is a programme providing access to simulated LSST-like data and images. These data were produced following the Dark Energy Science Collaboration's (DESC) second data challenge [188], whereby the results of N-body

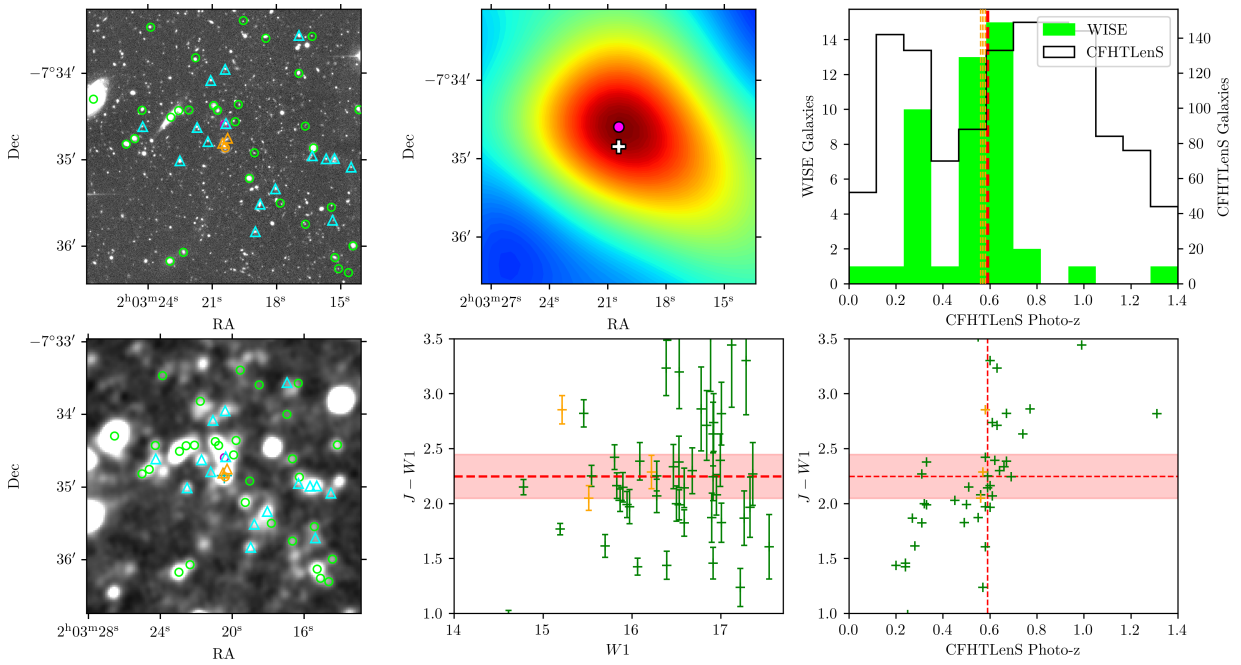

Figure 3.7: Example of a series of plots used to confirm the existence of objects within our test sample, at the coordinates provided by the original source. This series represents object SA6 from the [184] sample. Top-left: an image of the region from optical CFHTLenS data showing the galaxies detected within the J and $W1$ data. Top-centre: A zoomed in version of the density map, centred on the largest peak, highlighting the closeness of the peak to the recorded coordinates of the object. Top-right: histograms of the redshifts of galaxies within the CFHTLenS catalogue (black), and a subset of those that also appear in the *WISE* data (green). This shows two distinct redshift peaks at $z \sim 0.3$ and 0.6 indicating the presence of real collapsed objects at these redshifts. Bottom-left: same as top-right, except using *WISE* imagery. Bottom-centre: a J-$W1$ colour-magnitude diagram for the galaxies within this region, showing a cluster red sequence in accordance with the predicted colour for the object. Bottom-right: colour against photometric redshift for galaxies in the colour-magnitude diagram. This shows a cluster of points around the predicted colour and recorded photometric redshift of this object, furthering the evidence for a real object at this location.

simulations are passed through a model of the Rubin hardware before being processed by the official LSST pipelines, producing a catalogue of objects that is representative of what is to be expected from the Rubin telescope. It includes data for 300 square degrees of sky in all six Rubin bands and is based on stacked images containing five years of observation data. The objects within the simulation reach out to $z = 3$, however not every object will necessarily be detected following the processing steps. The base simulated data set contains information on individual dark matter halos and the galaxies bound to them, presenting an opportunity to test our method on data where the true underlying distribution of dark matter halos is known.

We applied the method on a single 0.5×0.5 region of the DP0 catalogue that was known to contain a significant number of massive and less-massive halos. We select galaxies by choosing extended objects that are detected in the y-band brighter than 21.1 mag, which corresponds to the J-band detection limit of VISTA corrected to the y-band using the expected y-J colour for an L* galaxy as calculated using the same EzGal model as described in section subsection 3.3.3. Our selection is therefore tuned to be as similar as possible to the current detection limits of VISTA J-band, and makes for a reasonable comparison despite the DP0 dataset being significantly deeper. All other parameters used in creating and convolving maps are identical to those used with the VISTA and *WISE* data as described in section 3.4.

Within the simulation test region, there are 41 dark matter halos with $M \geq 10^{13}\mathrm{M}_\odot$ at $z < 1$. We restrict to this redshift as the selection is tuned to the detection limits of $L^\star$ cluster galaxies in the J-band as shown in Figure 3.1, which we estimate to be detectable up to $z \sim 1$. Figure 3.8 shows the map for the test region, with the locations of the 41 dark matter halos overlaid. Firstly, it is reassuring to note that the qualitative distribution of these dark matter halos mostly follows the higher $\mathrm{SNR}_{\mathrm{eff}}$ regions of the map, which matches expectations. The map contains 9 peaks with $\mathrm{SNR}_{\mathrm{eff}} > 3$, all of which are within 1 arcmin of

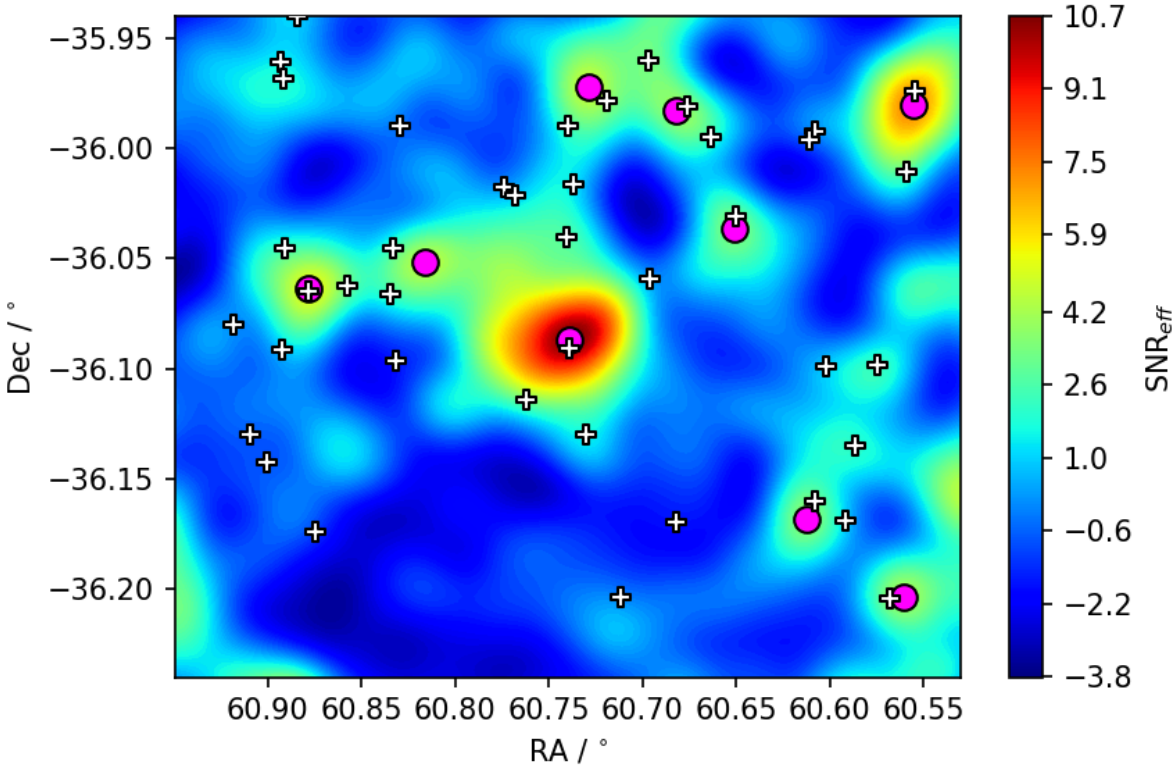

Figure 3.8: The map produced for the test region of simulated Rubin data. Magenta dots mark the locations of peaks with $\mathrm{SNR_{eff}} > 3$, and white pluses mark centres of dark matter halos with mass $M \geq 10^{13}\mathrm{M}_{\odot}$. Qualitatively, the distribution of dark matter halos follows the high $\mathrm{SNR_{eff}}$ regions of the map, which is indicative that the method is functioning as expected. The 9 peaks are all located within 1 arcmin of a dark matter halo, indicating the method has a low false positive rate when cutting at $\mathrm{SNR_{eff}} = 3$.

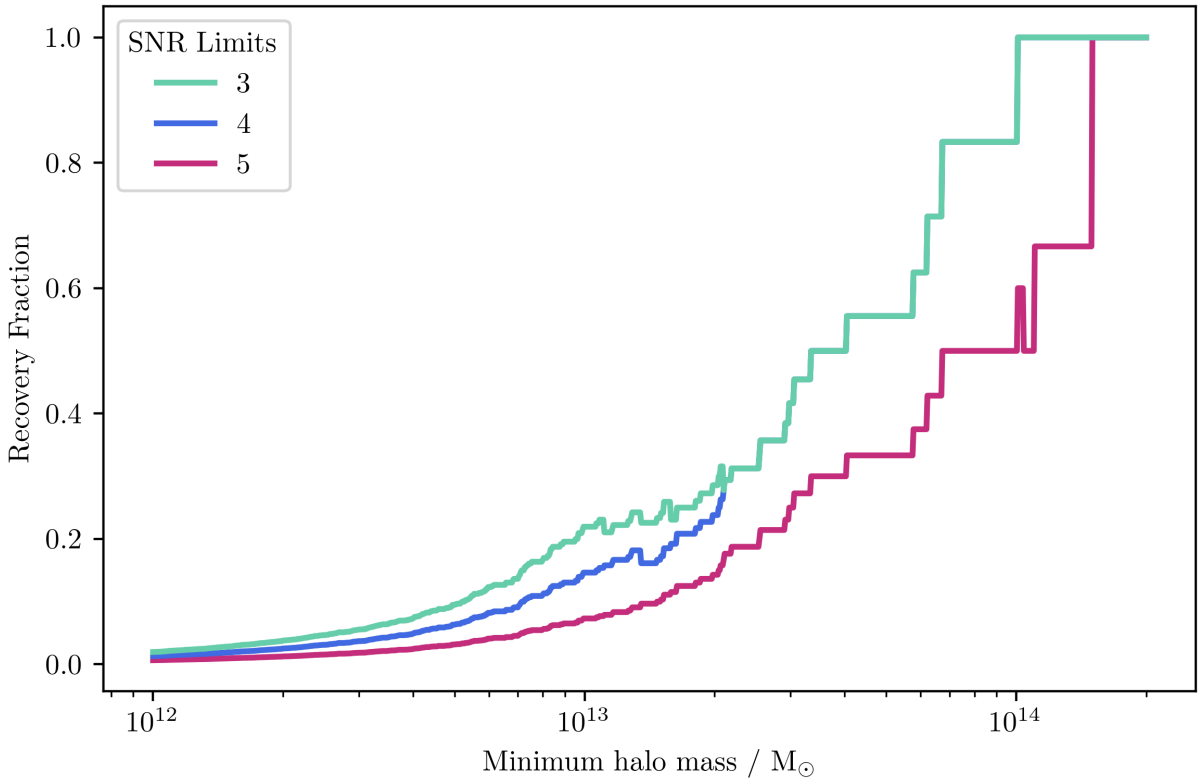

Figure 3.9: The recovery fraction of dark matter halos within the test region of simulated Rubin data as a function of halo mass. We calculate the fraction of halos greater than a given mass that are recovered by the method, where an object is considered to be recovered if it is the closest object within 1 arcmin of an $SNR_{eff} > 3$, 4 or 5 peak (note that the $SNR_{eff} = 3$ and 4 curves are identical above $M \sim 2 \times 10^{13} M_\odot$). The recovery rate using the simulated data matches well to the real data, with a good rate at high masses, that falls off at smaller values due to the difficulty in detecting those with fewer members. The ability to recover objects associated with massive dark matter halos does not explicitly match the goals of using the method, but it is sufficiently related, easy to test and gives a reasonable metric for the method's capability.

at least one of these halos. Therefore none of these peaks can be considered a false positive detection, based on the definition established in the previous section, which further affirms and is consistent with our previous evaluation that the false positive rate of the method is low when cutting at $\mathrm{SNR}_{\mathrm{eff}} \geq 3$.

In order to quantify the recovery fraction of objects within the test region, we assume that the halo closest to each peak is the one which provides the greatest contribution to that peak's signal, and hence is the object considered to be recovered by the presence of the peak. In reality, any given peak arises from the contribution of many objects that may be related to multiple different halos, however this simplification allows us to relate the recovery to a single parameter – the halo mass. We vary the minimum mass of the halos we consider, and plot the recovery fraction (as defined above) as a function of the halo mass in figure Figure 3.9, and for this we extend the lower mass cut for halos down to $10^{12}\mathrm{M}_{\odot}$. This shows the rate stays high (above 80 per cent for $M > 7 \times 10^{13}\mathrm{M}_{\odot}$ clusters) for halos with greater mass that have more bound galaxies, but drops as we extend to include the less-rich lower mass halos which do not produce as strong of a signal in the map. Whilst this plot is informative, it is not entirely representative of the goal of this method, which is to locate high-density lines of sight rather than recovering individual objects of a particular halo mass. Therefore, the decreased recovery rate at lower halo masses is not a pressing issue, because those that we do detect are the objects that have the greatest central number density between those of similar mass and redshift, and hence are the more efficient lenses.

3.6 Summary

We have described a proof-of-concept for a method which has the capability to discover galaxy groups and clusters across the entire sky out to $z \sim 1$ using only existing J and $W1$-

band wide-field data from the VISTA/UKIRT and *WISE* instruments, respectively. The objects found using this method are intended to be added to a watchlist of groups and clusters in order to locate candidate gravitationally lensed transient events such as supernovae, kilonovae, gravitational waves and gamma-ray bursts from various wide-field survey data streams. The lensing nature of these events would then be confirmed utilising further follow-up observations. In testing, our method successfully recovers between 80 and 100% of a sample of large Einstein radius ($\theta_E \geq 5''$) galaxy clusters, and 40 to 70% of smaller Einstein radius objects (dependant on individual radii and the detection threshold used). We also estimated the false positive rate of the method by investigating the surrounding regions of test objects that the method identifies as likely to contain a group or cluster. By inspecting telescope images and by producing and inspecting both colour-magnitude diagrams and plots of the photometric redshift distribution of galaxies local to these candidates, we searched for evidence of real group or cluster objects at these locations. Using these, we were able to constrain the false positive rate for significant detections to be between approximately 6 to 20%, depending upon the applied $\mathrm{SNR_{eff}}$ detection threshold. We use $\mathrm{SNR_{eff}}$ as the metric to determine the significance of detections with our method, and it is analogous to determining the number of standard deviations a detection is above a background of completely randomly distributed galaxies. Our investigations clearly show that the applied value of the $\mathrm{SNR_{eff}}$ threshold changes both the level of completeness and the false positive rate of the method. Using a higher $\mathrm{SNR_{eff}} = 5$ threshold results in secure detections of most large Einstein radius clusters with a very low false positive rate, but conversely produces a less complete catalogue due to many groups and clusters with smaller Einstein radii being detected with lower $\mathrm{SNR_{eff}}$. However, we can significantly increase the recovery of the smaller Einstein radius objects from 40 to 70% using a lower $\mathrm{SNR_{eff}} = 3$ cut, whilst still only producing 20% false positives. Therefore, we can increase the prospects of lensed transient detection by increasing the completeness of our watchlist using a lower cut, whilst still producing a manageable number of false positives. We also anticipate being able to suppress the number of false

positives in the future once data from Rubin becomes available. We also tested the method on simulated data from the Rubin DP0 programme, that was selected to be comparable to currently available data sets. Testing on this data has the advantage of knowing the true underlying distribution of the dark matter halos that drive the formation of lenses in our universe. This test provides similar results, indicating a good recovery rate (¿80% for halos above $10^{14}M_{\odot}$) and a low number of false positives.

Chapter 4

Searches for lensed transients using a prototype watchlist

The contents of this chapter involve an assortment of original work conducted by myself and collaborators, some of which is published and some of which is not. Here, I outline my personal contributions to each, ordered by section. In section 4.2, I am responsible for updating and maintaining the prototype watchlist for all except the very first version of 130 strong lensing clusters, which was assembled by Dr. Graham P. Smith [122]. In section 4.3 I was responsible for setting up, conducting, and analysing the findings of the lensed transient search, as well as taking the role of Principal Investigator for the Liverpool Telescope proposal from July 2022 onwards (previously Dr. Graham P. Smith). This study was completed alongside many collaborators – see [186] for a complete list. In section 4.4 I describe the results of an observational programme lead by Dr. Matteo Bianconi [187]. My contribution was to aid in the deduction of candidates for observation and most of the other work completed here was done by collaborators. Therefore I only give a brief overview of this work. In section 4.5 I describe a currently unpublished search for lensed GRBs that I am

actively involved in, alongside Ben Jones, Dr. Graham P. Smith and Dr. Ben Gompertz. The search for candidates itself was done by Ben Jones, and I describe my personal contribution to this project, involving some of the analysis of candidates that were produced by this search.

4.1 Introduction

In this chapter I discuss searches for lensed transients that I have been involved in and that have been ongoing for the past four years during my studies as a PhD student. These involve utilising a prototype watchlist, that has evolved over time, to search for candidate lensed transients that have occurred nearby to known galaxy groups and clusters, following the concept introduced in chapter 2. This search will eventually be supplemented with clusters found using the method described in chapter 3. In total, three types of transient have been considered for searches of lensed variants: GWs (and their kilonova counterparts), SNe and GRBs. This chapter will describe the construction of the watchlist used, as well as the data, methods and results associated with each search.

4.2 The prototype watchlist

The watchlist for these searches is only considered a prototype as it consists of clusters that were not detected for the purpose of finding lensed transients. Specifically, these clusters are not always from catalogues that cover the entire sky (or, the entire footprint of the relevant transient-detecting survey), and do not necessarily cover the relevant redshift range of $z \lesssim 1$, that was motivated in chapter 3. The first variation of the watchlist consisted of only 130 previously-identified strong lensing clusters with spectroscopically confirmed multiple images

or gravitational arcs, assembled and utilised by [122] for searches for lensed GWs in the first LIGO/Virgo observing runs O1 and O2. Following the results of chapter 2, it was understood that this search method will not include the complete sample of objects responsible for the lensing of transients if the watchlist only consisted of clusters that are known strong lenses. Therefore, there became a clear incentive to boost the number of clusters within the list.

During the development of the method presented in chapter 3, our watchlist-based searches would need to to take advantage of clusters from other pre-existing catalogues, which whilst not ideal in terms of sky coverage and redshift, would at least enable the possibility of discovering lensed transients in the interim. Therefore, the watchlist was supplemented by the clusters from the CODEX [189], redMaPPer [170] and Planck-SZ2 [169] catalogues.

The *Planck* telescope is a space-based microwave and infrared observatory dedicated to the study of the cosmic microwave background (CMB). It is the mission that is responsible for the most precise measurements of cosmological parameters to date (including the same early-universe measurement of H_0 that is now in significant tension with local-universe measurements from the cosmic distance ladder). However, an additional science goal of *Planck* was to take advantage of the thermal Sunyaev-Zeldovich (SZ) effect [168] in order to search for galaxy clusters. The SZ effect acts like reverse Compton scattering – photons (in this case from the CMB) interact with electrons within hot intra-cluster plasma. These photons gain energy and hence locally alter the CMB spectrum, allowing the presence of clusters to be inferred. Planck-SZ2 is the second catalogue of galaxy clusters assembled with Planck data using this method, and contains 1653 detections (with 1203 confirmed as clusters through external data). Planck-SZ2 is an all-sky catalogue, making it ideal for our lensed transient searches. In addition, the SZ effect cluster selection function is flatter at higher redshifts than those detected by x-rays or photometric methods [190], enabling some detection of clusters at higher z and toward the coveted $z \sim 1$ limit.

A disadvantage of the Planck-SZ2 catalogue is its lack of sensitivity compared to other methods, and produces the fewest detections per unit solid angle out of the catalogues we utilise. For example, the redMaPPer catalogue contains $\sim 25,000$ clusters over only $\sim 10,400$ sq. degrees ($\sim 1/4$ of the sky), compared to $\sim$1600 over the entire sky with *Planck*. However, redMaPPer is not all sky – it is contained within the footprint of the Sloan Digital Sky Survey (SDSS, [191]) – and has a much more restrictive upper redshift limit of $z \sim 0.55$, highlighting further differences between the outcomes of different cluster detection methods.

The redMaPPer catalogue was assembled utilising the red sequence method – clusters are found by identifying a horizontal trend of galaxies on a colour-magnitude diagram, i.e. galaxies in a cluster have very similar colours, irrespective of their individual brightnesses. This effect is attributed to the stars of galaxies in a cluster all having similar metallicities [192]. By combining the Planck and redMaPPer catalogues, we have a prototype watchlist that is all-sky, but is much more complete within the SDSS footprint. Given that this footprint is predominantly in the northern hemisphere, this watchlist has good synergy with searches for lensed SNe using ZTF (see subsection 4.3.2), which monitors the northern sky, and provides further motivation for prioritising a southern sky watchlist using the method presented in chapter 3.

The CODEX (COnstrain Dark Energy with X-rays) cluster survey utilises the redMaPPer cluster finding algorithm on SDSS data, but specifically targets regions where known x-ray sources from the ROSAT All-Sky Survey (RASS, [193]) are present. This means the catalogue has overlap with the redMaPPer clusters, given that they cover an identical survey region. We treat CODEX as an extension to the redMaPPer catalogue, to ensure the watchlist is as complete as possible, and covers detection from a wide variety of methods.

A final consideration that was made for this prototype watchlist was the precision

of the cluster coordinates provided by the Planck-SZ2 catalogue. The typical positional uncertainty given for each cluster in this catalogue is a few arcminutes, which is much larger than a typical galaxy cluster's Einstein radius (even the most extreme clusters have $\theta_E \lesssim 1$ arcmin [11]). A significant offset between the recorded and true centres of these clusters would render them unsuitable for the watchlist, as only background sources aligned within $\sim \theta_E$ of cluster cores are candidates to be strongly lensed. This motivated a study to locate the brightest central galaxy (BCG, a proxy for the cluster core) within each of the Planck clusters that are within the redshift range relevant to the lensing of transients ($z \geq 0.1$, motivated by the inefficiency of low-redshift lenses). The project was initially piloted by second year undergraduate students whom I supervised during an astronomy-based project module in Spring 2021, and was continued by one of these students, Josh Smith, over the Summer. This resulted in coordinates for 306 candidate BCGs in the southern hemisphere for the most relevant Planck clusters, and hence significantly improved the astrometry for these watchlist objects. This work is currently in preparation, and will be published under Smith, Joshua C. et al. in Research Notes of the American Astronomical Society.

The final version of the prototype watchlist was assembled from cluster detections within the catalogues described above. No explicit cuts are made for which clusters are included, given that even by including all of them a manageable number of transients that require manual inspection are produced daily. This watchlist population strategy will need to be revisited in the future to prioritise specific objects (likely based on estimates or proxies for Einstein radius or redshift), when the number of watchlist clusters and transient detections increases following the adoption of new cluster finding methods and transient finding surveys, and at which point it becomes too time consuming to manually vet every potential candidate.

4.3 Searches for lensed SNe using ZTF/Lasair and the Liverpool Telescope

4.3.1 The Lasair Transient Broker

Lasair[1] is one of the seven transient broker systems that will provide the astronomical community with information about transients detected with the Rubin observatory as they occur in real time [194]. Since the Rubin observatory is not yet operational, Lasair is currently operating on data ingested from the ZTF survey. This synergises well given that Rubin will cover the southern hemisphere and ZTF covers the northern hemisphere, providing full coverage of the transient sky. Therefore, searches for lensed transients in the interim can be conducted using ZTF data until Rubin data become available, albeit at a much lower sensitivity.

Lasair obtains images from the ZTF telescope in real time throughout nightly observations and uses these to detect and classify transients. Reference images of the entire sky have already been obtained by the telescope, and are subtracted from any subsequent images taken to create difference images. Doing so reveals pixels that have increased or decreased photon flux compared to the reference image. This makes it straightforward to identify explosive transients, but also other types of repeating transient such as transiting binary stars, variable stars or quasars/AGN. If a photon excess or reduction is detected in particular pixels in concurrent observations, then a lightcurve of the transient can be built up. Lasair will automatically produce these using the information from the difference images, adding to them as more data are recorded. The ZTF survey observes in two bands, g and r, hence a lightcurve can be produced for each.

[1] https://lasair-ztf.lsst.ac.uk

In addition, Lasair provides a preliminary classification of each detected transient using the Sherlock software package [195]. In short, this works by first cross-referencing many databases of known objects, containing (variable) stars, quasars/AGN and previously identified transients, then classifies accordingly. If the transient does not line up with any of these, then it provides a likely alternative classification based on whether the pixel excess/reduction is in the proximity of a galaxy. If it is, this would imply a SN or nuclear transient (such as a tidal disruption event), and if not the transient is labelled as an 'orphan'. This system is extremely useful for quickly separating the SN candidates from transients with stellar or AGN origins that make up a significant fraction of the total detections and are not of interest for lensed transient studies.

The main function of Lasair for our purposes is that it allows the construction of queries to specifically target transients that satisfy particular conditions, and that these conditions can be linked to objects within a pre-defined watchlist. As a result, searches for lensed transients can be performed by uploading a watchlist of galaxy clusters and filtering the incoming data to only relevant transients – those that are both nearby clusters and *resemble* SNe. The next section will discuss these conditions in more detail. This system allows for a straightforward and functional way to systematically narrow down a huge number of transient detections to just a handful per night, which can then be manually inspected in order to confirm if a transient is indeed a candidate for being lensed.

4.3.2 Identification and follow-up of lensed SN candidates

Implementing the cluster watchlist into Lasair is simple as it requires only three pieces of information per cluster: coordinates, a unique identifier and a search radius. Coordinates are taken directly from the source catalogue, and identifiers are assigned based on the unique identifiers provided in the base catalogue (e.g. redmapper-33292 is used for the redMaPPer

cluster with ID 33292). The search radius is the maximum separation in radius from the specified coordinates within which Lasair should search for transients. In theory, one could adjust this value based on the Einstein radius (or similar proxy such as the mass) of the cluster, and reduce the number of interloper transients found far from smaller θ_E clusters that would not be lensed candidates. However, a constant search radius of 1 arcmin was used for every cluster, which was chosen as an approximate upper limit on the Einstein radius of a massive galaxy cluster in line with values of those in our initial watchlist of 130 clusters. This simplified the analysis by removing any ambiguity arising from uncertainties in determining Einstein radii of clusters, whilst still returning a manageable number of transients to manually vet. Future iterations utilising Rubin data and a longer cluster watchlist will result in an increase in the number of transients by approximately two orders of magnitude, meaning a more systematic approach will be required in order for this method to remain feasible.

Candidate lensed SNe from Lasair have three requirements for them to be considered for further investigation. In addition to proximity to a watchlist cluster, they are required to be 'new' transients and have a SN-like classification. This is information that can be easily filtered out using queries with Lasair. A transient is classed as 'new' if it is the first time it has been detected, meaning there is no historical data associated with any object at its coordinates, and hence does not already have a specific ZTF-designated name. In practice, this filter was not strictly applied as it is plausible that a multiply-imaged SN could be re-detected multiple times following a time delay, and the number of candidates to vet was not significantly decreased by including it. However, this information was taken into account during the manual vetting process. For a transient to resemble a SN, it must not be associated with a known (variable) star or AGN from the various catalogues utilised by the Sherlock identifier and therefore is only classified by Sherlock as either a Nuclear Transient (NT), Supernova or Orphan. The relevant transients are not restricted just to the Supernova

class, as NTs, SNe and Orphans jointly only make up a small (approximately 10%) fraction of the total query, and so including them all has minimal impact on the number of transients to inspect. In addition, classification between these types is based solely on the galaxies associated with the transients – NTs are transients resolved within galaxy cores, SNe are those resolved within the outer extent of galaxies, and Orphans are those that do not fall into either category (i.e. no associated galaxy). It is currently not clear whether there is significant overlap between true NTs classed as SNe (and vice versa) with Sherlock, so the safest option is to include both categories. Furthermore, associated galaxies need to be either resolved or exist within an external catalogue, meaning Orphans must also be included to ensure transients with unresolved hosts are not automatically discarded.

The manual inspection process for identifying candidate lensed transients follows a few main steps. The first and possibly the most important consideration to make is the proximity of the transient to the cluster. Those located far from the cluster core are unlikely to be lensed and can immediately be ruled out as lensed candidates. Of course, this depends on the richness of the cluster – redMaPPer provides a richness estimate and Planck provides a mass estimate which can be used as proxy – with richer clusters supporting a larger maximum separation. The richer clusters also tend to be clear simply from inspecting telescope images, by the presence of greater numbers of large elliptical galaxies.

The second step of inspection is to try to rule out the possibility of the transient being a contaminant foreground SN hosted by a cluster galaxy. Type-Ia SNe are the most commonly-occurring SN within any magnitude-limited survey due to their intrinsic brightness, hence SN-Ia that are within the cluster (and therefore not lensed) are the dominant source of contamination. At the 5σ observation depth of ZTF, a typical Type-Ia is observable out to $z = 0.16$, meaning extra caution must be taken when vetting a transient located near a cluster with redshift around or below 0.16. In this case, there needs to be further evidence from the lightcurve post-peak that the SN is deviating significantly from a Type-Ia

to be considered a candidate lensed SN rather than a cluster SN. This can be done either by the shape of the lightcurve, or by considering the typical peak magnitude of a Ia at the cluster redshift – however this second argument can be less useful given the ~ 1.5 mag range of Ia peak brightness. Higher redshift clusters do not need to take this into account, as it is unlikely a Ia within the cluster would be resolved with ZTF.

In addition to the information provided by ZTF and Lasair, data from other catalogues are useful for determining the true nature of candidates. A commonly occurring scenario is when the transient host galaxy is in the foreground of the nearby cluster. This can sometimes be very obvious just from sky images (Lasair hosts PanSTARRS imagery showing the location of the transient), but galaxy redshifts or photometry from external databases such as the NASA/IPAC Extragalactic Database (NED) can be used to confirm this. Furthermore, we have witnessed Sherlock mistakenly class an asteroid as a SN-like transient, which was identified as a possibility by the alternative ALeRCE broker, and confirmed by using the NASA Small-Body Database to the presence of an asteroid at the time and location of the transient detection. Finally, for bright or low-redshift sources, we can make use of the Asteroid Terrestrial-impact Last Alert System (ATLAS). This is a group of telescopes that regularly scan the sky searching for near-Earth asteroids [196], and during these observations discover 10 to 15 SN candidates per night [195]. ATLAS operates in cyan (c) and orange (o) bands – different to those used by ZTF, which can provide complementary photometric information for identification of SN types by lightcurve or colours. ATLAS data are accessible via a forced-photometry server, so it is straightforward to check whether data exists for a ZTF transient at its specified position. However, this is only feasible for very bright objects, due to the low relative sensitivity of ATLAS.

For lensed SN candidates that are not ruled out by alternative classifications, we require further observations in order to confirm if they are indeed lensed. This is possible with high-resolution imagery and spectroscopy from large telescopes, although time on such

instruments is valuable and sought-after. Therefore, convincing arguments that the target is of significant interest must be made for any such follow-up to take place – in this case, strong evidence that the candidate is indeed likely to be lensed – and this requires more than what ZTF alone can provide. One way to do this is by inferring the redshift of the SN, which can be done using their observed colours in the absence of spectroscopy. Figure 4.1 below shows the expected evolution of SN r-z colours with redshift, based on models from [197]. The maroon-dashed line shows the evolution for Type-Ia SNe, whereas the grey solid lines bound the region expected for Type-II SNe. The black data points represent SNe from the Open Supernova Catalogue with precise photometry defined by the error on r-$z < 0.2$ mag within one day of the r and z-band lightcurve peaks. Lensed SNe will be more distant, and hence redder due to the faint rest-frame UV emission being redshifted into the optical bands. Therefore, one can cut by colour to select candidate lensed SNe by virtue of being redder than expected. The dotted black lines represent a fiducial colour cut r-$z = 0.5$ for a cluster at $z = 0.7$, however this cut is to be tuned based on the redshift of the nearby cluster, as the cluster redshift dictates the distribution of SN redshifts that it is likely to lens, and hence the distribution of possible colours. SNe redder than this cut are very strong candidates for being high redshift, and therefore also lensed. All of the very red points between $0.8 \lesssim z \lesssim 1.0$ in the figure are Type-Ia, which would not be observable with ZTF without the aid of lensing. In addition, the high-redshift ($z \gtrsim 1.5$) points are all superluminous SNe, which would emerge as a much rarer and more sought-after contaminant, given that only ~ 100 have been discovered to date [34].

In summary, the best candidates for lensed SNe are those with very red r-z colours that are located nearby massive galaxy clusters. In order to obtain the required r- and z-band photometry, myself and collaborators have been awarded Liverpool Telescope time to follow up two SNe per semester (approximately 9 months, with 2 months overlap between subsequent semesters) for six semesters total, to date. This time was to be spent on follow-

ing up promising candidates from our search using Lasair, in order to further solidify the lensing interpretation of these SNe. During this time we triggered observations on only one candidate, which was ultimately ruled out as lensed following these observations (see details in subsection 4.3.3).

4.3.3 Notable candidates from ZTF/Lasair

For the duration of the search for lensed SNe using the watchlist with Lasair, a few notable objects were found near to galaxy clusters. The first of these was picked up by our watchlist query in February 2021, and was labelled as ZTF21aaoleaj. The object was initially of interest as it was located very closely (8 arcseconds) to the core of galaxy cluster SDSSJ1004+4112. Sherlock classified the object as an AGN, meaning it was coincident with a catalogued object and was likely not triggered by detection of a SN. However, it is uncommon for objects to occur so close to a cluster core, so further investigation was initiated. This particular AGN was fairly well-documented in the literature, and is indeed strongly lensed, with four images that are bright enough to be resolved even with ZTF imaging (see Figure 4.2). This was therefore triggered by variability in one of the images of the quasar. The cluster and lensed quasar system had been previously observed using *Hubble's* Advanced Camera for Surveys (ACS), measuring a redshift $z = 1.74$ for the quasar, and noting its variable nature [132]. Whilst a new discovery had not been made, it was reassuring to be able to locate a previously known cluster-lensed source from an object within our prototype watchlist, and was especially exciting to see the multiple images resolved in the ZTF imagery. One would expect the variation in this quasar image to be observable in other images, following some time delay. [86] lists the predicted time delays and magnifications for each of the quasar images (the image associated with ZTF21aaoleaj is labelled image B), and predicts that one image (image A) should lead B by only $\sim$ 40 days. In addition image A boasts a greater

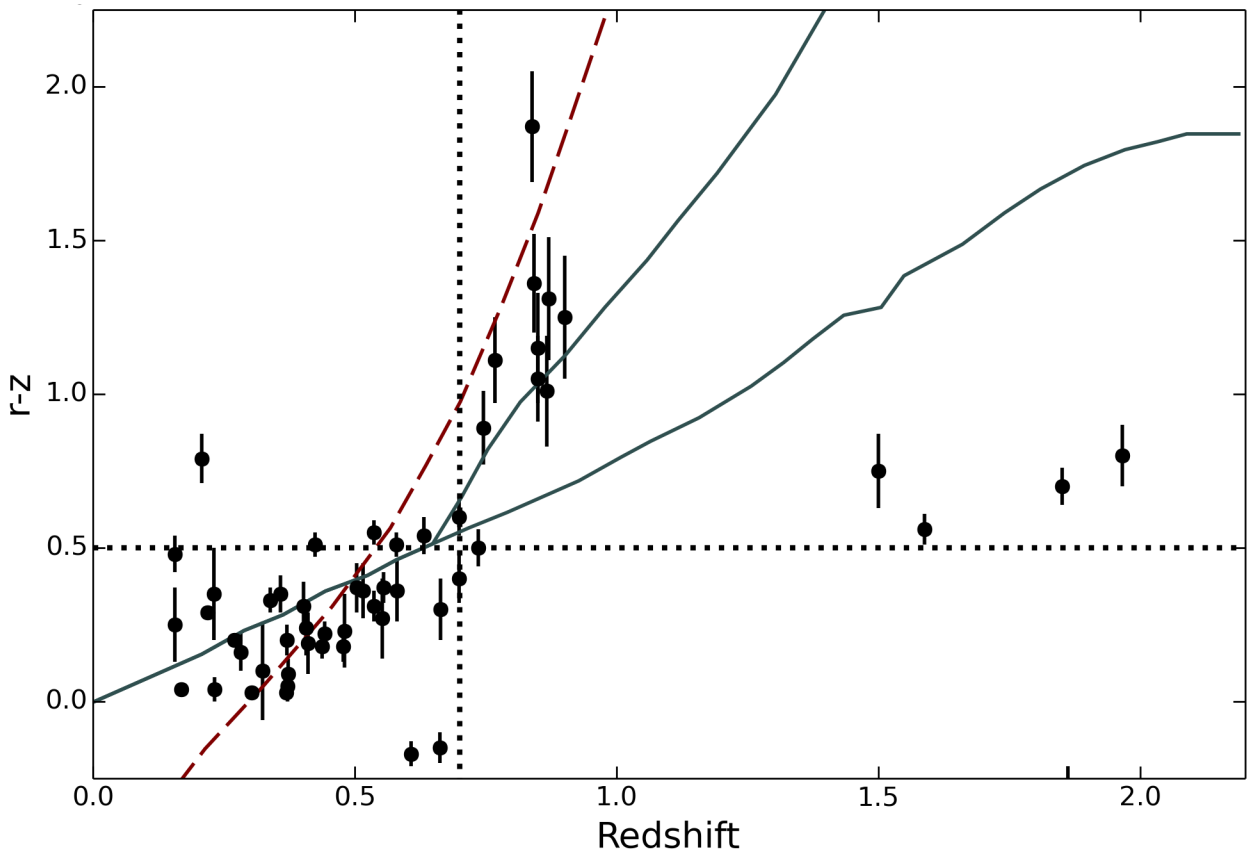

Figure 4.1: r-z colour evolution of SNe as a function of redshift. The dashed maroon line represents the predicted evolution for Type-Ia SNe, and the solid grey lines bound the range of colours associated with Type-II SNe, based on models presented in [197]. Black points represent a subset of SNe from the Open Supernova Catalogue, with r-z errors of < 0.2 mag and photometry within one day of the lightcurve peak. Dotted lines represent a fiducial colour cut for SNe found near a high-redshift $z = 0.7$ galaxy cluster. All of the very red SNe between $0.8 \lesssim z \lesssim 1.0$ are Type-Ia, which would not be observable with ZTF without the aid of lensing. Lensed SNe are biased towards higher redshifts, which implies a redder colour as faint emission in the rest-frame UV is shifted into the optical bands. Therefore, red SNe that are found near a watchlist galaxy cluster are strong candidates for being lensed and should therefore be followed up spectroscopically to confirm the lensing hypothesis.

magnification than image B, ruling out that it may not have been detectable. However, ZTF21aaoleaj is the only detection that appears in the watchlist query, or even following a cone-search of the entire Lasair database. The same variability in other images of the quasar may be detectable, but only in the future due to the much longer relative time delays ($\gtrsim 3$ years).

The second notable ZTF-detected watchlist transient was designated ZTF21abqoivk, and received a separate designation AT 2021vkz (later SN 2021vkz) by the Transient Name Server (TNS)[2]. Lasair reported the transient as a SN in close proximity to the galaxy cluster WISEA J230324.99+075643.5 (CODEX ID:54796). This was an interesting candidate as it appeared within $\sim$ 30 arcsec of the centre of a galaxy cluster, and was also only a few arcsec from one of the brightest cluster galaxies. Therefore, if this was a background SN it had a good possibility of being strongly lensed by the presence of the large galaxy in the foreground, which receives an additional boost from the cluster dark matter halo. The ZTF lightcurve for this object was sparse, with only five total data points across three observation epochs (see Figure 4.5).

As a result, follow-up observations with the Liverpool Telescope were triggered, and the results of the observations were reported to the TNS via an AstroNote [186]. The perceived outcome was that the colours and apparent magnitudes were consistent with a Type-Ia SN at the redshift of the galaxy cluster ($z = 0.15$), and so further follow-up was not pursued. Two days following the publication of our AstroNote, an independent group obtained a spectrum for the source using the LRIS instrument on the Keck 10m telescope, and confirmed the source to be a Type-Ia SN at the cluster redshift, in line with our expectations [198]. It is not known whether our observations prompted this additional follow-up. This securely

[2]The TNS is the official service provided by the International Astronomical Union (IAU) where transients can be reported. New transients are given the prefix AT, but confirmed supernovae will eventually be promoted to have the prefix SN.

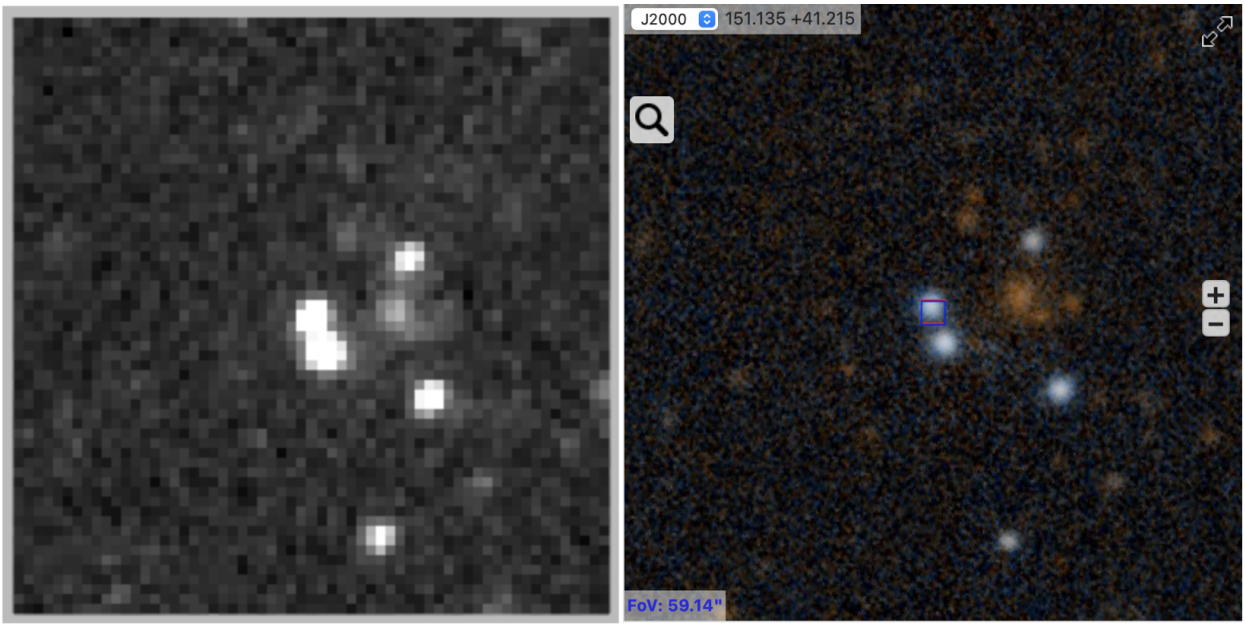

Figure 4.2: Left: ZTF r-band image of the lensed images of a $z = 1.74$ quasar initially discovered by [132]. Variability in the leftmost source was picked up by Lasair as a transient, recorded as object ZTF21aaoleaj, and was picked out by the query looking for transients near clusters in the watchlist. The core of the galaxy cluster lens, SDSSJ1004+4112 can be seen in the centre of the four resolved quasar images. Right: PanSTARRS colour-composite image of the same region, highlighting the quasar image that triggered ZTF21aaoleaj (red square). The blue square highlights the position of the catalogued source used by Sherlock, which overlaps. The faint red sources are the galaxy cluster members, whilst the encircling four blue sources are the multiple images of the quasar. The southern-most blue source is an unrelated non-lensed quasar.

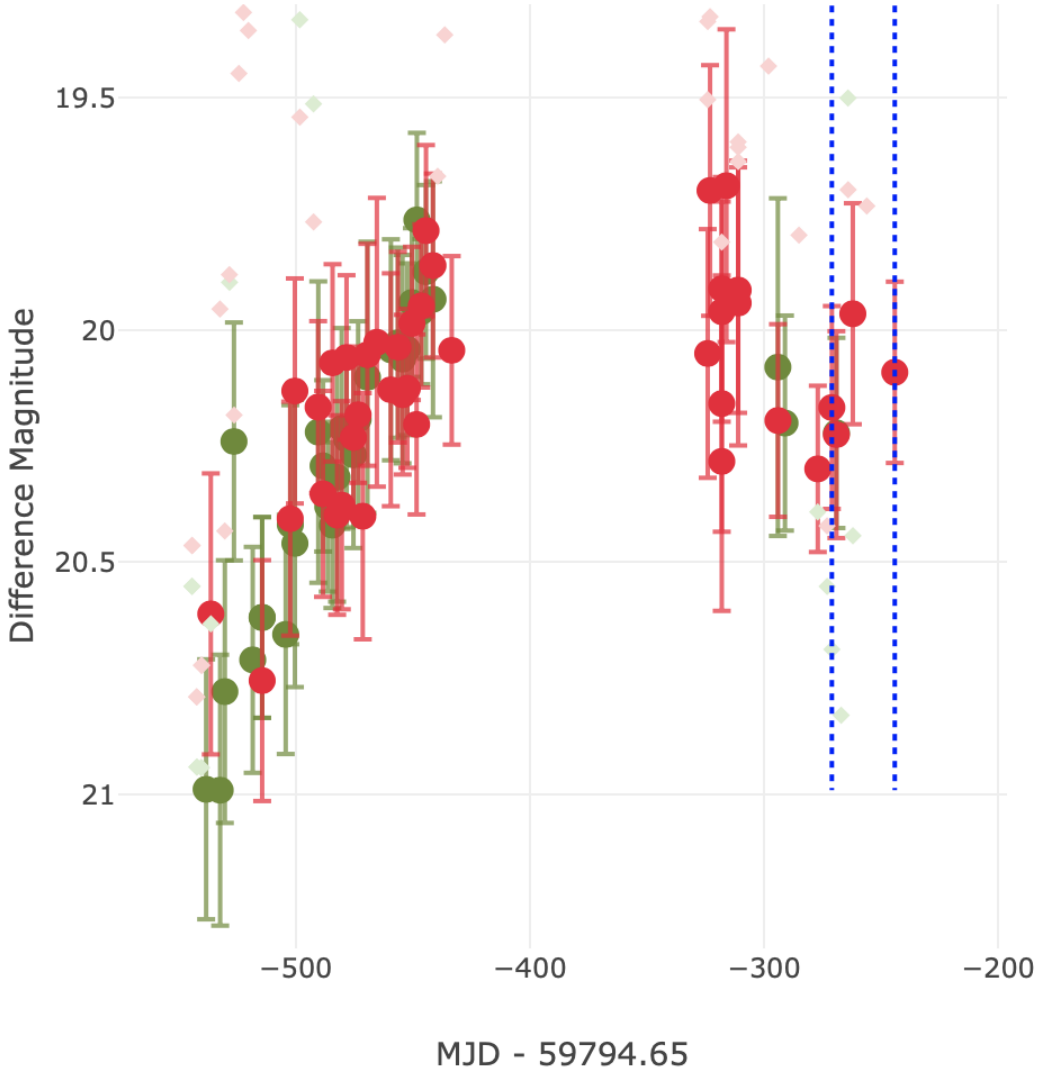

Figure 4.3: The ZTF lightcurve of ZTF21aaoleaj from Lasair. The green and red solid points correspond to g- and r-band measurements, respectively. Transparent diamonds represent the upper limits of non-detections. The difference magnitude on the y-axis is calculated based on difference imaging between the ZTF science and reference images. A clear variation is shown, as the image brightens in both bands before plateauing. There is a period for which no observations were taken for approximately 100 days, but the brightening was observed at a later epoch for an additional period of about 80 days. The variation has not been observed by ZTF since the last detection on 2 Dec 2021, so is presumed to have settled back to its initial quiescent state. Lasair has not noted this variation occurring in any of the other quasar images.

ruled-out ZTF21abqoivk/SN 2021vkz as a lensed SN, and motivated a reconsideration of our observing strategy related to SN-Ia within watchlist cluster galaxies, and led to the more stringent constraints placed for vetting transients near $z \leq 0.16$ clusters described in subsection 4.3.2.

4.4 Search for lensed GWs

During the third observational run (O3) of the LIGO/Virgo detector network during 2019-2020, I was involved in a watchlist-based search for lensed GWs and their KN counterparts. Due to the large sky localisations associated with GW detections ($\gtrsim 100$ sq. deg), it is not feasible to search the entire region for electromagnetic counterparts. However, if the GW is lensed, then the search region is restricted to only those sections of the localisation which are also lensed. Therefore, a valid observing strategy is to target powerful strong lensing clusters within the localisation of candidate lensed GWs as the most efficient way to cover as much of the strong lensing optical depth as possible, in the hope of locating the (lensed) KN counterpart. Detecting a strongly-lensed KN following the GW detection would provide conclusive evidence for the lensing of the GW signal, whilst also localising the GW source with sub-arcsecond precision.

In order to select candidate lensed GWs from the stream of detections with the current available low-latency data, there are two key ingredients. The first is assuming the existence of a neutron star-black hole mass-gap. This is a proposed solution to the apparent lack of observed compact objects between (approximately) 3–5$M_\odot$, by which most formation channels discourage the creation of such objects [199, 200, 201]. If such a gap is assumed to exist, then the detection of a signal with progenitors inferred to exist in the mass-gap can be instead described by a gravitationally-lensed BNS signal, rather than presuming the existence

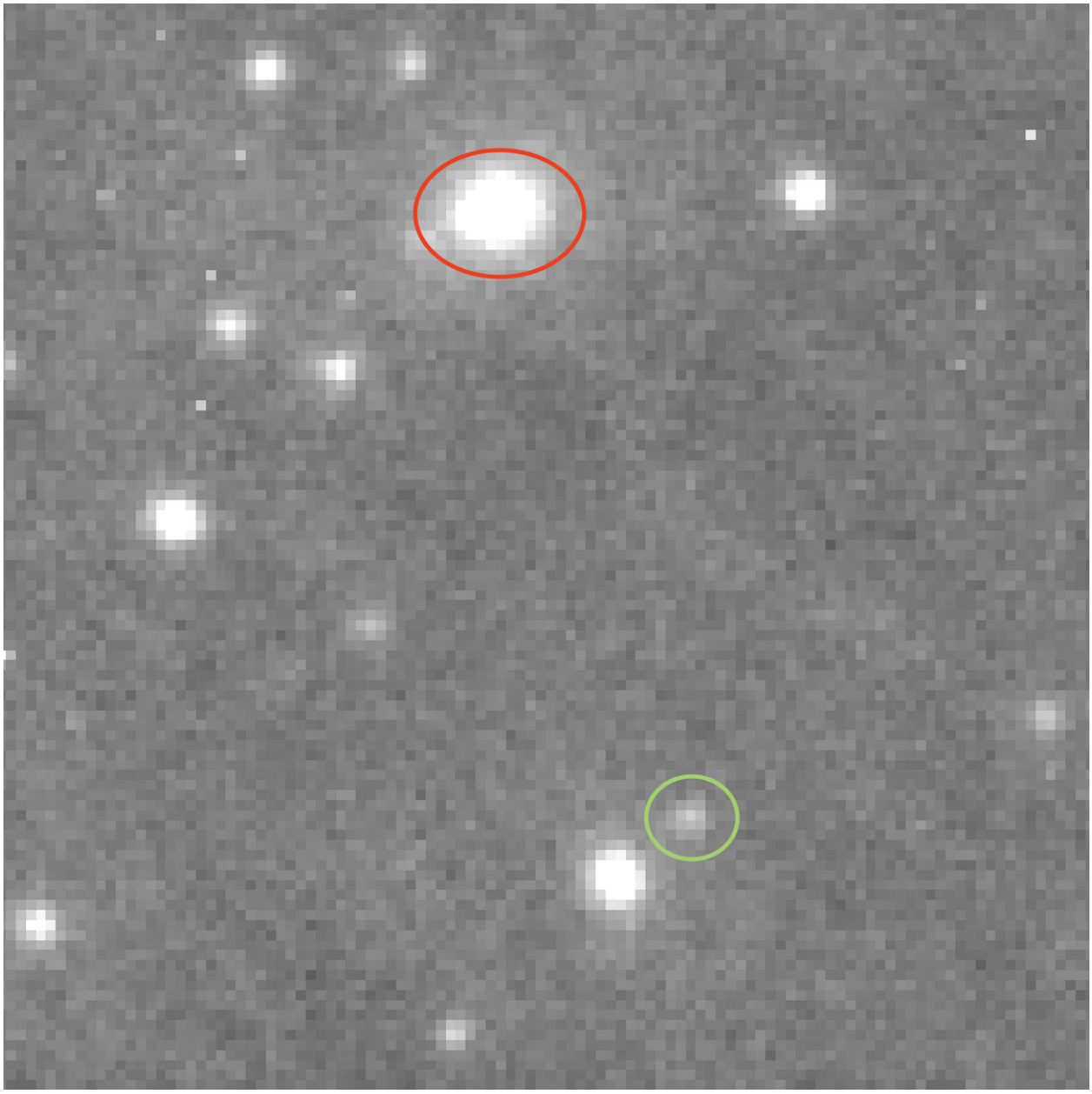

Figure 4.4: Liverpool Telescope r-band image of ZTF21abqoivk/SN 2021vkz. The SN is highlighted by the green ellipse, just to the top-right of its host galaxy, that was initially considered as the potential lens. The red ellipse shows the central galaxy of the galaxy cluster WISEA J230324.99+075643.5, approximately 30 arcsec from the SN. Images were also obtained in g, i and z-bands. The SN colours were consistent with a Type-Ia SN at the cluster redshift, and did not pass our threshold to be a lensed candidate, hence no further follow-up was pursued.

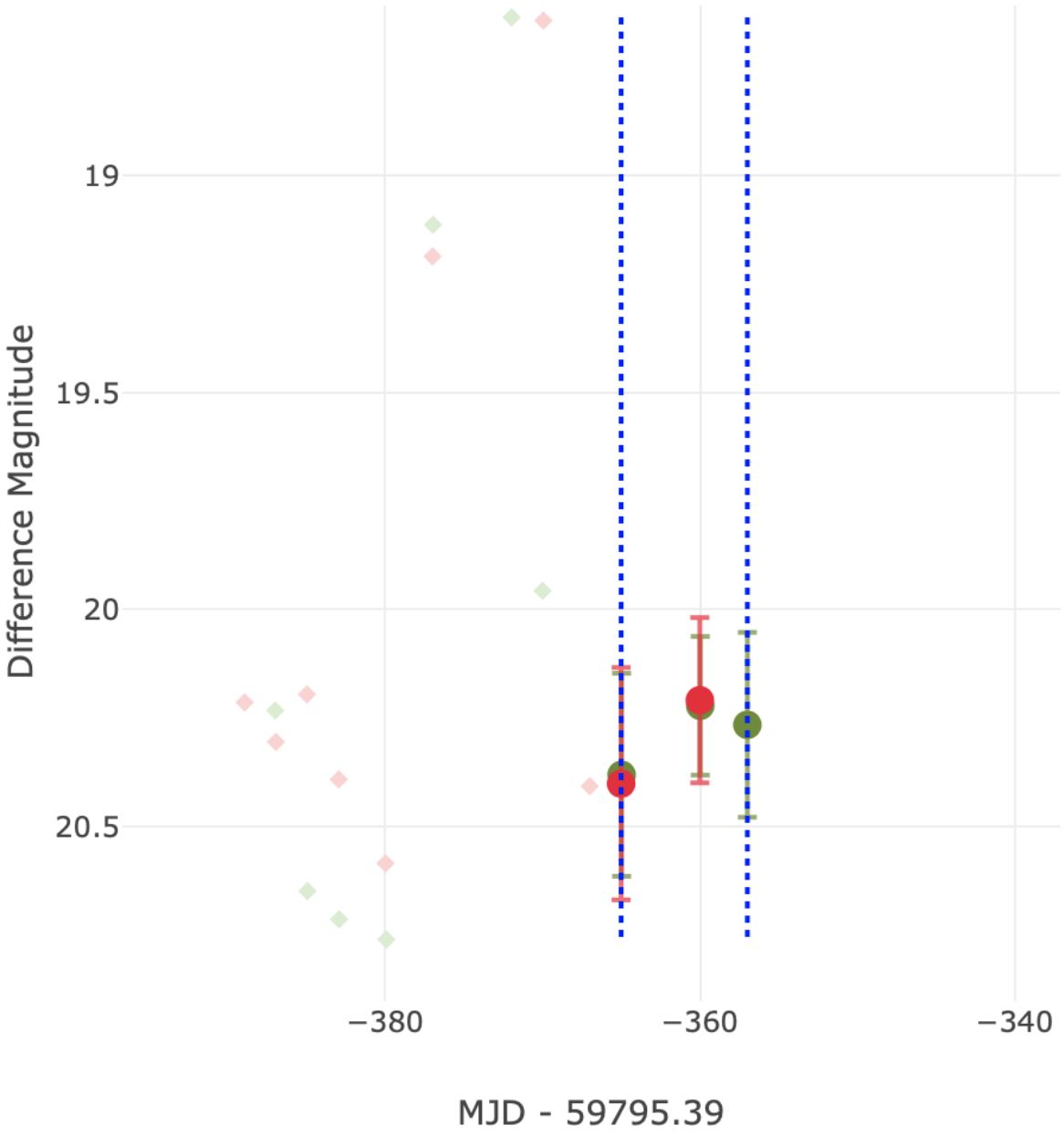

Figure 4.5: The ZTF lightcurve from Lasair for object ZTF21abqoivk/SN 2021vkz. The five data points were obtained in three epochs between 4 and 12 August 2021 in the g- and r-bands (green and red points, respectively). The scarcity of points is due to the SN being only just brighter than the detection limit of ZTF ($5\sigma \sim 20.5$ mag), being detectable only around its peak.

of objects that have not yet been observed. Because the inferred progenitor masses are degenerate with the magnification, and the assumed magnification of any detected GW signal is $\mu = 1$, then the masses of a lensed BNS signal would be overestimated (subsection 1.4.2) and hence can land within the mass-gap. Therefore, any GW signal whose progenitor masses are inferred to be in the mass-gap can be considered a candidate lensed BNS and hence should commence a search for the lensed KN counterpart. However, this requires the masses to be known very shortly after first detection, which leads nicely into the second ingredient that enables us to select candidate lensed GWs: the *low-latency* inference of the masses of the progenitors following a GW detection. Without this, it is not possible to know whether or not the GW is a lensed candidate in time to search for a potential KN counterpart. When a GW detection is made, the BAYESTAR algorithm matches the signal to the best-fitting waveform from a set of GW templates in order to produce an initial skymap and set of binary parameters – including the progenitor masses [202]. This can be completed in seconds following the detection, and is done to provide astronomers with pivotal information as to whether searches for electromagnetic counterparts (lensed or not) should commence, since BBH mergers do not produce EM counterparts. This information is presented as a set of probabilities, each referring to the probability that a particular progenitor type is the true source, and are served to the community through Gamma-ray burst Coordinates Network (GCN) circulars [203].

As already mentioned, the mass-gap probability is the most important of these distributed probabilities for lensed GW searches. However, it is imperative that these probabilities are as robust as possible in low-latency to ensure that observations can take place following true mass-gap candidates, although this is something completely out of our control. There have been cases where, following further higher-latency waveform analyses using more complex and sometimes human-vetted parameter estimation algorithms [204, 205], these probabilities change resulting in events that no longer reside in the mass-gap (e.g. event

S191216ap). However, due to the additional time and resources required to complete these analyses, follow-up observations have already concluded [187]. This highlights one of the risks associated with such a method that relies on the low-latency parameter estimation.

During O3, our group had time on the Gemini telescopes to observe known strong lensing clusters that appear within the sky localisations of high mass-gap probability GW detections, with the goal of detecting a strongly-lensed KN counterpart to the signal [187]. This was carried out in the early stages of the watchlist-based transient searches, and so the list itself was still in its infancy, containing only the initial 130 known strong lensing clusters. In total, three targets were selected and observed: MACS J2135.2-0102 following event S190930s (now GW190930), RX J2129.6+0005 following event S191216ap (now GW191216) and Abell 370 following event S200115j (now GW200115). Whilst no significant candidates were observed, this provided a key opportunity to investigate the possibility of detection. Given that the observations reached a magnitude limit of $\simeq 25.5$ mag, detection of a lensed KN is realistic following predictions from state-of-the-art lightcurve models [206].

4.5 Search for lensed GRBs

Beginning in the summer of 2021, I collaborated with Ben Jones, an undergraduate student, on a project to search for candidate lensed gamma-ray bursts (GRBs) within the archive of detections. The case for GRB lensing is compelling, as many thousands of detections have been made to date, so the probability of at least one detection being strongly lensed is far from insignificant. However, there have been no secure candidate lensed GRBs found to date [121]. This short study cross-referenced our prototype cluster watchlist against the historical catalogue of GRB detections to search for evidence that one of these detections may have been lensed by a galaxy cluster, and was the first lensed GRB search to utilise

objects selected in the lens-plane as a starting point.

For this study, 1414 catalogued GRB detections were taken from those made by the Neil Gehrels *Swift* Observatory's X-Ray Telescope (*Swift*-XRT, [207, 208]) and distributed by the UK Swift Science Data Centre (USSDC, [209, 210]). Thousands more detections exist made by other instruments, such as *Swift's* Burst Alert Telescope (*Swift*-BAT) and the *Fermi* telescope [211], however only those followed up by *Swift*-XRT provide the sub-arcsecond precision required for localising GRBs within the cores of potential lensing clusters. *Swift*-BAT and *Fermi* provide vital steps in the initial localisation of GRBs, but provide square arcminute and square degree precisions respectively, which are too broad for use in this study.

The XRT detections were cross-matched with the positions of all clusters from the prototype watchlist. The closest match (and the only within 1 arcminute of a watchlist cluster) was GRB191101A, separated by 25 arcseconds from the centre of galaxy cluster redMaPPer-28493. An interesting aspect can be also be seen within the lightcurve for the GRB, shown in Figure 4.6. The black data points show data from BAT, and the red from XRT. This shows the initial flare in the BAT data, followed by a secondary peak in the XRT data. One possible interpretation is that this is the same feature repeating following an $\sim$ 100 second time delay caused by gravitational lensing, which would imply a relative magnification between the two burst images. However, this currently remains as hypothesis and requires further analysis in order to be robust, especially since BAT and XRT are each sensitive to different energy ranges of photons.

The candidate lens, galaxy cluster redMaPPer-28493 is fairly sparse – using redMaPPer's richness estimate for the cluster, and cluster scaling relations from [212], we estimate the mass of the cluster as $M_{500} \sim 2 \times 10^{13} \mathrm{M}_{\odot}$. Then, assuming a Navarro-Frenk-White (NFW) profile [147] for the distribution of dark matter within a galaxy cluster, we calculate

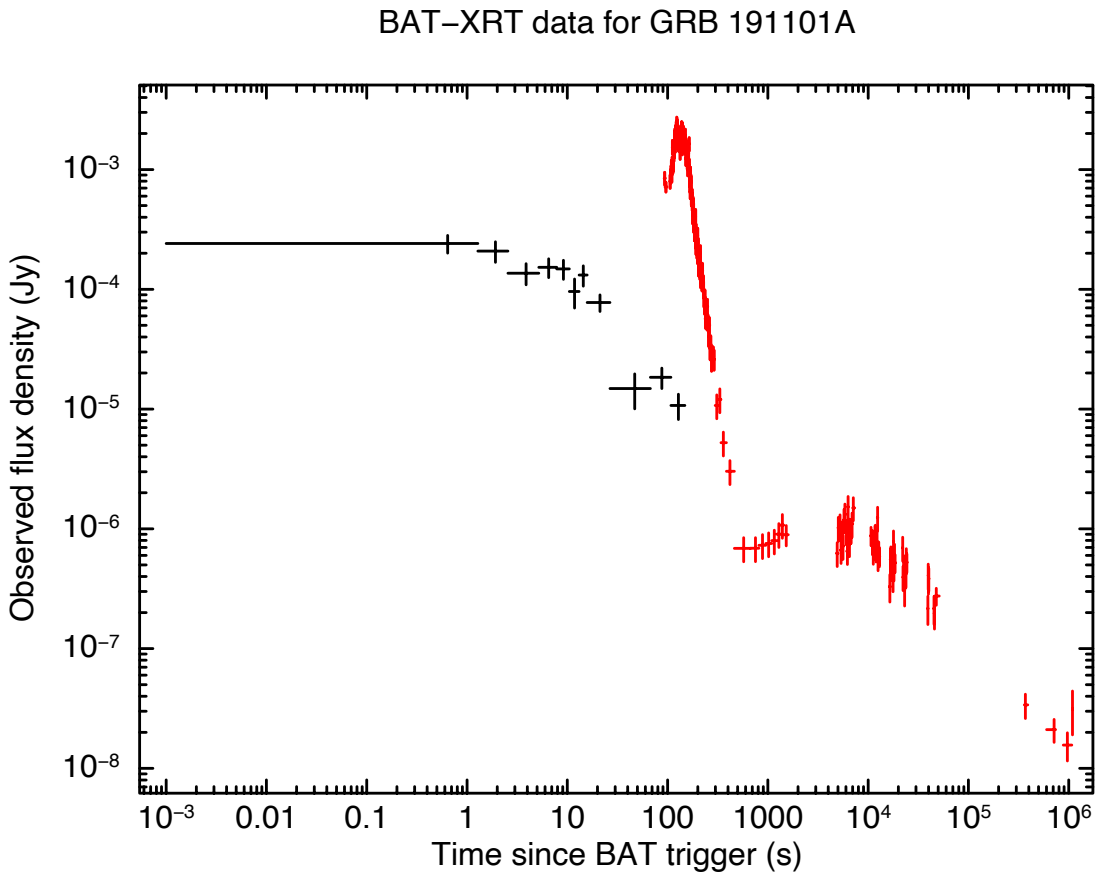

Figure 4.6: Lightcurve for GRB191101A, showing data points collected from the *Swift* telescope – BAT data points are shown in black, XRT data points are shown in red. The presence of a secondary burst at ~ 100 seconds since the initial trigger may be a second image of the initial burst caused by gravitational lensing. Data are obtained from the UK Swift Science Data Centre.

the expected magnification distribution as a function of separation from the centre of the cluster (Figure 4.7). This is calculated for an upper and lower value of c, the NFW concentration parameter, chosen as 2 and 10 respectively – reasonable values that bracket those of observed clusters [213, 148]. The redshift of the GRB is also not known, so a fairly high value of $z_S = 1.5$ is assumed, as a higher source redshift acts to increase the separation at which the high magnifications appear (i.e. increase the radius of the caustics). Therefore, choosing a high z_S is equivalent to placing an upper limit on the separation at which high magnifications occur.

The horizontal dashed black line in Figure 4.7 represents a fairly modest magnification of $\mu = 2$, which even in the case of the most extreme concentration parameter $c = 10$, intersects at only a separation of about 2.5 arcseconds. This means that the contribution of the dark matter component of this galaxy cluster is not significant enough to lens the GRB at a 25 arcsecond separation by any significant amount. Choosing a very extreme source redshift of $z_S = 5$ will only increase this separation to 3 arcseconds, so this result is not significantly changed by assuming a different redshift. Considering only the dark matter/NFW component does not take into account the possibility of a perturbation in the cluster's mass distribution from a member galaxy, which could provide the difference between the signal being lensed or not. However, searching for possible nearby galaxies using NED, and within UHS J-band and WISE $W1$-band imaging uncovers no galaxies nearby the GRB position (see Figure 4.8). Therefore, it seems unlikely that GRB191101A was lensed by any significant amount by the galaxy cluster redMaPPer-28493.

The work carried out for this project has not yet reached its conclusion due to prioritising time on other projects during my PhD. However this work is planned to be submitted for publication in the near future. In addition to the above, we anticipate producing some simple cluster lens models for some of the candidates in order to more robustly constrain the effects that lensing may have had on the respective GRBs.

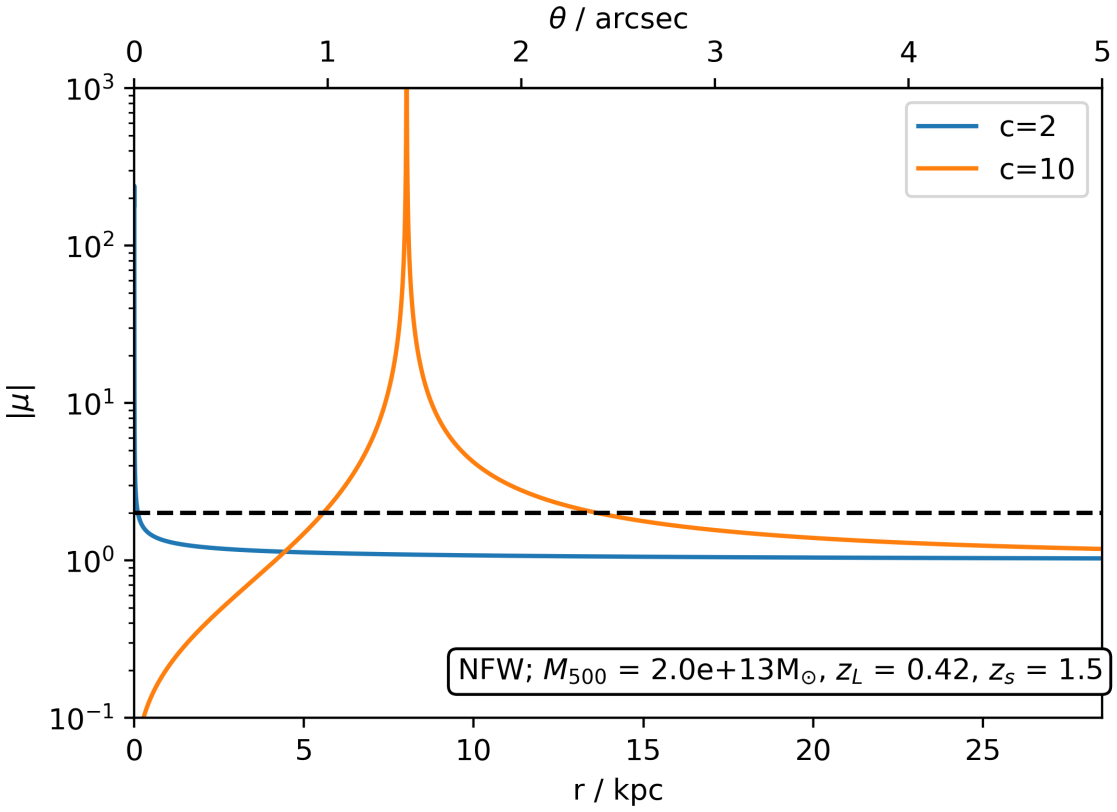

Figure 4.7: Magnification as a function of cluster-centric separation for an NFW dark matter halo of redMaPPer-28493, a cluster within the vicinity of lensed GRB candidate GRB191101A. Upper and lower limits for the concentration parameter, c, are chosen based on observational constraints for clusters [213, 148]. Low values of c require perfect alignment of the source for any significant magnification ($\mu \geq 2$, dashed line), whilst larger values allow a small offset of just above 2 arcseconds. Given the separation of the GRB to redMaPPer-28493 is ~ 25 arcseconds, it is unlikely that the cluster dark matter component provides any significant level of lensing.

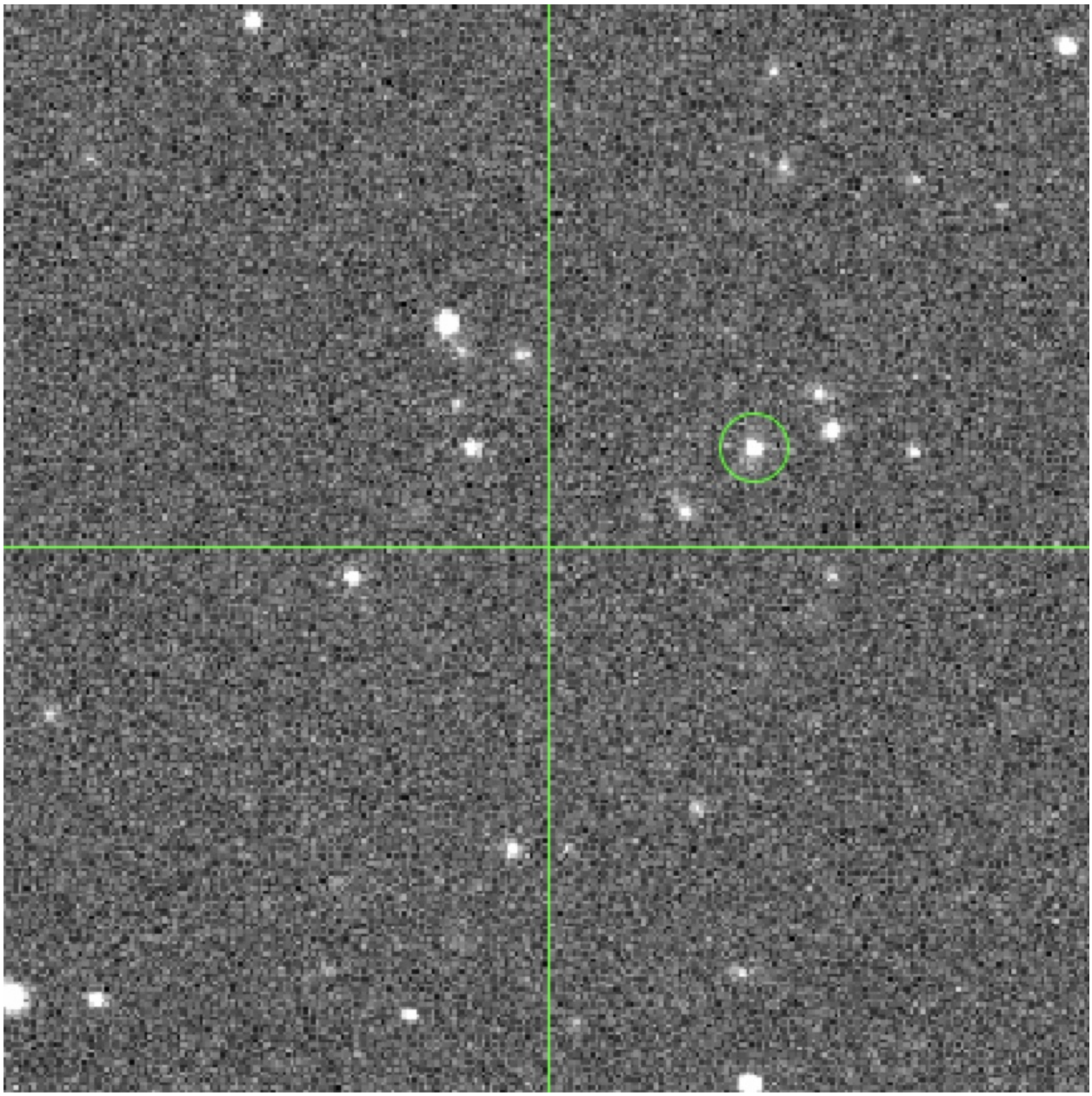

Figure 4.8: UK InfraRed Telescope (UKIRT) J-band image of the region containing GRB191101A. The dimensions of the image are 2x2 arcmin. The location of the GRB is shown at the centre of the crosshair, whilst the central cluster galaxy of redMaPPer-28493 is indicated by the green circle. There are no clear galaxies close to the location of the GRB that can be seen in this image, ruling out the possibility of a prominent cluster member being responsible for gravitationally lensing the GRB.

Chapter 5

Conclusion

In this thesis, I have presented my research into methods for optimising the prospects of detecting strong gravitationally lensed explosive transients, including supernovae, gamma-ray bursts, gravitational waves and kilonovae. In my first paper presented in chapter 2, I showed using a simple and well-defined method that known strong lensing clusters do not make up a significant proportion of clusters that are capable of lensing transient sources, and that a watchlist-based search for lensed transients should instead include as many clusters as possible. In my second paper presented in chapter 3, I describe an all-sky method for locating galaxy clusters up to $z \sim 1$ in order to populate such a watchlist, using only pre-existing survey data. The method was shown to be highly-complete and boasts a low rate of false positive detections during testing. Looking to the future, it is planned to apply this method in order to construct an all-sky watchlist for lensed transient detection, to be completed before the Rubin observatory's Legacy Survey of Space and Time commences operations. Given that the foundations of the method are well established and tested, there is not a large amount of work that remains before this can be done. There is only one main hurdle that remains before this can be completed – this is to streamline the code such that it can

perform the blind search on the entire sky. Until now it has been tested only on specifically chosen and much smaller regions of sky within the wide field survey data. Some code will need to be rewritten to accommodate for this, and some testing will need to be done in order to find the optimal approach – for example, what size of map and tiling strategy should be used. Once complete, we will have access to a catalogue of candidate galaxy clusters ready to be utilised for lensed transient searches, and that can be compared with catalogues assembled by other cluster finding methods. Specifically, we plan to compare the results with optical, x-ray and SZ-effect selected cluster catalogues, such as redMaPPer, CODEX and Planck, respectively. In addition, more sensitive photometry from Rubin will also be usable with this method to find clusters, permitting for discoveries at higher redshifts, and more secure detections at lower redshifts; although some optimisation will likely be required to make the most of the multi-band data. Cluster photometric redshifts from Rubin, and spectroscopic redshifts from cluster observations with the 4MOST instrument will also be central to refining recovery and false positive rate estimates of this method once data become available.

I also presented searches for lensed explosive transients that I have been involved with during my time as a PhD student. These searches utilised the watchlist-based approach that has been the focus of my two first-author papers, and was conducted with a prototype watchlist constructed using galaxy cluster catalogues mostly assembled from known strong lensing clusters and from clusters found by the *Planck* mission and within data from the Sloan Digital Sky Survey. These searches did not result in any significant candidates, however they have demonstrated the principles of operation for such watchlist-focused searches which will be paramount to future programmes looking to detect lensed transients – including with the Rubin observatory.

Bibliography

[1] Scott Dodelson. *Gravitational Lensing*. Cambridge Univ. Press, 2017.

[2] C.S. Kochanek, P. Schneider, and J. Wambsganss. *Gravitational Lensing: Strong, Weak and Micro, Proceedings of the 33rd Saas-Fee Advanced Course*. Ed. by P. Jetzer & P. North G. Meylan. Springer-Verlag: Berlin, 2004.

[3] Jo Bovy. *Dynamics and Astrophysics of Galaxies*. Princeton University Press, In preparation.

[4] F. W. Dyson, A. S. Eddington, and C. Davidson. "A Determination of the Deflection of Light by the Sun's Gravitational Field, from Observations Made at the Total Eclipse of May 29, 1919". In: *Philosophical Transactions of the Royal Society of London Series A* 220 (Jan. 1920), pp. 291–333. DOI: 10.1098/rsta.1920.0009.

[5] Eduardo S. Cypriano et al. "Weak-Lensing Mass Distributions for 24 X-Ray Abell Clusters". In: ApJ 613.1 (Sept. 2004), pp. 95–108. DOI: 10.1086/422896. arXiv: astro-ph/0310009 [astro-ph].

[6] Douglas Clowe, Anthony Gonzalez, and Maxim Markevitch. "Weak-Lensing Mass Reconstruction of the Interacting Cluster 1E 0657-558: Direct Evidence for the Existence of Dark Matter". In: ApJ 604.2 (Apr. 2004), pp. 596–603. DOI: 10.1086/381970. arXiv: astro-ph/0312273 [astro-ph].

[7] Maruša Bradač et al. "Strong and Weak Lensing United. III. Measuring the Mass Distribution of the Merging Galaxy Cluster 1ES 0657-558". In: ApJ 652.2 (Dec. 2006), pp. 937–947. DOI: 10.1086/508601. arXiv: astro-ph/0608408 [astro-ph].

[8] Anja von der Linden et al. "Weighing the Giants - I. Weak-lensing masses for 51 massive galaxy clusters: project overview, data analysis methods and cluster images". In: MNRAS 439.1 (Mar. 2014), pp. 2–27. DOI: 10.1093/mnras/stt1945. arXiv: 1208.0597 [astro-ph.CO].

[9] V. Belokurov et al. "The Cosmic Horseshoe: Discovery of an Einstein Ring around a Giant Luminous Red Galaxy". In: ApJ 671.1 (Dec. 2007), pp. L9–L12. DOI: 10.1086/524948. arXiv: 0706.2326 [astro-ph].

[10] Traci L. Johnson et al. "Lens Models and Magnification Maps of the Six Hubble Frontier Fields Clusters". In: ApJ 797.1, 48 (Dec. 2014), p. 48. DOI: 10.1088/0004-637X/797/1/48. arXiv: 1405.0222 [astro-ph.CO].

[11] Johan Richard et al. "Mass and magnification maps for the Hubble Space Telescope Frontier Fields clusters: implications for high-redshift studies". In: MNRAS 444.1 (Oct. 2014), pp. 268–289. DOI: 10.1093/mnras/stu1395. arXiv: 1405.3303 [astro-ph.CO].

[12] Graham P. Smith et al. "Discovering gravitationally lensed gravitational waves: predicted rates, candidate selection, and localization with the Vera Rubin Observatory". In: *arXiv e-prints*, arXiv:2204.12977 (Apr. 2022), arXiv:2204.12977. arXiv: 2204.12977 [astro-ph.HE].

[13] D. Stern et al. "Gaia GraL: Gaia DR2 Gravitational Lens Systems. VI. Spectroscopic Confirmation and Modeling of Quadruply Imaged Lensed Quasars". In: ApJ 921.1, 42 (Nov. 2021), p. 42. DOI: 10.3847/1538-4357/ac0f04. arXiv: 2012.10051 [astro-ph.GA].

[14] Irwin I. Shapiro. "Fourth Test of General Relativity". In: Phys. Rev. Lett. 13.26 (Dec. 1964), pp. 789–791. DOI: 10.1103/PhysRevLett.13.789.

[15] Adam G. Riess et al. "Large Magellanic Cloud Cepheid Standards Provide a 1% Foundation for the Determination of the Hubble Constant and Stronger Evidence for Physics beyond ΛCDM". In: ApJ 876.1, 85 (May 2019), p. 85. DOI: 10.3847/1538-4357/ab1422. arXiv: 1903.07603 [astro-ph.CO].

[16] Licia Verde, Tommaso Treu, and Adam G. Riess. "Tensions between the early and late Universe". In: *Nature Astronomy* 3 (Sept. 2019), pp. 891–895. DOI: 10.1038/s41550-019-0902-0. arXiv: 1907.10625 [astro-ph.CO].

[17] D. Walsh, R. F. Carswell, and R. J. Weymann. "0957+561 A, B: twin quasistellar objects or gravitational lens?" In: Nature 279 (May 1979), pp. 381–384. DOI: 10.1038/279381a0.

[18] P. Young et al. "The double quasar Q0957+561 A, B: a gravitational lens image formed by a galaxy at z=0.39." In: ApJ 241 (Oct. 1980), pp. 507–520. DOI: 10.1086/158365.

[19] S. Refsdal. "On the possibility of determining Hubble's parameter and the masses of galaxies from the gravitational lens effect". In: MNRAS 128 (Jan. 1964), p. 307. DOI: 10.1093/mnras/128.4.307.

[20] Kenneth C. Wong et al. "H0LiCOW - XIII. A 2.4 per cent measurement of H_0 from lensed quasars: 5.3σ tension between early- and late-Universe probes". In: MNRAS 498.1 (Oct. 2020), pp. 1420–1439. DOI: 10.1093/mnras/stz3094. arXiv: 1907.04869 [astro-ph.CO].

[21] J. Huchra et al. "2237+0305 : a new and unusual gravitational lens." In: AJ 90 (May 1985), pp. 691–696. DOI: 10.1086/113777.

[22] Adam G. Riess et al. “Milky Way Cepheid Standards for Measuring Cosmic Distances and Application to Gaia DR2: Implications for the Hubble Constant”. In: ApJ 861.2, 126 (July 2018), p. 126. DOI: 10.3847/1538-4357/aac82e. arXiv: 1804.10655 [astro-ph.CO].

[23] M. M. Phillips. “The Absolute Magnitudes of Type IA Supernovae”. In: ApJ 413 (Aug. 1993), p. L105. DOI: 10.1086/186970.

[24] G. Soucail et al. “A blue ring-like structure, in the center of the A 370 cluster of galaxies”. In: A&A 172 (Jan. 1987), pp. L14–L16.

[25] Roger Lynds and Vahe Petrosian. “Luminous Arcs in Clusters of Galaxies”. In: ApJ 336 (Jan. 1989), p. 1. DOI: 10.1086/166989.

[26] Y. Mellier et al. “Spectroscopy of the gravitational arcs in CL 2244 - 02, A370 (arclet A5), and CL 0024 + 1654”. In: ApJ 380 (Oct. 1991), pp. 334–343.

[27] M. Franx et al. “A Pair of Lensed Galaxies at z=4.92 in the Field of CL 1358+62”. In: ApJ 486 (Sept. 1997), p. L75.

[28] R. Ellis et al. “A Faint Star-forming System Viewed through the Lensing Cluster Abell 2218: First Light at z˜=5.6?” In: ApJ 560 (Oct. 2001), pp. L119–L122.

[29] E. M. Hu et al. “A Redshift z=6.56 Galaxy behind the Cluster Abell 370”. In: ApJ 568.2 (Apr. 2002), pp. L75–L79. DOI: 10.1086/340424. arXiv: astro-ph/0203091 [astro-ph].

[30] J. Kneib et al. “A Probable z˜7 Galaxy Strongly Lensed by the Rich Cluster A2218: Exploring the Dark Ages”. In: ApJ 607 (June 2004), pp. 697–703.

[31] Keiichi Umetsu et al. “A Precise Cluster Mass Profile Averaged from the Highest-quality Lensing Data”. In: ApJ 738.1, 41 (Sept. 2011), p. 41. DOI: 10.1088/0004-637X/738/1/41. arXiv: 1105.0444 [astro-ph.CO].

[32] G. Soucail et al. “The giant arc in A 370 : spectroscopic evidence for gravitational lensing from a source at Z=0.724.” In: A&A 191 (Feb. 1988), pp. L19–L21.

[33] Masamune Oguri. “Strong gravitational lensing of explosive transients”. In: *Reports on Progress in Physics* 82.12, 126901 (Dec. 2019), p. 126901. DOI: 10.1088/1361-6633/ab4fc5. arXiv: 1907.06830 [astro-ph.CO].

[34] Matt Nicholl. “Superluminous supernovae: an explosive decade”. In: *Astronomy and Geophysics* 62.5 (Oct. 2021), pp. 5.34–5.42. DOI: 10.1093/astrogeo/atab092. arXiv: 2109.08697 [astro-ph.HE].

[35] S. J. Smartt et al. “The death of massive stars - I. Observational constraints on the progenitors of Type II-P supernovae”. In: MNRAS 395.3 (May 2009), pp. 1409–1437. DOI: 10.1111/j.1365-2966.2009.14506.x. arXiv: 0809.0403 [astro-ph].

[36] Weidong Li et al. “Nearby supernova rates from the Lick Observatory Supernova Search - II. The observed luminosity functions and fractions of supernovae in a complete sample”. In: MNRAS 412.3 (Apr. 2011), pp. 1441–1472. DOI: 10.1111/j.1365-2966.2011.18160.x. arXiv: 1006.4612 [astro-ph.SR].

[37] Stephen J. Smartt. “Progenitors of Core-Collapse Supernovae”. In: ARA&A 47.1 (Sept. 2009), pp. 63–106. DOI: 10.1146/annurev-astro-082708-101737. arXiv: 0908.0700 [astro-ph.SR].

[38] A. Ray, K. P. Singh, and F. K. Sutaria. “The bolometric light curve of SN 1993J and the nature of its progenitor.” In: *Journal of Astrophysics and Astronomy* 14 (June 1993), pp. 53–63. DOI: 10.1007/BF02702248.

[39] George Sonneborn, Bruce Altner, and Robert P. Kirshner. “The Progenitor of SN 1987A: Spatially Resolved Ultraviolet Spectroscopy of the Supernova Field”. In: ApJ 323 (Dec. 1987), p. L35. DOI: 10.1086/185052.

[40] N. Panagia. "SN 1987A: The Unusual Explosion of a Normal Type II Supernova". In: *1604-2004: Supernovae as Cosmological Lighthouses*. Ed. by M. Turatto et al. Vol. 342. Astronomical Society of the Pacific Conference Series. Dec. 2005, p. 78. arXiv: astro-ph/0410275 [astro-ph].

[41] Chryssa Kouveliotou et al. "Identification of Two Classes of Gamma-Ray Bursts". In: ApJ 413 (Aug. 1993), p. L101. DOI: 10.1086/186969.

[42] Edo Berger. "Short-Duration Gamma-Ray Bursts". In: ARA&A 52 (Aug. 2014), pp. 43–105. DOI: 10.1146/annurev-astro-081913-035926. arXiv: 1311.2603 [astro-ph.HE].

[43] Ray W. Klebesadel, Ian B. Strong, and Roy A. Olson. "Observations of Gamma-Ray Bursts of Cosmic Origin". In: ApJ 182 (June 1973), p. L85. DOI: 10.1086/181225.

[44] Gerald J. Fishman and Charles A. Meegan. "Gamma-Ray Bursts". In: ARA&A 33 (Jan. 1995), pp. 415–458. DOI: 10.1146/annurev.aa.33.090195.002215.

[45] James E. Rhoads. "How to Tell a Jet from a Balloon: A Proposed Test for Beaming in Gamma-Ray Bursts". In: ApJ 487.1 (Sept. 1997), pp. L1–L4. DOI: 10.1086/310876. arXiv: astro-ph/9705163 [astro-ph].

[46] S. E. Woosley and J. S. Bloom. "The Supernova Gamma-Ray Burst Connection". In: ARA&A 44.1 (Sept. 2006), pp. 507–556. DOI: 10.1146/annurev.astro.43.072103.150558. arXiv: astro-ph/0609142 [astro-ph].

[47] D. Lazzati, E. Ramirez-Ruiz, and G. Ghisellini. "Possible detection of hard X-ray afterglows of short gamma -ray bursts". In: A&A 379 (Dec. 2001), pp. L39–L43. DOI: 10.1051/0004-6361:20011485. arXiv: astro-ph/0110215 [astro-ph].

[48] N. Gehrels et al. "A new γ-ray burst classification scheme from GRB060614". In: Nature 444.7122 (Dec. 2006), pp. 1044–1046. DOI: 10.1038/nature05376. arXiv: astro-ph/0610635 [astro-ph].

[49] J. M. Weisberg and J. H. Taylor. "The Relativistic Binary Pulsar B1913+16: Thirty Years of Observations and Analysis". In: *Binary Radio Pulsars*. Ed. by Fred A. Rasio and Ingrid H. Stairs. Vol. 328. Astronomical Society of the Pacific Conference Series. 2005, p. 25. arXiv: astro-ph/0407149 [astro-ph].

[50] B. P. Abbott et al. "Observation of Gravitational Waves from a Binary Black Hole Merger". In: Phys. Rev. Lett. 116.6, 061102 (2016), p. 061102. DOI: 10.1103/PhysRevLett.116.061102. arXiv: 1602.03837 [gr-qc].

[51] Curt Cutler and Kip S. Thorne. "An Overview of Gravitational-Wave Sources". In: *arXiv e-prints*, gr-qc/0204090 (2002), gr–qc/0204090. arXiv: gr-qc/0204090 [gr-qc].

[52] B. P. Abbott et al. "LIGO: the Laser Interferometer Gravitational-Wave Observatory". In: *Reports on Progress in Physics* 72.7, 076901 (2009), p. 076901. DOI: 10.1088/0034-4885/72/7/076901. arXiv: 0711.3041 [gr-qc].

[53] The LIGO Scientific Collaboration et al. "GWTC-3: Compact Binary Coalescences Observed by LIGO and Virgo During the Second Part of the Third Observing Run". In: *arXiv e-prints*, arXiv:2111.03606 (Nov. 2021), arXiv:2111.03606. arXiv: 2111.03606 [gr-qc].

[54] B. F. Schutz. "Determining the Hubble constant from gravitational wave observations". In: Nature 323.6086 (1986), pp. 310–311. DOI: 10.1038/323310a0.

[55] B. P. Abbott et al. "Tests of General Relativity with GW150914". In: Phys. Rev. Lett. 116.22, 221101 (2016), p. 221101. DOI: 10.1103/PhysRevLett.116.221101. arXiv: 1602.03841 [gr-qc].

[56] M. J. Graham et al. "Candidate Electromagnetic Counterpart to the Binary Black Hole Merger Gravitational-Wave Event S190521g*". In: Phys. Rev. Lett. 124.25,

251102 (June 2020), p. 251102. DOI: 10.1103/PhysRevLett.124.251102. arXiv: 2006.14122 [astro-ph.HE].

[57] A. von Kienlin et al. "The Fourth Fermi-GBM Gamma-Ray Burst Catalog: A Decade of Data". In: ApJ 893.1, 46 (Apr. 2020), p. 46. DOI: 10.3847/1538-4357/ab7a18. arXiv: 2002.11460 [astro-ph.HE].

[58] D. B. Fox et al. "The afterglow of GRB 050709 and the nature of the short-hard γ-ray bursts". In: Nature 437.7060 (Oct. 2005), pp. 845–850. DOI: 10.1038/nature04189. arXiv: astro-ph/0510110 [astro-ph].

[59] Iair Arcavi et al. "Optical emission from a kilonova following a gravitational-wave-detected neutron-star merger". In: Nature 551.7678 (Nov. 2017), pp. 64–66. DOI: 10.1038/nature24291. arXiv: 1710.05843 [astro-ph.HE].

[60] G. P. Lamb et al. "Short GRB 160821B: A Reverse Shock, a Refreshed Shock, and a Well-sampled Kilonova". In: ApJ 883.1, 48 (Sept. 2019), p. 48. DOI: 10.3847/1538-4357/ab38bb. arXiv: 1905.02159 [astro-ph.HE].

[61] W. Fong et al. "The Broadband Counterpart of the Short GRB 200522A at z = 0.5536: A Luminous Kilonova or a Collimated Outflow with a Reverse Shock?" In: ApJ 906.2, 127 (Jan. 2021), p. 127. DOI: 10.3847/1538-4357/abc74a. arXiv: 2008.08593 [astro-ph.HE].

[62] B. O'Connor et al. "A tale of two mergers: constraints on kilonova detection in two short GRBs at z $\sim$ 0.5". In: MNRAS 502.1 (Mar. 2021), pp. 1279–1298. DOI: 10.1093/mnras/stab132. arXiv: 2012.00026 [astro-ph.HE].

[63] J. C. Rastinejad et al. "A Kilonova Following a Long-Duration Gamma-Ray Burst at 350 Mpc". In: *arXiv e-prints*, arXiv:2204.10864 (Apr. 2022), arXiv:2204.10864. arXiv: 2204.10864 [astro-ph.HE].

[64] B. P. Abbott et al. "GWTC-1: A Gravitational-Wave Transient Catalog of Compact Binary Mergers Observed by LIGO and Virgo during the First and Second Observing Runs". In: *Physical Review X* 9.3, 031040 (July 2019), p. 031040. DOI: 10.1103/PhysRevX.9.031040. arXiv: 1811.12907 [astro-ph.HE].

[65] The LIGO Scientific Collaboration et al. "GWTC-3: Compact Binary Coalescences Observed by LIGO and Virgo During the Second Part of the Third Observing Run". In: *arXiv e-prints*, arXiv:2111.03606 (Nov. 2021), arXiv:2111.03606. arXiv: 2111.03606 [gr-qc].

[66] J. Veitch et al. "Estimating parameters of coalescing compact binaries with proposed advanced detector networks". In: *Phys. Rev. D* 85 (10 2012), p. 104045. DOI: 10.1103/PhysRevD.85.104045. URL: https://link.aps.org/doi/10.1103/PhysRevD.85.104045.

[67] V. A. Villar et al. "The Combined Ultraviolet, Optical, and Near-infrared Light Curves of the Kilonova Associated with the Binary Neutron Star Merger GW170817: Unified Data Set, Analytic Models, and Physical Implications". In: ApJ 851.1, L21 (Dec. 2017), p. L21. DOI: 10.3847/2041-8213/aa9c84. arXiv: 1710.11576 [astro-ph.HE].

[68] Masamune Oguri and Yozo Kawano. "Gravitational lens time delays for distant supernovae: breaking the degeneracy between radial mass profiles and the Hubble constant". In: MNRAS 338.4 (Feb. 2003), pp. L25–L29. DOI: 10.1046/j.1365-8711.2003.06290.x. arXiv: astro-ph/0211499 [astro-ph].

[69] Daniel E. Holz. "Seeing Double: Strong Gravitational Lensing of High-Redshift Supernovae". In: ApJ 556.2 (Aug. 2001), pp. L71–L74. DOI: 10.1086/322947. arXiv: astro-ph/0104440 [astro-ph].

[70] A. Goobar et al. "iPTF16geu: A multiply imaged, gravitationally lensed type Ia supernova". In: *Science* 356.6335 (Apr. 2017), pp. 291–295. DOI: 10.1126/science.aal2729. arXiv: 1611.00014 [astro-ph.CO].

[71] Akın Yıldırım, Sherry H. Suyu, and Aleksi Halkola. "Time-delay cosmographic forecasts with strong lensing and JWST stellar kinematics". In: MNRAS 493.4 (Apr. 2020), pp. 4783–4807. DOI: 10.1093/mnras/staa498. arXiv: 1904.07237 [astro-ph.CO].

[72] Daniel A. Goldstein et al. "Precise Time Delays from Strongly Gravitationally Lensed Type Ia Supernovae with Chromatically Microlensed Images". In: ApJ 855.1, 22 (Mar. 2018), p. 22. DOI: 10.3847/1538-4357/aaa975. arXiv: 1708.00003 [astro-ph.CO].

[73] Edvard Mörtsell and Christoffer Sunesson. "Strong lensing, cosmology and lensing halos". In: J. Cosmology Astropart. Phys. 2006.1, 012 (Jan. 2006), p. 012. DOI: 10.1088/1475-7516/2006/01/012. arXiv: astro-ph/0510120 [astro-ph].

[74] Kai Liao et al. "Precision cosmology from future lensed gravitational wave and electromagnetic signals". In: *Nature Communications* 8, 1148 (Oct. 2017), p. 1148. DOI: 10.1038/s41467-017-01152-9. arXiv: 1703.04151 [astro-ph.CO].

[75] S. H. Suyu et al. "Two Accurate Time-delay Distances from Strong Lensing: Implications for Cosmology". In: ApJ 766.2, 70 (Apr. 2013), p. 70. DOI: 10.1088/0004-637X/766/2/70. arXiv: 1208.6010 [astro-ph.CO].

[76] S. H. Suyu et al. "H0LiCOW - I. H_0 Lenses in COSMOGRAIL's Wellspring: program overview". In: MNRAS 468.3 (2017), pp. 2590–2604. DOI: 10.1093/mnras/stx483. arXiv: 1607.00017 [astro-ph.CO].

[77] Peter Schneider and Dominique Sluse. "Mass-sheet degeneracy, power-law models and external convergence: Impact on the determination of the Hubble constant from gravitational lensing". In: A&A 559, A37 (Nov. 2013), A37. DOI: 10.1051/0004-6361/201321882. arXiv: 1306.0901 [astro-ph.CO].

[78] A. Krolak and Bernard F. Schutz. "Coalescing binaries—Probe of the universe". In: *General Relativity and Gravitation* 19.12 (Dec. 1987), pp. 1163–1171. DOI: 10.1007/BF00759095.

[79] Yudai Suwa. "Supernova forecast with strong lensing". In: MNRAS 474.2 (Feb. 2018), pp. 2612–2616. DOI: 10.1093/mnras/stx2953. arXiv: 1711.00183 [astro-ph.HE].

[80] Eli Waxman and Boaz Katz. "Shock Breakout Theory". In: *Handbook of Supernovae*. Ed. by Athem W. Alsabti and Paul Murdin. 2017, p. 967. DOI: 10.1007/978-3-319-21846-5_33.

[81] Andrew Robertson et al. "What does strong gravitational lensing? The mass and redshift distribution of high-magnification lenses". In: *arXiv e-prints*, arXiv:2002.01479 (Feb. 2020), arXiv:2002.01479. arXiv: 2002.01479 [astro-ph.CO].

[82] Daniel E. Holz, M. Coleman Miller, and Jean M. Quashnock. "Gravitational Lensing Limits on the Average Redshift of Gamma-Ray Bursts". In: ApJ 510.1 (Jan. 1999), pp. 54–63. DOI: 10.1086/306568. arXiv: astro-ph/9804271 [astro-ph].

[83] ChunYu Li and LiXin Li. "Constraining fast radio burst progenitors with gravitational lensing". In: *Science China Physics, Mechanics, and Astronomy* 57.7 (July 2014), pp. 1390–1394. DOI: 10.1007/s11433-014-5465-6. arXiv: 1403.7873 [astro-ph.HE].

[84] E. Bellm. "The Zwicky Transient Facility". In: *The Third Hot-wiring the Transient Universe Workshop*. Ed. by P. R. Wozniak et al. 2014, pp. 27–33. arXiv: 1410.8185 [astro-ph.IM].

[85] LSST Science Collaboration et al. "LSST Science Book, Version 2.0". In: *arXiv e-prints*, arXiv:0912.0201 (2009), arXiv:0912.0201. arXiv: 0912.0201 [astro-ph.IM].

[86] Masamune Oguri. "The Mass Distribution of SDSS J1004+4112 Revisited". In: PASJ 62 (Aug. 2010), p. 1017. DOI: 10.1093/pasj/62.4.1017. arXiv: 1005.3103 [astro-ph.CO].

[87] Daniel A. Goldstein, Peter E. Nugent, and Ariel Goobar. "Rates and Properties of Supernovae Strongly Gravitationally Lensed by Elliptical Galaxies in Time-domain

Imaging Surveys". In: ApJS 243.1, 6 (2019), p. 6. DOI: 10.3847/1538-4365/ab1fe0. arXiv: 1809.10147 [astro-ph.GA].

[88] Graham P. Smith et al. "Discovery of Strongly-lensed Gravitational Waves - Implications for the LSST Observing Strategy". In: *arXiv e-prints*, arXiv:1902.05140 (Feb. 2019), arXiv:1902.05140. arXiv: 1902.05140 [astro-ph.HE].

[89] O. A. Hannuksela et al. "Search for Gravitational Lensing Signatures in LIGO-Virgo Binary Black Hole Events". In: ApJ 874.1, L2 (2019), p. L2. DOI: 10.3847/2041-8213/ab0c0f. arXiv: 1901.02674 [gr-qc].

[90] Liang Dai et al. "Search for Lensed Gravitational Waves Including Morse Phase Information: An Intriguing Candidate in O2". In: *arXiv e-prints*, arXiv:2007.12709 (July 2020), arXiv:2007.12709. arXiv: 2007.12709 [astro-ph.HE].

[91] Xiaoshu Liu, Ignacio Magaña Hernandez, and Jolien Creighton. "Identifying Strong Gravitational-wave Lensing during the Second Observing Run of Advanced LIGO and Advanced Virgo". In: ApJ 908.1, 97 (Feb. 2021), p. 97. DOI: 10.3847/1538-4357/abd7eb. arXiv: 2009.06539 [astro-ph.HE].

[92] Alvin K. Y. Li et al. "Finding diamonds in the rough: Targeted Sub-threshold Search for Strongly-lensed Gravitational-wave Events". In: *arXiv e-prints*, arXiv:1904.06020 (Apr. 2019), arXiv:1904.06020. arXiv: 1904.06020 [gr-qc].

[93] Connor McIsaac et al. "Search for strongly lensed counterpart images of binary black hole mergers in the first two LIGO observing runs". In: Phys. Rev. D 102.8, 084031 (Oct. 2020), p. 084031. DOI: 10.1103/PhysRevD.102.084031. arXiv: 1912.05389 [gr-qc].

[94] R. Abbott et al. "Search for Lensing Signatures in the Gravitational-Wave Observations from the First Half of LIGO-Virgo's Third Observing Run". In: ApJ 923.1, 14 (Dec. 2021), p. 14. DOI: 10.3847/1538-4357/ac23db. arXiv: 2105.06384 [gr-qc].

[95] Peter T. H. Pang et al. "Lensed or not lensed: determining lensing magnifications for binary neutron star mergers from a single detection". In: MNRAS 495.4 (July 2020), pp. 3740–3750. DOI: 10.1093/mnras/staa1430. arXiv: 2002.04893 [astro-ph.HE].

[96] A. A. Abdo et al. "A limit on the variation of the speed of light arising from quantum gravity effects". In: Nature 462.7271 (Nov. 2009), pp. 331–334. DOI: 10.1038/nature08574. arXiv: 0908.1832 [astro-ph.HE].

[97] Thomas E. Collett and David Bacon. "Testing the Speed of Gravitational Waves over Cosmological Distances with Strong Gravitational Lensing". In: Phys. Rev. Lett. 118.9, 091101 (Mar. 2017), p. 091101. DOI: 10.1103/PhysRevLett.118.091101. arXiv: 1602.05882 [astro-ph.HE].

[98] K. C. Chambers et al. "The Pan-STARRS1 Surveys". In: *arXiv e-prints*, arXiv:1612.05560 (Dec. 2016), arXiv:1612.05560. arXiv: 1612.05560 [astro-ph.IM].

[99] R. Chornock et al. "PS1-10afx at z = 1.388: Pan-STARRS1 Discovery of a New Type of Superluminous Supernova". In: ApJ 767.2, 162 (Apr. 2013), p. 162. DOI: 10.1088/0004-637X/767/2/162. arXiv: 1302.0009 [astro-ph.CO].

[100] Robert M. Quimby et al. "Extraordinary Magnification of the Ordinary Type Ia Supernova PS1-10afx". In: ApJ 768.1, L20 (May 2013), p. L20. DOI: 10.1088/2041-8205/768/1/L20. arXiv: 1302.2785 [astro-ph.CO].

[101] Robert M. Quimby et al. "Detection of the Gravitational Lens Magnifying a Type Ia Supernova". In: *Science* 344.6182 (Apr. 2014), pp. 396–399. DOI: 10.1126/science.1250903. arXiv: 1404.6014 [astro-ph.CO].

[102] Patrick L. Kelly et al. "Multiple images of a highly magnified supernova formed by an early-type cluster galaxy lens". In: *Science* 347.6226 (2015), pp. 1123–1126. DOI: 10.1126/science.aaa3350. arXiv: 1411.6009 [astro-ph.CO].

[103] P. L. Kelly et al. "SN Refsdal: Classification as a Luminous and Blue SN 1987A-like Type II Supernova". In: ApJ 831.2, 205 (Nov. 2016), p. 205. DOI: 10.3847/0004-637X/831/2/205. arXiv: 1512.09093 [astro-ph.GA].

[104] M. Oguri. "Predicted properties of multiple images of the strongly lensed supernova SN Refsdal." In: MNRAS 449 (Apr. 2015), pp. L86–L89. DOI: 10.1093/mnrasl/slv025. arXiv: 1411.6443 [astro-ph.CO].

[105] Keren Sharon and Traci L. Johnson. "Revised Lens Model for the Multiply Imaged Lensed Supernova, "SN Refsdal" in MACS J1149+2223". In: ApJ 800.2, L26 (Feb. 2015), p. L26. DOI: 10.1088/2041-8205/800/2/L26. arXiv: 1411.6933 [astro-ph.CO].

[106] Jose M. Diego et al. "A free-form prediction for the reappearance of supernova Refsdal in the Hubble Frontier Fields cluster MACSJ1149.5+2223". In: MNRAS 456.1 (Feb. 2016), pp. 356–365. DOI: 10.1093/mnras/stv2638. arXiv: 1504.05953 [astro-ph.CO].

[107] M. Jauzac et al. "Hubble Frontier Fields: predictions for the return of SN Refsdal with the MUSE and GMOS spectrographs". In: MNRAS 457.2 (Apr. 2016), pp. 2029–2042. DOI: 10.1093/mnras/stw069. arXiv: 1509.08914 [astro-ph.GA].

[108] T. Treu et al. ""Refsdal" Meets Popper: Comparing Predictions of the Re-appearance of the Multiply Imaged Supernova Behind MACSJ1149.5+2223". In: ApJ 817.1, 60 (Jan. 2016), p. 60. DOI: 10.3847/0004-637X/817/1/60. arXiv: 1510.05750 [astro-ph.CO].

[109] Graham P. Smith et al. "Hubble Space Telescope Observations of a Spectacular New Strong-Lensing Galaxy Cluster: MACS J1149.5+2223 at z = 0.544". In: ApJ 707.2 (Dec. 2009), pp. L163–L168. DOI: 10.1088/0004-637X/707/2/L163. arXiv: 0911.2003 [astro-ph.CO].

[110] P. L. Kelly et al. "Deja Vu All Over Again: The Reappearance of Supernova Refsdal". In: ApJ 819.1, L8 (Mar. 2016), p. L8. DOI: 10.3847/2041-8205/819/1/L8. arXiv: 1512.04654 [astro-ph.CO].

[111] J. Vega-Ferrero et al. "The Hubble Constant from SN Refsdal". In: ApJ 853.2, L31 (Feb. 2018), p. L31. DOI: 10.3847/2041-8213/aaa95f. arXiv: 1712.05800 [astro-ph.CO].

[112] Yi Cao, Peter E. Nugent, and Mansi M. Kasliwal. "Intermediate Palomar Transient Factory: Realtime Image Subtraction Pipeline". In: PASP 128.969 (Nov. 2016), p. 114502. DOI: 10.1088/1538-3873/128/969/114502. arXiv: 1608.01006 [astro-ph.IM].

[113] Steven A. Rodney et al. "A gravitationally lensed supernova with an observable two-decade time delay". In: *Nature Astronomy* 5 (Sept. 2021), pp. 1118–1125. DOI: 10.1038/s41550-021-01450-9. arXiv: 2106.08935 [astro-ph.CO].

[114] J. A. Muñoz et al. "The Longest Delay". In: *arXiv e-prints*, arXiv:2206.08597 (June 2022), arXiv:2206.08597. arXiv: 2206.08597 [astro-ph.GA].

[115] A. Goobar et al. "Near-IR search for lensed supernovae behind galaxy clusters. II. First detection and future prospects". In: A&A 507.1 (2009), pp. 71–83. DOI: 10.1051/0004-6361/200811254. arXiv: 0810.4932 [astro-ph].

[116] R. Amanullah et al. "A Highly Magnified Supernova at z = 1.703 behind the Massive Galaxy Cluster A1689". In: ApJ 742.1, L7 (Nov. 2011), p. L7. DOI: 10.1088/2041-8205/742/1/L7. arXiv: 1109.4740 [astro-ph.CO].

[117] Brandon Patel et al. "Three Gravitationally Lensed Supernovae behind CLASH Galaxy Clusters". In: ApJ 786.1, 9 (May 2014), p. 9. DOI: 10.1088/0004-637X/786/1/9. arXiv: 1312.0943 [astro-ph.CO].

[118] Steven A. Rodney et al. "Illuminating a Dark Lens : A Type Ia Supernova Magnified by the Frontier Fields Galaxy Cluster Abell 2744". In: ApJ 811.1, 70 (Sept. 2015), p. 70. DOI: 10.1088/0004-637X/811/1/70. arXiv: 1505.06211 [astro-ph.CO].

[119] D. Rubin et al. "The Discovery of a Gravitationally Lensed Supernova Ia at Redshift 2.22". In: ApJ 866.1, 65 (2018), p. 65. DOI: 10.3847/1538-4357/aad565. arXiv: 1707.04606 [astro-ph.GA].

[120] Björn Ahlgren and Josefin Larsson. "A Search for Lensed Gamma-Ray Bursts in 11 yr of Observations by Fermi GBM". In: ApJ 897.2, 178 (July 2020), p. 178. DOI: 10.3847/1538-4357/ab9b8a. arXiv: 2006.07095 [astro-ph.HE].

[121] P. Veres et al. "Fermi-GBM Observations of GRB 210812A: Signatures of a Million Solar Mass Gravitational Lens". In: ApJ 921.2, L30 (Nov. 2021), p. L30. DOI: 10.3847/2041-8213/ac2ee6. arXiv: 2110.06065 [astro-ph.HE].

[122] Graham P. Smith et al. "What if LIGO's gravitational wave detections are strongly lensed by massive galaxy clusters?" In: MNRAS 475.3 (2018), pp. 3823–3828. DOI: 10.1093/mnras/sty031. arXiv: 1707.03412 [astro-ph.HE].

[123] G. P. Smith et al. "Deep and rapid observations of strong-lensing galaxy clusters within the sky localization of GW170814". In: MNRAS 485.4 (2019), pp. 5180–5191. DOI: 10.1093/mnras/stz675. arXiv: 1805.07370 [astro-ph.HE].

[124] Dan Ryczanowski et al. "On building a cluster watchlist for identifying strongly lensed supernovae, gravitational waves and kilonovae". In: MNRAS 495.2 (June 2020), pp. 1666–1671. DOI: 10.1093/mnras/staa1274. arXiv: 2005.02296 [astro-ph.GA].

[125] The GOTO Collaboration. *"The Gravitational-wave Optical Transient Observer"*. Accessed: 2019-10-04. 2016. URL: https://goto-observatory.org.

[126] Daniel A. Goldstein and Peter E. Nugent. "How to Find Gravitationally Lensed Type Ia Supernovae". In: ApJ 834.1, L5 (2017), p. L5. DOI: 10.3847/2041-8213/834/1/L5. arXiv: 1611.09459 [astro-ph.IM].

[127] Masamune Oguri and Philip J. Marshall. "Gravitationally lensed quasars and supernovae in future wide-field optical imaging surveys". In: MNRAS 405.4 (2010), pp. 2579–2593. DOI: 10.1111/j.1365-2966.2010.16639.x. arXiv: 1001.2037 [astro-ph.CO].

[128] Ken K. Y. Ng et al. "Precise LIGO lensing rate predictions for binary black holes". In: Phys. Rev. D 97.2, 023012 (2018), p. 023012. DOI: 10.1103/PhysRevD.97.023012. arXiv: 1703.06319 [astro-ph.CO].

[129] Shun-Sheng Li et al. "Gravitational lensing of gravitational waves: a statistical perspective". In: MNRAS 476.2 (2018), pp. 2220–2229. DOI: 10.1093/mnras/sty411. arXiv: 1802.05089 [astro-ph.CO].

[130] Leo P. Singer, Daniel A. Goldstein, and Joshua S. Bloom. "The Two LIGO/Virgo Binary Black Hole Mergers on 2019 August 28 Were Not Strongly Lensed". In: *arXiv e-prints*, arXiv:1910.03601 (2019), arXiv:1910.03601. arXiv: 1910.03601 [astro-ph.CO].

[131] V. Bonvin et al. "H0LiCOW - V. New COSMOGRAIL time delays of HE 0435-1223: H_0 to 3.8 per cent precision from strong lensing in a flat ΛCDM model". In: MNRAS 465.4 (2017), pp. 4914–4930. DOI: 10.1093/mnras/stw3006. arXiv: 1607.01790 [astro-ph.CO].

[132] Keren Sharon et al. "Discovery of Multiply Imaged Galaxies behind the Cluster and Lensed Quasar SDSS J1004+4112". In: ApJ 629.2 (2005), pp. L73–L76. DOI: 10.1086/452633. arXiv: astro-ph/0507360 [astro-ph].

[133] Masamune Oguri et al. "The Hidden Fortress: structure and substructure of the complex strong lensing cluster SDSS J1029+2623". In: MNRAS 429.1 (2013), pp. 482–493. DOI: 10.1093/mnras/sts351. arXiv: 1209.0458 [astro-ph.CO].

[134] Keren Sharon et al. "Lens Model and Time Delay Predictions for the Sextuply Lensed Quasar SDSS J2222+2745". In: ApJ 835.1, 5 (2017), p. 5. DOI: 10.3847/1538-4357/835/1/5. arXiv: 1609.08848 [astro-ph.GA].

[135] G. P. Smith et al. "LIGO/Virgo S191216ap: Two candidate counterparts from UKIRT/WFCAM z-band observations". In: *GRB Coordinates Network* 26605 (Dec. 2019), p. 1.

[136] Philip J. Marshall et al. "SPACE WARPS - I. Crowdsourcing the discovery of gravitational lenses". In: MNRAS 455.2 (2016), pp. 1171–1190. DOI: 10.1093/mnras/stv2009. arXiv: 1504.06148 [astro-ph.IM].

[137] F. Lenzen, S. Schindler, and O. Scherzer. "Automatic detection of arcs and arclets formed by gravitational lensing". In: A&A 416 (2004), pp. 391–401. DOI: 10.1051/0004-6361:20034619. arXiv: astro-ph/0311554 [astro-ph].

[138] Kenneth C. Wong et al. "A New Approach to Identifying the Most Powerful Gravitational Lensing Telescopes". In: ApJ 769.1, 52 (May 2013), p. 52. DOI: 10.1088/0004-637X/769/1/52. arXiv: 1304.3127 [astro-ph.CO].

[139] Sebastian Stapelberg, Mauricio Carrasco, and Matteo Maturi. "EasyCritics - I. Efficient detection of strongly lensing galaxy groups and clusters in wide-field surveys". In: *Monthly Notices of the Royal Astronomical Society* 482.2 (2019), pp. 1824–1839. DOI: 10.1093/mnras/sty2784. arXiv: 1709.09758 [astro-ph.CO].

[140] Planck Collaboration et al. "Planck 2015 results. XIII. Cosmological parameters". In: A&A 594, A13 (2016), A13. DOI: 10.1051/0004-6361/201525830. arXiv: 1502.01589 [astro-ph.CO].

[141] P. Schechter. "An analytic expression for the luminosity function for galaxies." In: ApJ 203 (1976), pp. 297–306. DOI: 10.1086/154079.

[142] O. Ilbert et al. "Cosmos Photometric Redshifts with 30-Bands for 2-deg^2". In: ApJ 690.2 (2009), pp. 1236–1249. DOI: 10.1088/0004-637X/690/2/1236. arXiv: 0809.2101 [astro-ph].

[143] T. M. C. Abbott et al. "The Dark Energy Survey: Data Release 1". In: ApJS 239.2, 18 (2018), p. 18. DOI: 10.3847/1538-4365/aae9f0. arXiv: 1801.03181 [astro-ph.IM].

[144] Raphaël Gavazzi et al. "The Sloan Lens ACS Survey. IV. The Mass Density Profile of Early-Type Galaxies out to 100 Effective Radii". In: ApJ 667.1 (Sept. 2007), pp. 176–190. DOI: 10.1086/519237. arXiv: astro-ph/0701589 [astro-ph].

[145] Johan Richard et al. "LoCuSS: first results from strong-lensing analysis of 20 massive galaxy clusters at z = 0.2". In: MNRAS 404.1 (2010), pp. 325–349. DOI: 10.1111/j.1365-2966.2009.16274.x. arXiv: 0911.3302 [astro-ph.CO].

[146] Keiichi Umetsu et al. "CLASH: Joint Analysis of Strong-lensing, Weak-lensing Shear, and Magnification Data for 20 Galaxy Clusters". In: ApJ 821.2, 116 (Apr. 2016), p. 116. DOI: 10.3847/0004-637X/821/2/116. arXiv: 1507.04385 [astro-ph.CO].

[147] Julio F. Navarro, Carlos S. Frenk, and Simon D. M. White. "A Universal Density Profile from Hierarchical Clustering". In: ApJ 490.2 (Dec. 1997), pp. 493–508. DOI: 10.1086/304888. arXiv: astro-ph/9611107 [astro-ph].

[148] Nobuhiro Okabe and Graham P. Smith. "LoCuSS: weak-lensing mass calibration of galaxy clusters". In: MNRAS 461.4 (2016), pp. 3794–3821. DOI: 10.1093/mnras/stw1539. arXiv: 1507.04493 [astro-ph.CO].

[149] Roger Blandford and Ramesh Narayan. "Fermat's Principle, Caustics, and the Classification of Gravitational Lens Images". In: ApJ 310 (1986), p. 568. DOI: 10.1086/164709.

[150] Graham P. Smith et al. “A Hubble Space Telescope lensing survey of X-ray luminous galaxy clusters - IV. Mass, structure and thermodynamics of cluster cores at z= 0.2”. In: MNRAS 359.2 (May 2005), pp. 417–446. DOI: 10.1111/j.1365-2966.2005.08911.x. arXiv: astro-ph/0403588 [astro-ph].

[151] Maruša Bradač et al. “Dark Matter and Baryons in the X-Ray Luminous Merging Galaxy Cluster RX J1347.5-1145”. In: ApJ 681.1 (July 2008), pp. 187–196. DOI: 10.1086/588377. arXiv: 0711.4850 [astro-ph].

[152] M. Limousin et al. “Strong lensing by a node of the cosmic web. The core of MACS J0717.5+3745 at z = 0.55”. In: A&A 544, A71 (Aug. 2012), A71. DOI: 10.1051/0004-6361/201117921. arXiv: 1109.3301 [astro-ph.CO].

[153] Mathilde Jauzac et al. “The core of the massive cluster merger MACS J0417.5-1154 as seen by VLT/MUSE”. In: MNRAS 483.3 (Mar. 2019), pp. 3082–3097. DOI: 10.1093/mnras/sty3312. arXiv: 1811.02505 [astro-ph.GA].

[154] Masamune Oguri et al. “Can the Steep Mass Profile of A1689 Be Explained by a Triaxial Dark Halo?” In: ApJ 632.2 (Oct. 2005), pp. 841–846. DOI: 10.1086/452629. arXiv: astro-ph/0505452 [astro-ph].

[155] Virginia L. Corless, Lindsay J. King, and Douglas Clowe. “A new look at massive clusters: weak lensing constraints on the triaxial dark matter haloes of A1689, A1835 and A2204”. In: MNRAS 393.4 (Mar. 2009), pp. 1235–1254. DOI: 10.1111/j.1365-2966.2008.14294.x. arXiv: 0812.0632 [astro-ph].

[156] Mauro Sereno and Adi Zitrin. “Triaxial strong-lensing analysis of the z > 0.5 MACS clusters: the mass-concentration relation”. In: MNRAS 419.4 (Feb. 2012), pp. 3280–3291. DOI: 10.1111/j.1365-2966.2011.19968.x. arXiv: 1110.2854 [astro-ph.CO].

[157] Mauro Sereno et al. "Mass, shape and thermal properties of Abell 1689 using a multiwavelength X-ray, lensing and Sunyaev-Zel'dovich analysis". In: MNRAS 428.3 (Jan. 2013), pp. 2241–2254. DOI: 10.1093/mnras/sts186. arXiv: 1210.3359 [astro-ph.CO].

[158] Joachim Wambsganss, Paul Bode, and Jeremiah P. Ostriker. "Gravitational Lensing in a Concordance ΛCDM Universe: The Importance of Secondary Matter along the Line of Sight". In: ApJ 635.1 (Dec. 2005), pp. L1–L4. DOI: 10.1086/498976. arXiv: astro-ph/0405147 [astro-ph].

[159] Matthew B. Bayliss et al. "Line-of-sight Structure toward Strong Lensing Galaxy Clusters". In: ApJ 783.1, 41 (Mar. 2014), p. 41. DOI: 10.1088/0004-637X/783/1/41. arXiv: 1312.3637 [astro-ph.CO].

[160] Anson D'Aloisio, Priyamvada Natarajan, and Paul R. Shapiro. "The effect of large-scale structure on the magnification of high-redshift sources by cluster lenses". In: MNRAS 445.4 (Dec. 2014), pp. 3581–3591. DOI: 10.1093/mnras/stu1931. arXiv: 1311.1614 [astro-ph.CO].

[161] Henry C. Ferguson et al. "The Size Evolution of High-Redshift Galaxies". In: ApJ 600.2 (2004), pp. L107–L110. DOI: 10.1086/378578. arXiv: astro-ph/0309058 [astro-ph].

[162] Patrick L. Kelly et al. "Extreme magnification of an individual star at redshift 1.5 by a galaxy-cluster lens". In: *Nature Astronomy* 2 (2018), pp. 334–342. DOI: 10.1038/s41550-018-0430-3. arXiv: 1706.10279 [astro-ph.GA].

[163] S. A. Rodney et al. "Two peculiar fast transients in a strongly lensed host galaxy". In: *Nature Astronomy* 2 (2018), pp. 324–333. DOI: 10.1038/s41550-018-0405-4. arXiv: 1707.02434 [astro-ph.GA].

[164] Stefan Hilbert et al. “Strong-lensing optical depths in a ΛCDM universe - II. The influence of the stellar mass in galaxies”. In: MNRAS 386.4 (2008), pp. 1845–1854. DOI: 10.1111/j.1365-2966.2008.13190.x. arXiv: 0712.1593 [astro-ph].

[165] Dan Ryczanowski et al. “Enabling discovery of gravitationally lensed explosive transients: a new method to build an all-sky watch-list of groups and clusters of galaxies”. In: *arXiv e-prints*, arXiv:2204.12984 (Apr. 2022), arXiv:2204.12984. arXiv: 2204.12984 [astro-ph.CO].

[166] Radosław Wojtak, Jens Hjorth, and Christa Gall. “Magnified or multiply imaged? - Search strategies for gravitationally lensed supernovae in wide-field surveys”. In: MNRAS 487.3 (Aug. 2019), pp. 3342–3355. DOI: 10.1093/mnras/stz1516. arXiv: 1903.07687 [astro-ph.CO].

[167] F. Pacaud et al. “The XXL Survey. II. The bright cluster sample: catalogue and luminosity function”. In: A&A 592, A2 (June 2016), A2. DOI: 10.1051/0004-6361/201526891. arXiv: 1512.04264 [astro-ph.CO].

[168] R. A. Sunyaev and Ya. B. Zeldovich. “The Observations of Relic Radiation as a Test of the Nature of X-Ray Radiation from the Clusters of Galaxies”. In: *Comments on Astrophysics and Space Physics* 4 (Nov. 1972), p. 173.

[169] Planck Collaboration et al. “Planck 2015 results. XXVII. The second Planck catalogue of Sunyaev-Zeldovich sources”. In: A&A 594, A27 (Sept. 2016), A27. DOI: 10.1051/0004-6361/201525823. arXiv: 1502.01598 [astro-ph.CO].

[170] E. S. Rykoff et al. “redMaPPer. I. Algorithm and SDSS DR8 Catalog”. In: ApJ 785.2, 104 (Apr. 2014), p. 104. DOI: 10.1088/0004-637X/785/2/104. arXiv: 1303.3562 [astro-ph.CO].

[171] Peter R. M. Eisenhardt et al. “Clusters of Galaxies in the First Half of the Universe from the IRAC Shallow Survey”. In: ApJ 684.2 (Sept. 2008), pp. 905–932. DOI: 10.1086/590105. arXiv: 0804.4798 [astro-ph].

[172] Euclid Collaboration et al. “Euclid preparation. III. Galaxy cluster detection in the wide photometric survey, performance and algorithm selection”. In: A&A 627, A23 (July 2019), A23. DOI: 10.1051/0004-6361/201935088. arXiv: 1906.04707 [astro-ph.CO].

[173] Anthony H. Gonzalez et al. “The Massive and Distant Clusters of WISE Survey. I. Survey Overview and a Catalog of ¿2000 Galaxy Clusters at z 1”. In: ApJS 240.2, 33 (Feb. 2019), p. 33. DOI: 10.3847/1538-4365/aafad2. arXiv: 1809.06820 [astro-ph.CO].

[174] S. Dye et al. “The UKIRT Hemisphere Survey: definition and J-band data release”. In: MNRAS 473.4 (Feb. 2018), pp. 5113–5125. DOI: 10.1093/mnras/stx2622. arXiv: 1707.09975 [astro-ph.IM].

[175] R. G. McMahon et al. “First Scientific Results from the VISTA Hemisphere Survey (VHS)”. In: *The Messenger* 154 (Dec. 2013), pp. 35–37.

[176] Edward L. Wright et al. “The Wide-field Infrared Survey Explorer (WISE): Mission Description and Initial On-orbit Performance”. In: AJ 140.6 (Dec. 2010), pp. 1868–1881. DOI: 10.1088/0004-6256/140/6/1868. arXiv: 1008.0031 [astro-ph.IM].

[177] A. Edge et al. “The VISTA Kilo-degree Infrared Galaxy (VIKING) Survey: Bridging the Gap between Low and High Redshift”. In: *The Messenger* 154 (Dec. 2013), pp. 32–34.

[178] Federico Marocco et al. “The CatWISE2020 Catalog”. In: ApJS 253.1, 8 (Mar. 2021), p. 8. DOI: 10.3847/1538-4365/abd805. arXiv: 2012.13084 [astro-ph.IM].

[179] Conor L. Mancone and Anthony H. Gonzalez. "EzGal: A Flexible Interface for Stellar Population Synthesis Models". In: PASP 124.916 (June 2012), p. 606. DOI: 10.1086/666502. arXiv: 1205.0009 [astro-ph.IM].

[180] G. Bruzual and S. Charlot. "Stellar population synthesis at the resolution of 2003". In: MNRAS 344.4 (Oct. 2003), pp. 1000–1028. DOI: 10.1046/j.1365-8711.2003.06897.x. arXiv: astro-ph/0309134 [astro-ph].

[181] Gilles Chabrier. "Galactic Stellar and Substellar Initial Mass Function". In: PASP 115.809 (July 2003), pp. 763–795. DOI: 10.1086/376392. arXiv: astro-ph/0304382 [astro-ph].

[182] Yen-Ting Lin, Joseph J. Mohr, and S. Adam Stanford. "K-Band Properties of Galaxy Clusters and Groups: Luminosity Function, Radial Distribution, and Halo Occupation Number". In: ApJ 610.2 (Aug. 2004), pp. 745–761. DOI: 10.1086/421714. arXiv: astro-ph/0402308 [astro-ph].

[183] Y. Wang, R. J. Brunner, and J. C. Dolence. "The SDSS galaxy angular two-point correlation function". In: MNRAS 432.3 (July 2013), pp. 1961–1979. DOI: 10.1093/mnras/stt450. arXiv: 1303.2432 [astro-ph.CO].

[184] M. Carrasco et al. "EasyCritics II. Testing its efficiency: new gravitational lens candidates in CFHTLenS". In: *arXiv e-prints*, arXiv:1807.03793 (July 2018), arXiv:1807.03793. arXiv: 1807.03793 [astro-ph.CO].

[185] Graham P. Smith et al. "Strong-lensing of Gravitational Waves by Galaxy Clusters". In: *IAU Symposium* 338 (Oct. 2018), pp. 98–102. DOI: 10.1017/S1743921318003757. arXiv: 1803.07851 [astro-ph.CO].

[186] D. Ryczanowski et al. "Observations of lensed supernova candidate AT 2021vkz (ZTF21abqoivk) with the Liverpool Telescope". In: *Transient Name Server AstroNote* 231 (Sept. 2021), pp. 1–231.

[187] Matteo Bianconi et al. "On the gravitational lensing interpretation of three gravitational wave detections in the mass gap by LIGO and Virgo". In: *arXiv e-prints*, arXiv:2204.12978 (Apr. 2022), arXiv:2204.12978. arXiv: 2204.12978 [astro-ph.GA].

[188] LSST Dark Energy Science Collaboration (LSST DESC) et al. "The LSST DESC DC2 Simulated Sky Survey". In: ApJS 253.1, 31 (Mar. 2021), p. 31. DOI: 10.3847/1538-4365/abd62c. arXiv: 2010.05926 [astro-ph.IM].

[189] A. Finoguenov et al. "CODEX clusters. Survey, catalog, and cosmology of the X-ray luminosity function". In: A&A 638, A114 (June 2020), A114. DOI: 10.1051/0004-6361/201937283. arXiv: 1912.03262 [astro-ph.CO].

[190] John E. Carlstrom, Gilbert P. Holder, and Erik D. Reese. "Cosmology with the Sunyaev-Zel'dovich Effect". In: ARA&A 40 (Jan. 2002), pp. 643–680. DOI: 10.1146/annurev.astro.40.060401.093803. arXiv: astro-ph/0208192 [astro-ph].

[191] Donald G. York et al. "The Sloan Digital Sky Survey: Technical Summary". In: AJ 120.3 (Sept. 2000), pp. 1579–1587. DOI: 10.1086/301513. arXiv: astro-ph/0006396 [astro-ph].

[192] Michael D. Gladders and H. K. C. Yee. "A New Method For Galaxy Cluster Detection. I. The Algorithm". In: AJ 120.4 (Oct. 2000), pp. 2148–2162. DOI: 10.1086/301557. arXiv: astro-ph/0004092 [astro-ph].

[193] W. Voges et al. "The ROSAT all-sky survey bright source catalogue". In: A&A 349 (Sept. 1999), pp. 389–405. arXiv: astro-ph/9909315 [astro-ph].

[194] K. W. Smith et al. "Lasair: The Transient Alert Broker for LSST:UK". In: *Research Notes of the American Astronomical Society* 3.1, 26 (Jan. 2019), p. 26. DOI: 10.3847/2515-5172/ab020f.

[195] K. W. Smith et al. "Design and Operation of the ATLAS Transient Science Server". In: PASP 132.1014, 085002 (Aug. 2020), p. 085002. DOI: 10.1088/1538-3873/ab936e. arXiv: 2003.09052 [astro-ph.IM].

[196] J. L. Tonry et al. "ATLAS: A High-cadence All-sky Survey System". In: PASP 130.988 (June 2018), p. 064505. DOI: 10.1088/1538-3873/aabadf. arXiv: 1802.00879 [astro-ph.IM].

[197] Adam G. Riess et al. "Identification of Type Ia Supernovae at Redshift 1.3 and Beyond with the Advanced Camera for Surveys on the Hubble Space Telescope". In: ApJ 600.2 (Jan. 2004), pp. L163–L166. DOI: 10.1086/378311. arXiv: astro-ph/0308185 [astro-ph].

[198] K. W. Davis et al. "UCSC Transient Classification Report for 2021-09-04". In: *Transient Name Server Classification Report* 2021-3046 (Sept. 2021), pp. 1–3046.

[199] Feryal Özel et al. "The Black Hole Mass Distribution in the Galaxy". In: ApJ 725.2 (Dec. 2010), pp. 1918–1927. DOI: 10.1088/0004-637X/725/2/1918. arXiv: 1006.2834 [astro-ph.GA].

[200] Will M. Farr et al. "The Mass Distribution of Stellar-mass Black Holes". In: ApJ 741.2, 103 (Nov. 2011), p. 103. DOI: 10.1088/0004-637X/741/2/103. arXiv: 1011.1459 [astro-ph.GA].

[201] Anuradha Gupta et al. "Black holes in the low-mass gap: Implications for gravitational-wave observations". In: Phys. Rev. D 101.10, 103036 (May 2020), p. 103036. DOI: 10.1103/PhysRevD.101.103036. arXiv: 1909.05804 [gr-qc].

[202] Leo P. Singer and Larry R. Price. "Rapid Bayesian position reconstruction for gravitational-wave transients". In: Phys. Rev. D 93.2, 024013 (Jan. 2016), p. 024013. DOI: 10.1103/PhysRevD.93.024013. arXiv: 1508.03634 [gr-qc].

[203] S. D. Barthelmy et al. "GRB Coordinates Network (GCN): A status report". In: *Gamma-ray Bursts, 5th Huntsville Symposium*. Ed. by R. Marc Kippen, Robert S. Mallozzi, and Gerald J. Fishman. Vol. 526. American Institute of Physics Conference Series. Sept. 2000, pp. 731–735. DOI: 10.1063/1.1361631.

[204] J. Veitch et al. "Parameter estimation for compact binaries with ground-based gravitational-wave observations using the LALInference software library". In: Phys. Rev. D 91.4, 042003 (Feb. 2015), p. 042003. DOI: 10.1103/PhysRevD.91.042003. arXiv: 1409.7215 [gr-qc].

[205] Gregory Ashton et al. "BILBY: A User-friendly Bayesian Inference Library for Gravitational-wave Astronomy". In: ApJS 241.2, 27 (Apr. 2019), p. 27. DOI: 10.3847/1538-4365/ab06fc. arXiv: 1811.02042 [astro-ph.IM].

[206] Matt Nicholl et al. "Tight multimessenger constraints on the neutron star equation of state from GW170817 and a forward model for kilonova light-curve synthesis". In: MNRAS 505.2 (Aug. 2021), pp. 3016–3032. DOI: 10.1093/mnras/stab1523. arXiv: 2102.02229 [astro-ph.HE].

[207] David N. Burrows et al. "The Swift X-Ray Telescope". In: *X-Ray and Gamma-Ray Instrumentation for Astronomy XIII*. Ed. by Kathryn A. Flanagan and Oswald H. W. Siegmund. Vol. 5165. Society of Photo-Optical Instrumentation Engineers (SPIE) Conference Series. Feb. 2004, pp. 201–216. DOI: 10.1117/12.504868.

[208] N. Gehrels et al. "The Swift Gamma-Ray Burst Mission". In: ApJ 611.2 (Aug. 2004), pp. 1005–1020. DOI: 10.1086/422091. arXiv: astro-ph/0405233 [astro-ph].

[209] P. A. Evans et al. "An online repository of Swift/XRT light curves of γ-ray bursts". In: A&A 469.1 (July 2007), pp. 379–385. DOI: 10.1051/0004-6361:20077530. arXiv: 0704.0128 [astro-ph].

[210] P. A. Evans et al. "Methods and results of an automatic analysis of a complete sample of Swift-XRT observations of GRBs". In: MNRAS 397.3 (Aug. 2009), pp. 1177–1201. DOI: 10.1111/j.1365-2966.2009.14913.x. arXiv: 0812.3662 [astro-ph].

[211] Charles Meegan et al. "The Fermi Gamma-ray Burst Monitor". In: ApJ 702.1 (Sept. 2009), pp. 791–804. DOI: 10.1088/0004-637X/702/1/791. arXiv: 0908.0450 [astro-ph.IM].

[212] Sarah L. Mulroy et al. "LoCuSS: scaling relations between galaxy cluster mass, gas, and stellar content". In: MNRAS 484.1 (Mar. 2019), pp. 60–80. DOI: 10.1093/mnras/sty3484. arXiv: 1901.11276 [astro-ph.CO].

[213] Aaron D. Ludlow et al. "The mass-concentration-redshift relation of cold dark matter haloes". In: MNRAS 441.1 (June 2014), pp. 378–388. DOI: 10.1093/mnras/stu483. arXiv: 1312.0945 [astro-ph.CO].